

POLITECNICO DI TORINO

Collegio di Ingegneria Chimica e dei Materiali

**Master of Science Course
in Materials Engineering**

Master of Science Thesis

“Optimization of process parameters for Directed Energy Deposition of IN718 nickel- based superalloy.”



Thesis Supervisor

Prof. Sara Biamino

Thesis Advisors

Dr. Abdollah Saboori

Dr. Giulio Marchese

Candidate

Stefano Di Falco

October 2019

Contents

- 1. Introduction.....1
- 2. Metal Additive Manufacturing.....3
 - 2.1 Introduction.....3
 - 2.2 Brief AM “Pre-History” and “History”4
 - 2.3 Additive Manufacturing Technologies and Standards.....10
 - 2.4 Additive Manufacturing Advantages and Disadvantages.....10
 - 2.5 The Additive Manufacturing “Approach”12
 - 2.6 Metal AM Categories.....14
 - 2.6.1 Powder Bed Fusion (PBF).....15
 - 2.6.1.1 Selective Laser Melting (SLM).....16
 - 2.6.1.2 Electron Beam Melting (EBM).....17
 - 2.6.2 Direct Energy Deposition (DED).....19
 - 2.6.2.1 DED Wire feeding.....20
 - 2.6.2.2 DED Powder feeding.....22
 - 2.6.2.2.1 Process parameters in LBMD.....23
 - 2.6.2.2.2 Parameters correlation.....26
 - 2.6.3 DED and PBF comparison.....29
 - 2.7 Metal AM Applications.....30
 - 2.7.1 DED Aerospace/Aviation applications.....31
 - 2.7.2 Design philosophies and repairing.....33
 - 2.7.3 Hybrid Additive-Subtractive Manufacturing systems for repairing operations.....35
 - 2.8 Ni Superalloys and AM.....38
 - 2.8.1 Microstructure description and Phases.....39
 - 2.8.2 Strengthening by Solid Solution.....41
 - 2.8.3 Hardening by Precipitation.....41
 - 2.8.4 Alloying elements.....43
- 3. IN718 and DED.....45
 - 3.1 Melt Pool.....45
 - 3.1.1 Chemical-Physical aspects.....45
 - 3.1.2 Dynamic Melt Pool and grains morphology.....46
 - 3.1.3 Melt-pool cross-section morphology.....47
 - 3.2 Single Wall.....48

3.2.1 Grains morphology.....	48
3.2.2 Microstructure and phases.....	50
3.3 SEM / EBSD Analysis in “as-deposited conditions.”.....	52
3.3.1 SEM / EBSD: Morphology & Texture in “as-deposited conditions”.....	52
3.3.2 SEM / EBSD: Phases and chemical composition in “as-deposited”.....	56
4. Materials and Methods.....	61
4.1 Feedstock particles.....	61
4.2 DED Machine.....	62
4.3 Stereomicroscope.....	63
4.4 Cutting.....	64
4.4.1 Sampling.....	65
4.5 Mounting.....	67
4.6 Polishing.....	68
4.7 Chemical etching.....	69
4.8 Optical Microscope.....	70
4.9 SEM.....	70
5. Results and Discussion.....	71
5.1 Purposes.....	71
5.1.1 Features specifications and themes of analysis.....	71
5.2 Single Scan Tracks characterization.....	72
5.2.1 Single Scan Tracks morphology.....	73
5.2.2 SSTs and Heat Affected Zone (HAZ) regularity.....	76
5.2.3 SSTs etched Melt Pools HAZ.....	80
5.2.4 SSTs etched Melt Pools Morphology.....	80
5.2.5 SSTs etched Melt Pools coherence with the substrate.....	81
5.2.5.1 Melt Pool’s Width, Fusion depth and Bead height.....	82
5.2.6 SST n° 37 - etched Melt Pool’s SEM/EDS analysis.....	88
5.3 Layers characterization.....	90
5.3.1 Substrate 2 – Inclusions.....	90
5.3.1.1 Inclusions Percentage area.....	93
5.3.1.2 Inclusions Average size.....	94
5.3.1.4 Inclusions discussion.....	95
5.3.2 Substrates 1 and 2 – etched layers morphology.....	98
5.4 Bulks/Cubes Characterization.....	102

5.4.1 Defects analysis of the Cubes.....	102
5.4.2 Optical analysis of the etched Cubes.....	104
5.4.2.1 Top of the Cubes.....	106
5.4.2.2 Core of the Cubes.....	108
5.4.2.3 Bottom of the Cubes.....	110
5.5 SEM/EDS Cubes' analysis.....	112
5.5.1 Laves phases EDS analysis.....	116
5.5.2 δ -phases – EDS analysis.....	117
5.5.3 Carbides – EDS analysis.....	117
5.5.4 Oxide layer – EDS analysis.....	120
5.6 SEM/EDS Substrate.....	122
5.6.1 Carbides.....	122
5.6.2 Laves-phases.....	123
5.6.3 δ -phases.....	124
6.Conclusions.....	127
6.1 SSTs.....	127
6.2 Layers.....	128
6.3 Bulks.....	128
7.References.....	130
8.Thanks.....	134

Sommario italiano

1. Introduzione

Definita da "McKensey & Company" come uno dei co-protagonisti della "Ops 4.0 Revolution", l' "Additive Manufacturing" (AM), allo stesso modo della scienza dei Big Data, dell'analisi avanzata, della robotica e dell'intelligenza artificiale, si propone di essere uno dei settori leader che, nel prossimo futuro, aumenteranno la produttività industriale del 20% (McKinsey & Company, 2018). Grazie alle sue caratteristiche di flessibilità, versatilità e ai suoi numerosi vantaggi, questa recente tecnologia, ha già infatti trovato terreno fertile nei campi più tecnologicamente avanzati, come quello dell'Aviazione e dell'Automotive, in cui il suo impatto è stato definito da tecnici ed esperti come "Disruptive"! In particolar modo, l'AM ha attirato un notevole interesse da parte delle divisioni di ricerca e sviluppo di società leader di molteplici settori industriali dell'Hi-tech, come l'Aviazione, l'Aerospazio, l'Automotive e il Biomedicale, grazie alle sue capacità di: produrre componenti dotati di alte performances, ridurre il time to market, ridurre il peso delle parti, semplificare la supply chain, fornire alta versatilità di progetto, garantire una produzione On-demand di componenti personalizzati e decentralizzare la produzione. In particolar modo, fra tutte le famiglie di AM presenti ad oggi sul mercato, la Metal AM è spesso considerata di primo rilievo quando a richiedersi sono componenti con performances e proprietà meccaniche superiori, altresì dotati di ottime proprietà di conducibilità termica ed elettrica. Più nello specifico la Metal AM può essere distinta in due categorie principali: la Powder Bed Fusion (PBF) e la Directed Energy Deposition (DED). La prima sfrutta una sorgente laser focalizzata su un letto di polvere al fine di fondere selettivamente le particelle di feedstock subito prima compattate in un sottile strato (layer) da un rullo/recoater sulla piattaforma di costruzione. Con la progressiva ritrazione verso il basso di quest'ultima, il processo viene iterato strato per strato realizzando così una parte 3D. Diversamente, la tecnologia a deposizione diretta impiega un equipaggiamento composto da un braccio robotico principale che movimentata spazialmente una testa di deposizione comprensiva nel suo corpo di un sistema di alimentazione e una sorgente laser passante con asse coincidente a quello della testa. Nel caso specifico di un'alimentazione a polvere, il materiale particolato fluisce all'interno degli appositi canali di approvvigionamento sospinto da un gas vettore, che ne convoglia il particolato in direzione del raggio laser. Spesso inoltre la zona di fusione è schermata da un gas protettivo (N₂ o Ar). Dunque, il processo di deposizione avviene per fusione locale del substrato (su cui la sorgente energetica è focalizzata) per formazione di una piscina di fusione "Melt Pool", dentro la quale vengono intrappolate le particelle del materiale d'apporto. Tale processo avviene inoltre in modo dinamico, in conseguenza dello spostamento della testa di deposizione a date velocità trasversale e direzione. La solidificazione del sistema fisico così composto, corrisponde allora a uno spessore di materiale adeso al substrato di partenza quasi a significare un cordone di saldatura. Iterando il processo di deposizione è quindi possibile fabbricare o riparare componenti in tre dimensioni.

Sebbene entrambe le tecnologie perseguano la stessa finalità di ottenimento di parti funzionali e performanti, fra le due, si evidenziano sostanziali differenze in termini di volumi producibili, rate di produzione, precisione dimensionale e tolleranze perseguibili, proprietà meccaniche e finitura superficiale ottenibili. In particolar modo, la tecnologia PBF consente l'ottenimento di parti funzionali, nel rispetto di ottime tolleranze geometriche e dimensionali ($\pm 0,05-0,1$ mm), ridotta rugosità superficiale (4-11 μ m), e con microstrutture generalmente molto fini che si traducono in proprietà meccaniche elevate. Differentemente, rispetto alla tecnologia PBF, la deposizione diretta DED fornisce accuratezza geometrica delle parti inferiore (di ± 25 mm) e

una rugosità superficiale maggiore (di circa 25 μm). Inoltre, la microstruttura derivante dal processo a deposizione diretta, se paragonata a quella ottenibile via LPBF, risulta essere più grossolana e marcatamente anisotropa. Tuttavia, i maggiori vantaggi forniti dalla tecnologia DED sono da riconoscersi nella capacità di produrre componenti massivi aventi volumi non egualmente ottenibili con altre tecnologie AM, poiché limitate dagli ingombri delle camere di stampa. Non di meno, l'alto grado di mobilità spaziale del braccio robotico, insieme alla possibilità di movimentare il piatto di stampa nelle tre dimensioni, fornisce fino a 9 gradi di libertà che consentono quindi un'enorme flessibilità produttiva. In ragione di tale confronto, appare dunque evidente che la scelta di una famiglia rispetto all'altra sia dettata, più che da valori di merito, dalle esigenze dei differenti casi applicativi.

Tuttavia, uno dei limiti più costrittivi che accomuna ambedue, sono i costi di produzione quando volumi medio-grandi di componenti sono richiesti. Infatti, il vantaggio economico nel produrre componenti via AM, surrogando i processi produttivi convenzionali, è tutt'oggi fortemente limitato a settori industriali di nicchia e alla produzione di tirature limitate dove si richiede un'elevata complessità delle parti. Piuttosto, in molti casi si ricerca la coesistenza della produzione additiva con i processi di manufacturing tradizionali al fine di sfruttare i vantaggi di complementarità di entrambe le tecnologie.

Un esempio di coerenza fra processi produttivi convenzionali e Metal AM, è rappresentato dalla possibilità di utilizzare sistemi ibridi DED-CNC (Figura 1), per riparare stampi o componenti funzionali danneggiati e precedentemente costruiti tramite processi convenzionali. Con tali apparati, è infatti possibile depositare nuovo materiale in corrispondenza delle aree difettate, rifinando poi forma tolleranze e superfici tramite operazioni sottrattive, riducendo così a obsoleta la necessità di fabbricare ex novo altri componenti. In modo particolare, quest'ultimo caso applicativo è preso in analisi nel presente incarico di tesi.

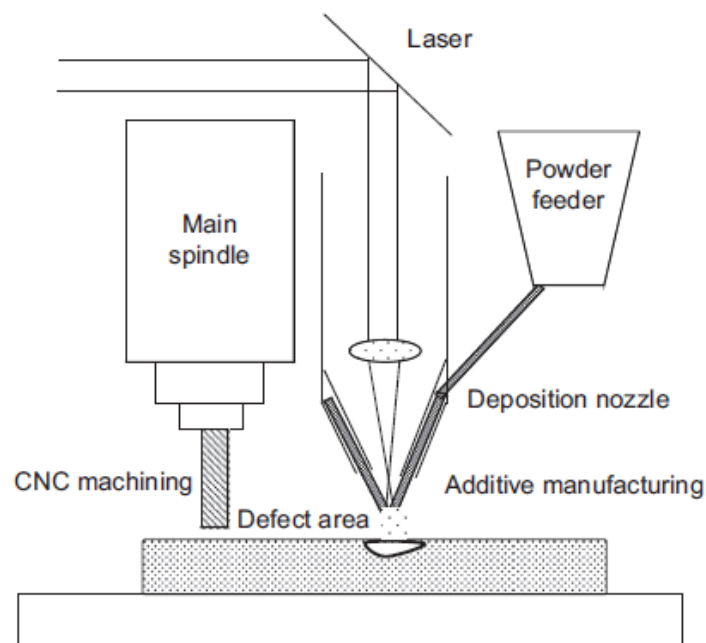


Figura 1: Apparato ibrido DED-CNC di fabbricazione additiva e sottrattiva (Villeneuve et al., 2018)

Inoltre, la possibilità di questi apparati di riparare i componenti danneggiati non richiedendo complesse attrezzature e in modo versatile, per esecuzione di processo e impiego di materiali, risponde perfettamente alle esigenze manifestate dall'Aviazione. Infatti, la gran parte dei

componenti avionici è progettata secondo una filosofia di design “Damage tolerance” che prevede di tracciare lo stato di vita del componente, in relazione allo stato di avanzamento delle cricche o dei danneggiamenti all’interno di esso, stabilendo aprioristicamente un punto di ispezione e ripristino dello stesso (Figura 2). Proprio in questa istanza un apparato ibrido DED-CNC risulterebbe adatto a compiere operazioni di riparazione estendendo la vita del componente.

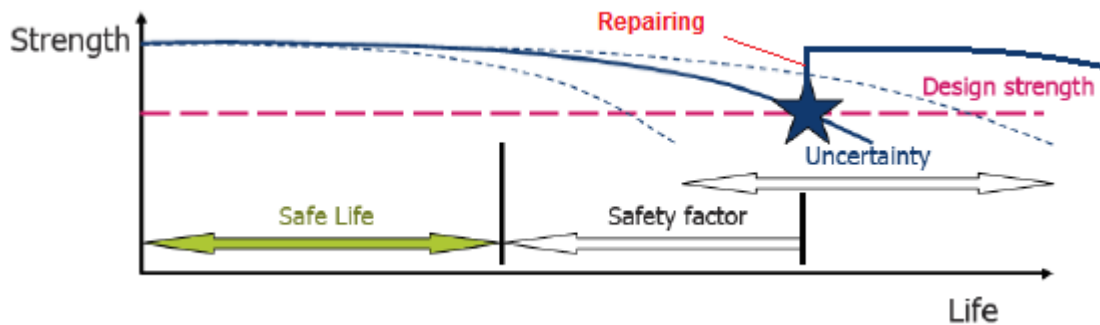


Figura 2: Diagramma resistenza-tempo di vita di un componente avionico progettato “Damage tolerant” e riparato (Alderliesten, 2018).

Riconducendosi almeno in prima approssimazione allo scenario appena esposto, nel presente incarico di tesi si riportano i risultati di una campagna sperimentale volta a identificare i parametri di processo ottimali con cui settare un apparato DED alimentato a polveri di IN718. Ipotizzando che tale apparato possa essere integrato in uno ibrido DED-Laser ablation-milling, tali parametri di processo potrebbero essere dunque impiegati per compiere deposizioni additive e riparative di componenti avionici danneggiati in IN718.

A tale fine, tre differenti tipologie di “caratteristiche” in IN718 costruite a differenti valori di potenza laser P e velocità di deposizione F su un substrato di IN718 non preriscaldato, sono state analizzate sotto molteplici aspetti.

Più nel dettaglio le caratteristiche prese in analisi sono:

- 40 Singole tracce uniche fra loro (Single Scan Tracks-SSTs)
- 20 Singoli Layers unici fra loro (SLs) suddivisi nei due differenti substrati 1 e 2
- 3 Cubi depositati impiegando i medesimi parametri di processo (Cubes)

1.1 Ulteriori specifiche e temi di analisi:

- Le SSTs sono state realizzate impiegando:

- 8 livelli di Feed rate, F [mm/min]: 300, 450, 600, 750, 900, 1050, 1200, 1350
- 5 livelli di Laser Power, P [W]: 300, 400, 500, 600, 700.

e caratterizzate nella loro:

- morfologia
- regolarità della loro zona termicamente alterata (ZTA)
- morfologia e regolarità dei “Melt Pools” osservati lungo le cross-sections delle SSTs dopo attacco chimico.
- coerenza con il substrato

- I **SLs** del “Substarto 1” sono stati realizzati impiegando:

- un’unica Potenza laser, P [W]: 600
- 2 velocità di deposizione, F [mm/min]: 750, 900
- 2 Hatching distances, Hd [mm]: 0,3, 0,4

mentre quelli del “Substrato 2” utilizzando:

- un’unica Potenza laser, P [W]: 400
- 2 velocità di deposizione, F [mm/min]: 750, 900
- 2 Hatching distances, Hd [mm]: 0,3, 0,4.

Inoltre, I **SLs** di ogni substrato sono stati caratterizzati in:

- area percentuale di defettologie
- morfologia delle deposizioni dopo attacco chimico

- I **Cubi** sono stati realizzati impiegando:

- un’unica Potenza laser, P [W]: 750
- un’unica velocità di deposizione, F [mm/min]: 900
- un’unica Hatching distance H [mm]: 0,3
- layer thickness dz [mm]: 0,2
- la strategia di hatching “Raster”: 0° /90° /45° /135° /60° /120°

e caratterizzati in:

- area percentuale di defettologie
- morfologia della microstruttura
- area percentuale delle fasi laviche
- tipologia delle fasi presenti
- dimensioni e composizione dello strato di ossido sopra formatosi.

2. Materiali e Metodi

2.1 Polveri

Il feed-stock che è stato utilizzato per alimentare l’apparato DED è costituito da polveri sferiche di IN718, ottenute tramite processo di atomizzazione a gas, aventi taglia media grossolana compresa fra 44 e 106 μm . L’analisi morfologica superficiale condotta tramite microscopia ottica a scansione, ha inoltre permesso di rivelare la non uniformità di forma delle particelle evidenziando la presenza di particelle satellitari adese alla superficie di quelle principali. L’analisi EDS di composizione di superficie, ha invece rivelato la presenza di Ni, Cr, Fe, O e Nb oltre a una modesta percentuale di Ti e Al (Figura 3), elementi potenziali formatori di composti e ossidi non desiderati.

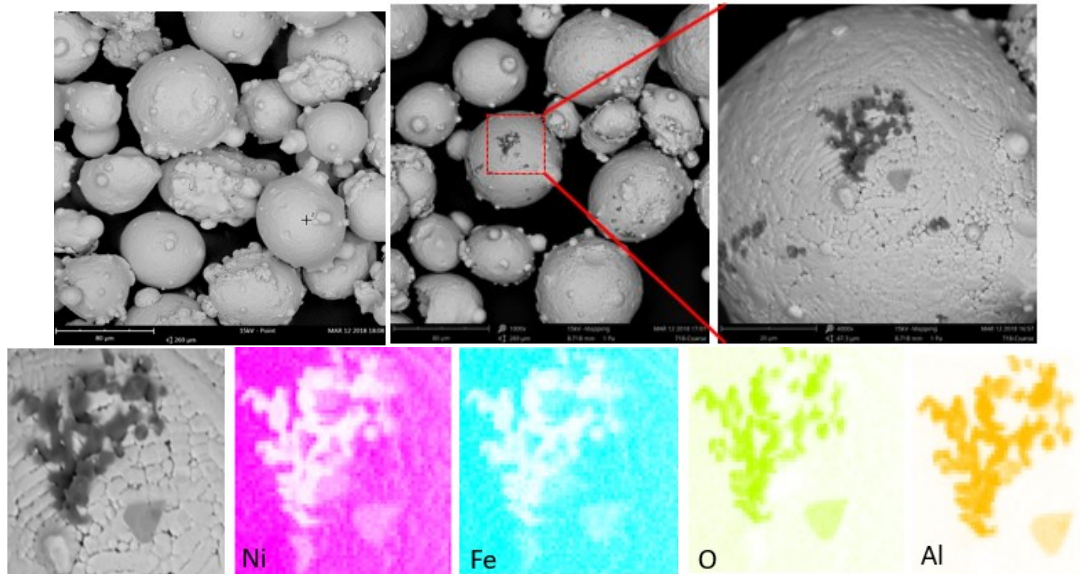


Figura 3: Analisi EDS composizionale della superficie delle polveri

Volendo approfondire l'aspetto composizionale, l'analisi EDS è stata applicata anche alle cross-sections delle particelle evidenziando la presenza non trascurabile di porosità interne e di ossidi di alluminio (Figura 4). La genesi di queste defettologie è stata imputata alla scelta di eseguire il processo di atomizzazione in un'atmosfera non inerte.

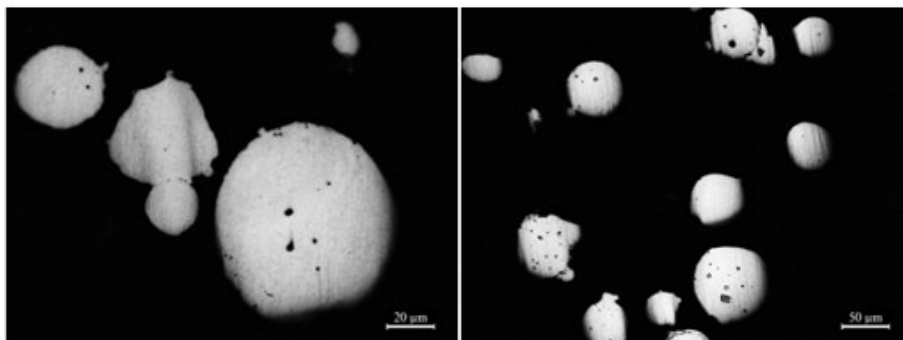


Figura 4: Analisi SEM delle cross-sections delle polveri di feedstock.

2.2 Stereomicroscopio

Le caratteristiche in oggetto di analisi in questa campagna sono state dapprima analizzate nella loro morfologia superficiale tramite un'analisi ottica allo stereomicroscopio LEICA EZ4W. Tale metodologia di ispezione ha permesso dunque di determinare le regolarità o irregolarità di forma delle caratteristiche e quindi valutare macroscopicamente la conformità di deposizione delle stesse.

2.3 Taglio dei campioni e inglobamento

I substrati contenenti le caratteristiche da essere analizzate sono stati tagliati tramite la Cutting Machine "Remet TR 100s", equipaggiata con una lama CERMET al carburo di silicio, campionando dunque le stesse nei volumi minimi di materiale che le potessero contenere.

Ulteriormente, ogni campione, è stato sezionato lungo il piano di sezione trasversale delle caratteristiche. I campionamenti così ottenuti, sono stati successivamente inglobati in una matrice polimerica termoidurente a costituire una montatura adatta alla corretta e agile manipolazione del campione nelle successive operazioni di lucidatura.

2.4 Lucidatura e attacco chimico

La lucidatura delle caratteristiche, operazione indispensabile da eseguirsi per permettere l'osservazione microscopica, è stata eseguita tramite una polishing machine "Presi Mecatech 234" utilizzando un set di carte abrasive rispettivamente indicizzate: #FEPA 320, 600, 800, 1200, 2400 e 4000. Infine, è stata eseguita una lucidatura più spinta atta a portare la rugosità media superficiale prima a 3 e poi 1 μm tramite l'ausilio di due panni in feltro cosparsi di una soluzione di lubrificante e pasta diamantata. A titolo di esempio, si riportano le immagini delle superfici così lucidate delle SSTs, ossevate a microscopio ottico in Figura 5.

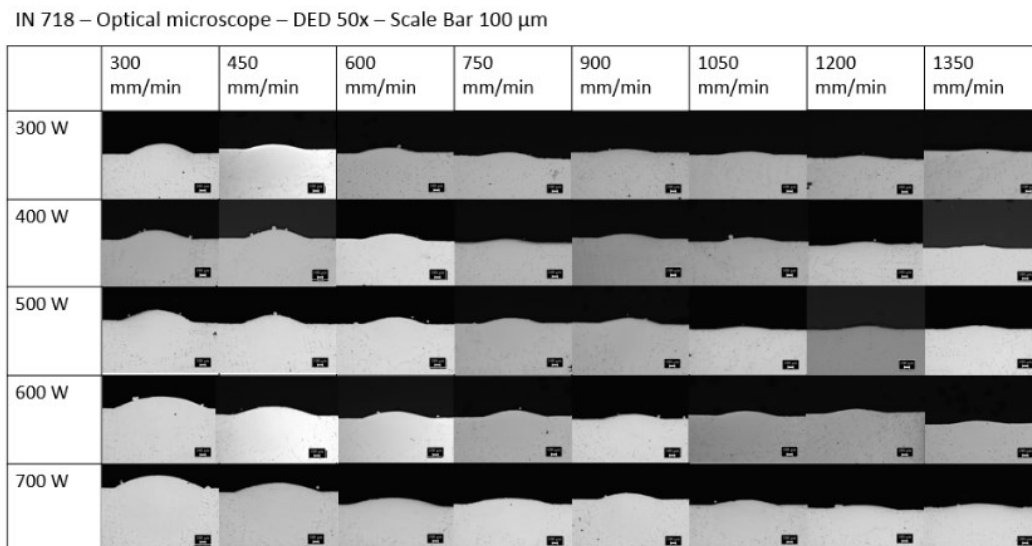


Figura 5: Sezioni trasversali delle SSTs dopo lucidatura osservate a 50X per microscopia ottica.

Dopo la loro lucidatura, i campioni sono stati attaccati chimicamente con la soluzione Kalling's n° 2 di composizione:

- CuCl_2 10 gr
- Hydrochloridic acid 200 ml
- Ethanol absolute 200 ml

I provini sono stati pertanto immersi nella soluzione per un tempo medio di 15s prima di essere spenti in acqua distillata. Tale trattamento di incisione chimica metallografica, ha permesso ai processi corrosivi di prendere luogo con rates di corrosione differenti a seconda che interessassero fasi e microstrutture diverse. La superficie così preparata e la sua microstruttura sono state successivamente osservate tramite il microscopio ottico LEICA DMI 5000 agli ingrandimenti 50X e 100X.

2.6 Microscopia a scansione SEM ed analisi EDS

L'osservazione delle fasi microstrutturali e l'analisi di composizione sono state eseguite tramite un microscopio SEM da banco "Phenom XL", equipaggiato con rivelatore di RX per l'analisi EDS. Al fine di rendere possibile l'analisi mediante irraggiamento elettronico i campioni metallici sono stati liberati dalla loro montatura plastica permettendo dunque la piena funzionalità delle loro proprietà di conduzione elettrica.

3. Risultati sperimentali

Al fine di individuare la migliore combinazione di potenza laser e di velocità di deposizione, la conformità delle singole 40 coppie di valori di F e P è stata valutata analizzando le deposizioni rispettivamente ottenute. Tramite un primo processo ad esclusione, si sono considerati come conformi i parametri di processo che fornissero deposizioni regolari, omogenee, la cui ZTA avesse valori contenuti, e che esibissero Melt Pools simmetrici e con dimensioni caratteristiche funzionali a garantire un corretto processo di sovrapposizione degli stessi. In base all'analisi delle cross-sections dei SLs, è stato scelto invece il valore di Hd ottimale, riscontrato in corrispondenza dei layers più densi e aventi migliore regolarità superficiale. I risultati ottenuti hanno dunque indicato i parametri di processo P 600W, F 750 mm/min e Hd 0.3 mm, come ottimali per eseguire operazioni di riparazione funzionali nel rispetto del miglior compromesso fra minimizzazione dei tempi di processo e risparmio di materiale. In ultimo luogo un'analisi più approfondita ha riguardato la detezione delle defettologie e l'osservazione delle caratteristiche microstrutturali nelle cross-sections dei 3 cubi costruiti impiegando i parametri di ottimizzazione appena riportati.

3.1 Morfologia delle SSTs

Tramite stereo-microscopia è stata condotta un'analisi on-top delle SSTs all'ingrandimento 10X, ottenendo una prima mappa di ottimizzazione nella quale distinguere le zone di processo non conformi da quelle conformi (Figura 6).

Dunque, la conformità morfologica delle SSTs è stata valutata secondo i due parametri di giudizio principali di:

- Omogeneità delle deposizioni
- Regolarità del profilo

Pertanto, dall'analisi dei risultati raccolti:

- a) si evidenziano due instabilità di processo in corrispondenza delle deposizioni 21 e 25 (contornate in blu) ottenute rispettivamente tramite le due coppie di parametri P 500W, F 900 mm/min e P 400W, F 3000 mm/min.
- b) si riconosce una finestra di non conformità in corrispondenza di valori medio bassi di velocità di scansione e alti valori di potenza laser impiegata. La stessa è stata contornata in colore rosso.

Le cause delle suddette defettologie sono state rispettivamente riconosciute in:

- a) – una probabile improvvisa accelerazione della testa di deposizione e/o in un non corretto approvvigionamento di polveri della zona di fusione da parte dei feeders.
 - una scarsa potenza laser non sufficiente a fondere le particelle di polvere flussate nell'unità di tempo resa disponibile dalla velocità di scansione.
- b) una troppo alta energia specifica che ha comportato un'interazione troppo severa con il substrato, dunque causando una alta ZTA e disomogeneità di deposizione in conseguenza di una troppo alta bagnabilità del materiale fuso.

	Laser Power				
	300 W	400 W	500 W	600 W	700 W
300 (mm/min)					
450 (mm/min)					
600 (mm/min)					
750 (mm/min)					
900 (mm/min)					
1050 (mm/min)					
1200 (mm/min)					
1350 (mm/min)					

Figura 6: SSTs all' ingrandimento 10X: conformi se contornate in verde (omogeneità di deposizione) non conformi se contornate in rosso (disomogeneità di deposizione).

3.2 ZTA delle SSTs

Volendo inoltre valutare l'omogeneità e la regolarità dell'interazione laser con il substrato, la zona termicamente alterata è stata misurata nella sua larghezza e quindi nella sua deviazione standard lungo il profilo delle tracce.

Più precisamente, non è stato possibile riferirsi a precisi valori soglia della ZTA su cui basare un'analisi di conformità ad esclusione.

Tuttavia, è stato possibile osservare che:

- la larghezza della zona termicamente alterata diminuisce con l'incremento della velocità di scansione a parità di potenza laser impiegata.
- la larghezza della zona termicamente alterata aumenta con l'incremento della potenza laser a parità di velocità di scansione.
- le SSTs

I risultati ottenuti sono stati dunque riportati:

- in Figura 7 ove indicati i valori della larghezza media della ZTA e delle relative deviazioni standard

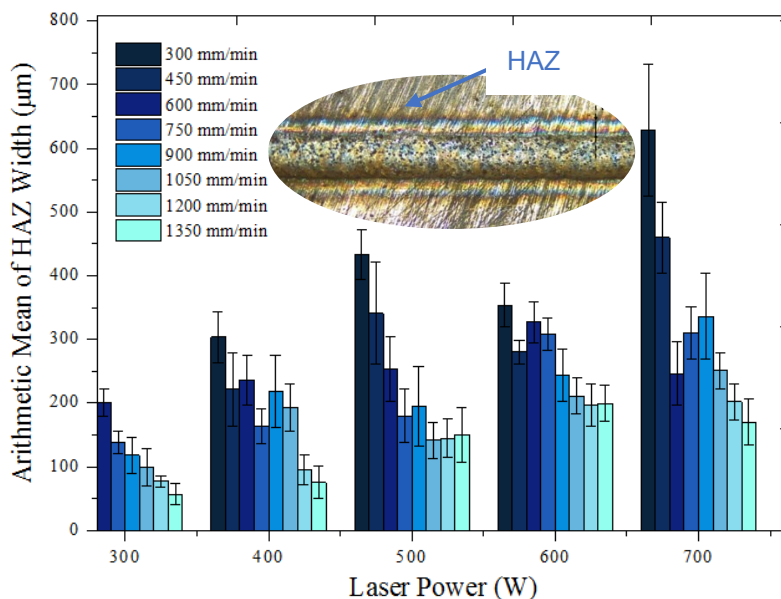


Figura 7: Media aritmetica "A" e Deviazione Standard "SD" della larghezza della ZTA in funzione della potenza laser P e della velocità di deposizione F

3.3 Analisi microscopica ottica dei "Melt Pools" attaccati chimicamente

L'analisi microscopica ottica delle cross-sections ha permesso di analizzare i pozzetti di fusione considerando come parametro chiave per ottenere una corretta sovrapposizione laterale e

trasversale delle tracce, la loro simmetria. Ulteriormente, sono state valutate le dimensioni principali dei “Melt Pools” al fine di valutare il grado di penetrazione e coerenza delle deposizioni con il substrato, oltre all’eventuale presenza di difettologie come il “Key holes” (difetto dovuto a interazioni troppo severe della sorgente laser con il substrato).

I parametri chiave di giudizio utilizzati in questo campo di analisi sono stati dunque:

- la simmetria dei pozzetti di fusione
- la valutazione delle dimensioni caratteristiche “Width”, “Bead Height” e “Fusion Depth” (Figura 8).

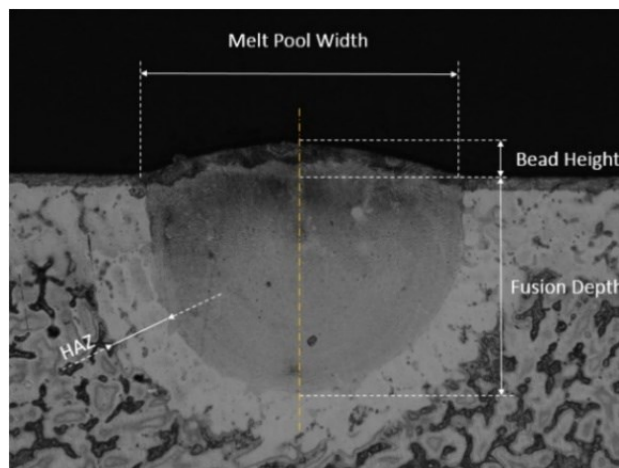


Figura 8: SST "37" e le sue dimensioni principali: Melt Pool Width, Bead Height, Fusion Depth e HAZ

I risultati dell’analisi geometrica di simmetria hanno dunque evidenziato (Figura 9):

- la non conformità di utilizzo della potenza laser 400W in corrispondenza della quale i Melt Pools delle SSTs 26, 27, 28, 29, 30, 31 e 32 mostrano evidenti asimmetrie geometriche.
- la parziale non conformità di utilizzo della potenza laser 300 W in corrispondenza della quale i Melt Pools delle SSTs 10, 11, 12, 13 mostrano asimmetrie geometriche.
- un'unica difettologia è stata riscontrata a 500W nel Melt Pool della SST 22.

La misura invece delle dimensioni caratteristiche ha evidenziato gli andamenti generali (Figure 10,11,12,13):

- la Bead height diminuisce a parità di P se il feed rate cresce
- la Width e la Fusion Depth aumentano se P aumenta a parità di F
- tutte e tre le caratteristiche diminuiscono all’aumento della velocità di scansione
- un'insufficiente decrescita del rapporto “Width” / “Fusion Depth” a causa di un troppo modesto valore di feed rate, che ha comportato melt pools aciculari e non geometricamente bilanciati
- un'insufficiente decrescita del rapporto “Width/Bead Height” a causa di un troppo modesto valore di feed rate, che ha comportato melt pools con bassi bead height e non geometricamente bilanciati.

Tuttavia, sebbene gli andamenti sopra citati risultano essere generalmente validi, diverse eccezioni sono state rilevate:

- le SSTs 8, 23, 33 e 37 mostrano una Width inferiore di quella attesa rispetto ai parametri impiegati
- le SSTs 1 e 21 mostrano una Fusion Depth inferiore di quella attesa.
- le SSTs 22, 23 e 28 mostrano valori sottostimati del loro rapporto Bead Height/Width a causa dell'alta velocità trasversale che fa decrescere il valore di Powder Density.

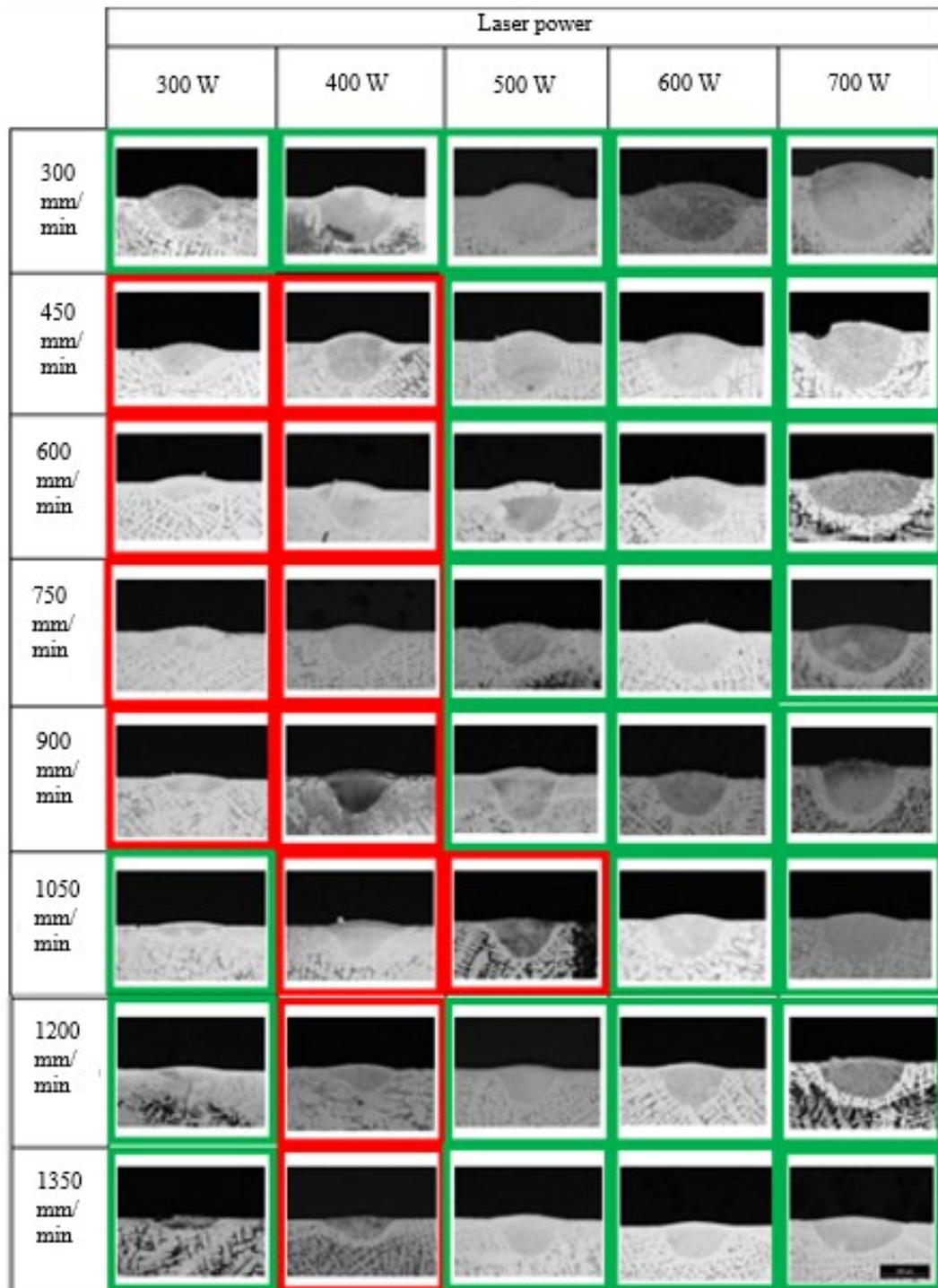


Figura 9: cross-sections dei "Melt Pools" attaccati chimicamente – Analisi ottica a 50X

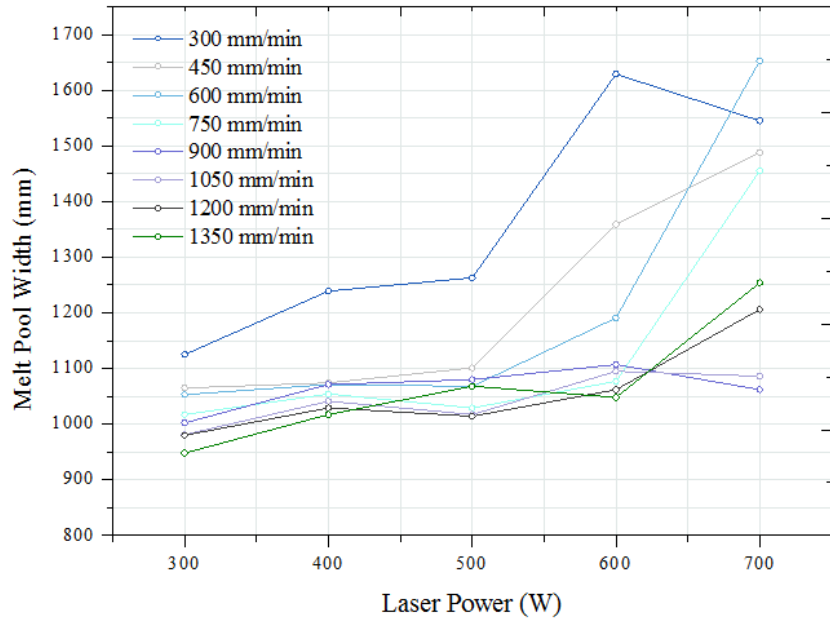


Figura 10: SSTs – Melt Pools' Width in funzione della potenza laser

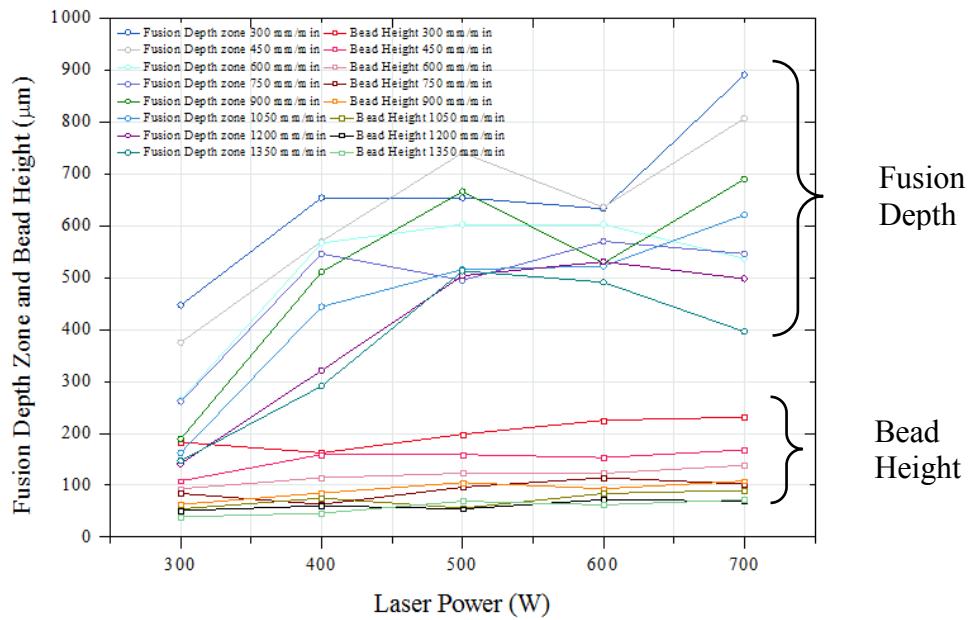


Figura 11: SSTs- Fusion Depth e Bead Height in funzione della potenza laser

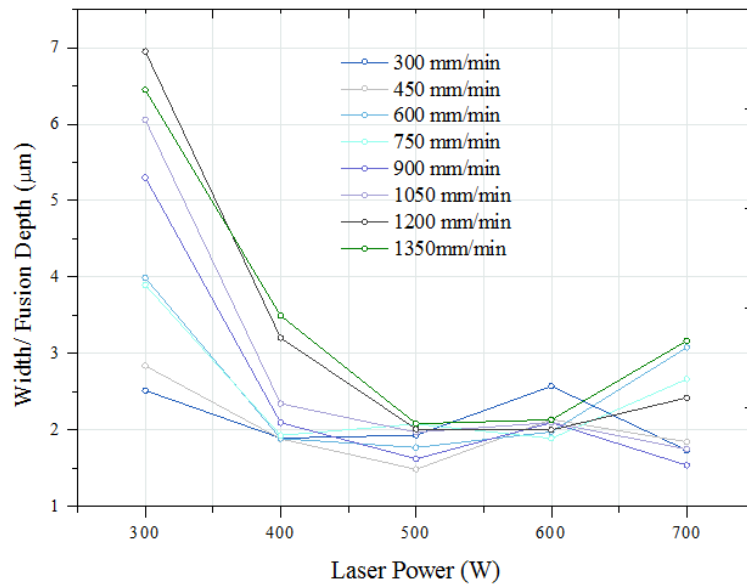


Figura 12: SSTs – rapporto fra Melt Pool width e Fusion Depth in funzione della potenza laser

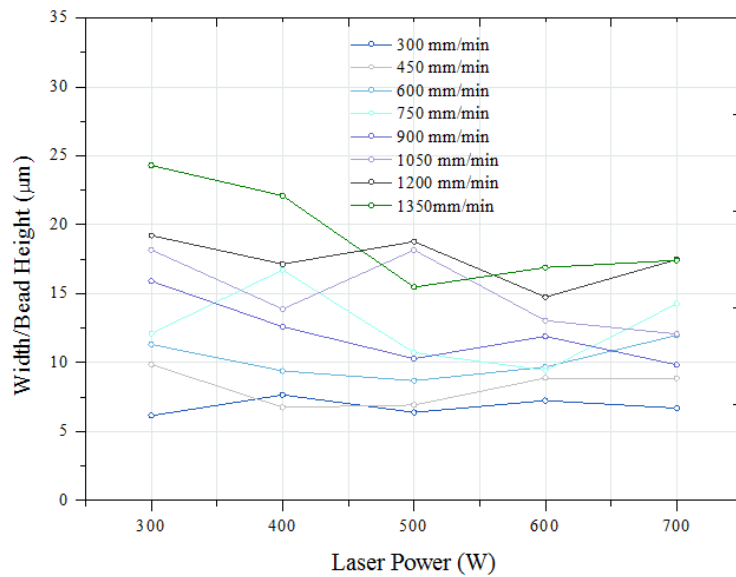


Figura 13: SSTs – rapporto fra Melt Pool width e Fusion Depth in funzione della potenza laser

Al fine di riassumere tutti i risultati di analisi ottenuti, si presenta in Tabella 1 una raccolta delle conformità e non conformità delle SSTs relativamente ai parametri di processo con cui le stesse sono state ottenute.

Tabella 1: Raccolta delle conformità e non conformità delle SSTs

Laser Power (W)	Feed Rate (mm/min)	SST number	Cross sectional analysis			Melt Pool coherence with the substrate		
			Process stability	SST regularity	Melt Pool	Width	F. Depth	B. Height
						●	✘	▲
600	300	1	●	✘	●	●	▲	●
	450	2	●	✘	●	●	●	●
	600	3	●	✘	●	●	●	●
	750	4	●	●	●	●	●	●
	900	5	●	●	●	●	●	●
	1050	6	●	●	●	●	●	●
	1200	7	●	●	●	●	●	●
	1350	8	●	●	●	▲	●	●
300	300	9	●	●	●	●	●	●
	450	10	●	●	✘	●	●	●
	600	11	●	●	✘	●	●	●
	750	12	●	●	✘	●	●	●
	900	13	●	●	✘	●	●	●
	1050	14	●	●	●	●	●	●
	1200	15	●	●	●	●	●	●
	1350	16	●	●	●	●	●	●
500	300	17	●	✘	●	●	●	●
	450	18	●	●	●	●	●	●
	600	19	●	●	●	●	●	●
	750	20	●	●	●	●	●	●
	900	21	✘	●	●	●	▲	●
	1050	22	●	●	✘	●	●	▲
	1200	23	●	●	●	▲	●	▲
	1350	24	●	●	●	●	●	●
400	300	25	✘	●	●	●	●	●
	450	26	●	●	✘	●	●	●
	600	27	●	●	✘	●	●	●
	750	28	●	●	✘	●	●	▲
	900	29	●	●	✘	●	●	●
	1050	30	●	●	✘	●	●	●
	1200	31	●	●	✘	●	●	●
	1350	32	●	●	✘	●	●	●
700	300	33	●	✘	●	▲	●	●
	450	34	●	✘	●	●	●	●
	600	35	●	✘	●	●	●	●
	750	36	●	●	●	●	●	●
	900	37	●	●	●	▲	●	●
	1050	38	●	●	●	●	●	●
	1200	39	●	●	●	●	●	●
	1350	40	●	●	●	●	●	●

- Compliancy
- ✘ Non-compliancy
- ▲ Deviation from the expected trend

In ultima istanza si evince dunque che:

- la potenza laser di 700W comporta un'interazione troppo severa con il substrato (quindi estesa ZTA ed inomogeneità di deposizione), dovuta a valori di energia specifica troppo alti e non opportunamente bilanciati con le velocità di deposizione considerate.
- la potenza laser di 400W produce deposizioni asimmetriche con pronunciata e irregolare ZTA.
- la migliore soluzione in termini di minimizzazione delle defettologie è rappresentata dalla scelta di velocità di scansione medio-alte che compensino l'energia specifica fornita e quindi minimizzino le inomogeneità e le irregolarità deposizionali.
- la migliore soluzione in termini di massimizzazione delle dimensioni caratteristiche è rappresentata dalla scelta di velocità di scansione basse, unitamente all'aumento del valore di feed rate (quantità di polvere flussata in unità di tempo).

Pertanto, si è riconosciuto per valori intermedi di velocità di deposizione e potenza laser, il miglior compromesso fra massimizzazione delle dimensioni dei Melt Pools e minimizzazione delle defettologie.

In ragione di quanto detto sono stati preselezionati come ottimali le coppie di valori

- P: 400W e 600W
- F: 750 mm/min e 900 mm/min

3.4 Analisi microscopica ottica dei "Layers" – Detezione delle defettologie

Le due coppie di valori identificati come ottimali dall'analisi delle SSTs, sono state impiegate per realizzare:

- 12 Layers impiegando P 600W e F 750/900 mm/min (Substrato 1) *
- * 4 di questi non sono stati analizzati poiché difettati
- 12 Layer impiegando P 400W e F 750/950 mm/min (Substrato 2)

L'analisi per microscopia ottica delle sezioni trasversali (non attaccate chimicamente) del Substrato 2 ha rivelato:

- il valore massimo di area percentuale delle defettologie dello 0.06%, in corrispondenza dei layers ottenuti impiegando F 750 mm/min.
- la dimensione media massima delle defettologie di 41,7 μm , in corrispondenza dei layers ottenuti impiegando F 900 mm/min.
- defettologie di forma prevalentemente circolare, in prima assunzione riferibili a una presenza promiscua di porosità e ossidi.

Le possibili cause che possono aver portato alla genesi di tali defettologie, sono state imputate:

- alla non adozione di "Shielding gas", la quale ha permesso all'ossigeno presente in atmosfera di formare ossidi
- all'intrappolamento di "Carrier gas" nel metallo fuso che ha così formato pori circolari
- alla presenza di porosità e ossidi nel feedstock di partenza che, una volta fuso, ha trasferito le sue defettologie alla parte.

Tuttavia, potendo considerare la presenza percentuale di difetti come modesta, gli stessi non sono stati considerati come uno dei parametri chiave su cui basare l'analisi di conformità delle deposizioni. Per questa ragione, la medesima analisi non è stata intrapresa anche per il Substrato 1.

3.5 Analisi microscopica ottica dei "Layers" – Analisi di coerenza delle deposizioni con il substrato.

La coerenza dei layers con il substrato è stata valutata osservando le cross-sections dei layers (attaccate chimicamente) nella loro morfologia. In particolare, sono stati valutati il grado di sovrapposizione laterale delle tracce e l'omogeneità di deposizione, in relazione ai valori di P ed F impiegati e in base alle due "Hatching distance" adottate di 0,3 mm e 0,4 mm.

Al fine di selezionare la migliore combinazione di parametri, la migliore deposizione del Substrato 1 e del Substrato 2, ottenute rispettivamente a 600W (e 900 mm/min, 0,4 mm) e a 400W (e 750 mm/min, 0,3 mm), sono state confrontate (Figura 9).

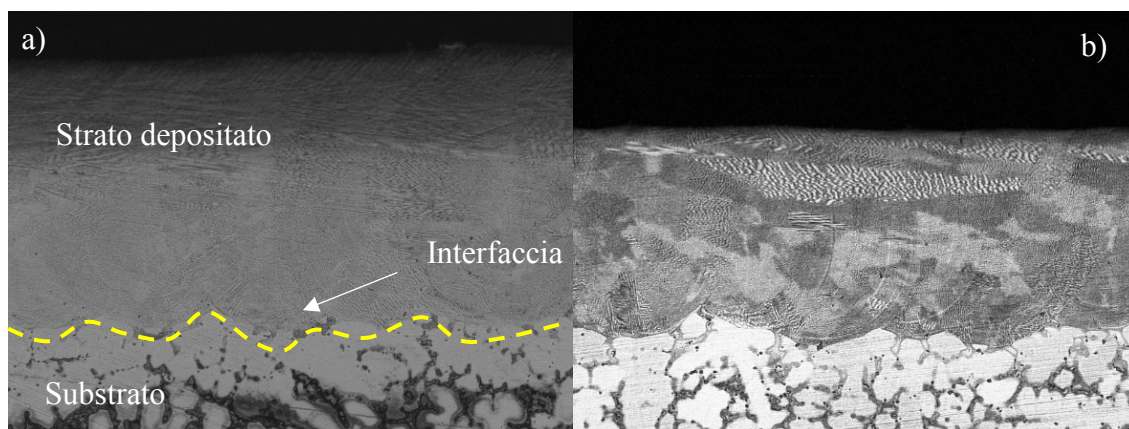


Figura 9: a) SLs 9 del Substrato 1 e b) 6 del Substrato 2 (a destra)

I risultati dell'analisi morfologica di confronto hanno pertanto rivelato:

- dimensioni caratteristiche dei melt pools superiori negli strati depositati a 600W
- superiore sovrapposizione laterale delle singole tracce depositate a 600W
- notevole disomogeneità morfologica delle deposizioni ottenute a 400W

In ragione di tali risultati, la potenza laser di **600 W** è stata selezionata come ottimale da impiegarsi per realizzare le caratteristiche in esame nella seguente campagna.

Infine, volendo massimizzare l'omogeneità deposizionale e la stabilità di processo, si sono scelti come parametri ottimali la velocità di deposizione F **750 mm/min** e la distanza di Hatching di **0,3 mm**. Infatti, sebbene tale scelta sia in contro tendenza con la ricerca della massimizzazione di produttività, si è scelto di porre l'enfasi sull'affidabilità di processo e minimizzazione delle defettologie vista la natura dell'applicazione e dei componenti da ripararsi. A parità di potenza laser infatti, più modeste velocità di deposizione comportano

aumento della Width dei Melt Pools la quale, unitamente a Hd ridotte, permette una più marcata giunzione laterale delle SSTs senza formazione di pori.

3.6 Analisi microscopica ottica dei “Cubes” – Detezione delle defettologie

A conclusione della campagna sperimentale, sono state analizzate le cross-sections di tre cubi depositati con i parametri di ottimizzazione precedentemente selezionati.

Similarmente all’analisi delle defettologie intrapresa per gli strati, i cubi sono stati osservati per microscopia ottica potendo così quantificare la loro area percentuale e dimensione media rispettivamente in 0,04% e 14,8 μm . Si è notato inoltre che tali valori si dimostrano essere pur inferiori a quelli trovati nei Layers (del Substrato 2) costruiti con gli stessi parametri di processo, fornendo dunque un ulteriore conferma che la potenza laser di 600W rappresenti la migliore scelta. In aggiunta, nessuna particolare defettologia come Keyholes o Lacks of fusion è stata riscontrata.

3.7 Analisi microscopica ottica dei “Cubes” – Morfologia della microstruttura

Tramite microscopia ottica, è stato inoltre possibile osservare la morfologia microstrutturale delle parti agli ingrandimenti 50X e 100X. Più precisamente l’analisi ha preso in esame le tre zone differenti del cubo: “Top”, “Core” e “Bottom”.

I risultati dell’analisi hanno pertanto fornito le seguenti osservazioni

“Bottom”

- dalla zona inferiore si estende verso il centro della parte una microstruttura dendritica colonnare e fine.
- la zona di interfaccia fra la parte e la base risulta essere omogenea, coerente e con una modesta ZTA (a differenza di quanto rilevato per la SST 4 ottenuta impiegando i medesimi parametri)

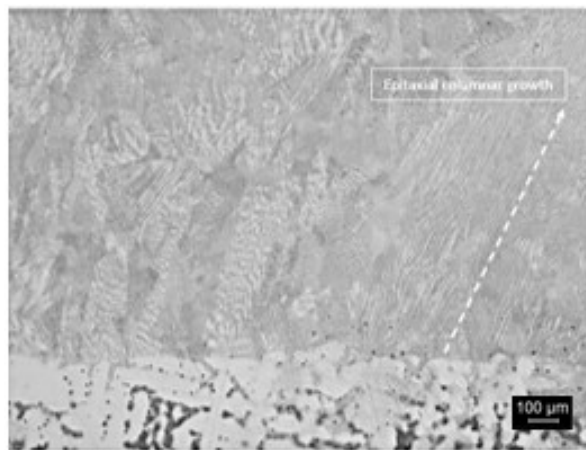


Figura 10: Crescita epitassiale e colonnare dendritica dal substrato verso il core della parte – Micrografia ottica a 50X

“Core”

- nel centro dei cubi non è stata rilevata presenza di difettologie come Lack of fusions o Key Holes
- una crescita colonnare dendritica attraversa coerentemente gli strati e le singole tracce sovrapposte suggerendo così una crescita epitassiale
- la strategia di deposizione insieme al forte carattere direzionale di solidificazione tipico del processo DED, hanno comportato una forte anisotropia microstrutturale testimoniata anche dall'effetto “stair-case” (Figura 11).

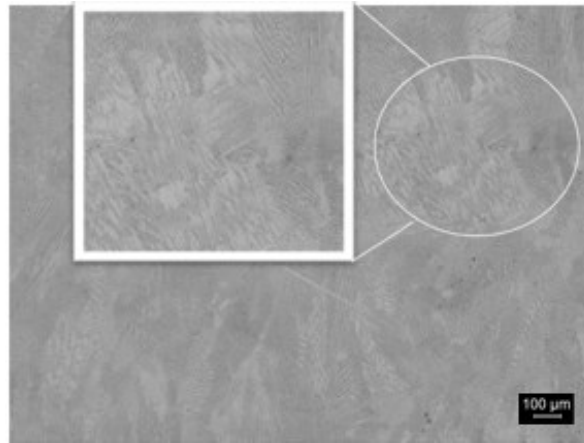


Figura 11: Effetto "stair case" in cui si distingue un netto cambio di direzionalità della microstruttura da un SL all'altro

“Top”

- nella zona in prossimità della superficie si è osservata una zona di transizione a demarcare la struttura colonnare proveniente dal centro del cubo e una microstruttura cellulare equiassiale situata in prossimità dei bordi. Tale variazione morfologica è in accordo con la diminuzione locale del rapporto G/R (Figura 12).

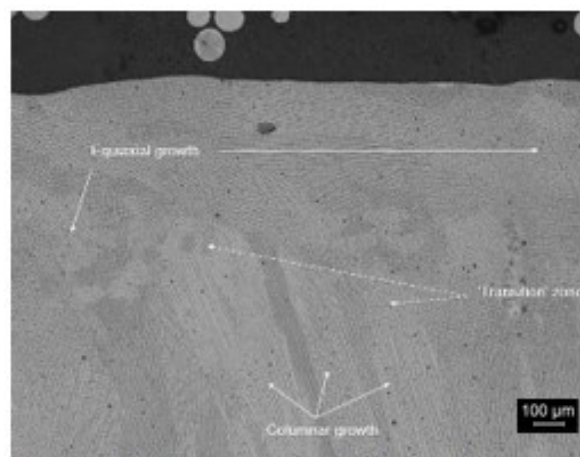


Figura 12: Micrograph of the etched Cube 6 top acquired at 100X (optical microscope) - transition from columnar to equiaxed microstructure.

3.8 Analisi microscopica a scansione ed EDS dei “Cubes”

Al fine di ispezionare più approfonditamente la microstruttura è stata eseguita un’analisi di microscopia a scansione nelle medesime aree analizzate tramite microscopia ottica. Eseguendo una mappatura dei campioni ai tre ingrandimenti 1000X, 2000X e 3000X, è stato possibile evidenziare:

- una rilevante presenza percentuale di fasi “Laves” inter-dendritiche seppur non quantificabile tramite i metodi di analisi utilizzati
- inattesa presenza di fasi “Laves” nelle aree prossime ai bordi delle caratteristiche, nonostante il basso gradiente termico locale.

Pertanto, la rimarcata anisotropia microstrutturale evidenziata dapprima dalla microscopia ottica e qui rimarcata dalla microscopia a scansione, indica una forte discontinuità delle proprietà del materiale. Per tale motivo, le caratteristiche “as-deposited” non possono costituire una soluzione pronta all’uso, ma piuttosto, prima della loro messa in opera si deve prevedere un trattamento termico al fine di dissolvere le fasi laviche e le spesso presenti fasi delta. Inoltre, al fine di identificare le fasi presenti all’interno delle parti, è stata condotta un’analisi EDS, la quale ha dimostrato la presenza di:

- Carburi dispersi nella matrice γ
- Ossidi di Ti e Al
- Fasi “Laves”
- Fasi delta
- Ossidi di Ti e Al all’interno dello strato di ossido che ricopre la superficie della parte.

4. Conclusioni

IN questo incarico di tesi è stata presentata una campagna sperimentale che ha interessato la caratterizzazione di tre caratteristiche: (SSTs, SLs e Cubes), realizzate in superlega a base Ni IN718 e fabbricate tramite la tecnologia di produzione additiva “Directed Energy Deposition” (DED) con alimentazione a polvere. Più nel dettaglio, 40 singole tracce sono state analizzate nel loro aspetto morfologico e nelle loro caratteristiche microstrutturali identificando così una prima finestra di conformità del processo. Successivamente, la caratterizzazione ha interessato le due più massive caratteristiche “SLs” e “Cubes”. Dai risultati ottenuti in laboratorio e dalle analisi eseguite si possono trarre le seguenti conclusioni:

6.1 SSTs

- L’analisi on-top delle SSTs ha riportato:
 - che tutte le SSTs mostrano regolarità del loro profilo eccetto le tracce no. 1, 2, 3, 17, 33, 34, and 35.
 - che le SSTs 21 e 25 sono state depositate non conformemente poiché testimoni di instabilità di processo
 - la Potenza laser di 700W causa una troppo severa interazione col substrato comportando quindi lo sviluppo di una ZTA troppo pronunciata
- L’analisi delle sezioni trasversali attaccate chimicamente delle SSTs ha riportato:
 - l’assenza di difettologie “Key hole”

- la notevole asimmetria dei pozzetti di fusione delle SSTs:
 - no. 26,27,28,29,30,31 and 32 (ottenute a 400W)
 - no. 10,11,12,13 (ottenute a 300W)
 - no. 22
- L'analisi delle dimensioni principali dei melt pools ha evidenziato:
 - la progressiva diminuzione della "Fusion depth", "Width" e "Bead Height" dei melt pools all'incremento della velocità di scansione a parità di potenza laser impiegata
 - la "Width" e la "Fusion Depth" crescono se la potenza laser power P cresce a parità della velocità di scansione
 - la "Bead Height", quindi la "layer thickness" diminuisce a parità di P se la velocità di scansione cresce
 - un valore di feed rate non conforme per alimentare la testa di deposizione che ha comportato valori dei rapporti "Fusion Depth/Width" e "Bead Height Width" notevolmente scostati dal valore ideale "1" e quindi indicanti melt pools non bilanciati nelle loro dimensioni principali.
- Tutte le non conformità rilevate delle SSTs sono state riassunte in Tabella 1
- In conseguenza dell'analisi delle non conformità si è dunque dedotto che:
 - i valori medi di velocità di scansione 750,900 mm/min e I valori medi di potenza laser,600W sono da considerarsi nel caso applicativo considerato come ottimali
 - la miglior soluzione in termini di minimizzazione delle defettologie è perseguibile tramite l'adozione di valori di velocità di scansione medio alti che ben compensino l'energia specifica fornita nell'unità di tempo
 - la miglior soluzione in termini di massimizzazione delle dimensioni caratteristiche dei melt pools è perseguibile tramite l'adozione di basse velocità di scansione e un maggiore feed rate di quello adottato.

- **6.2 SLs**

L'analisi ottica delle cross-sections dei "SLs" non attaccati chimicamente ha rivelato:

- La presenza di due tipi di defettologie: "ossidi" e "pori", tuttavia non distinguibili nelle loro quantità relative tramite le metodologie di analisi usate
- La massima area percentuale dei difetti di 0,06%, rilevata in corrispondenza dei "SLs" costruiti con F 750 mm/min (Substrato 2)
- La massima taglia media dei difetti di 41,7 μm , rilevata in corrispondenza dei "SLs" costruiti con F 900 mm/min (Substrato 2)
- Considerando la modesta presenza di defettologie, non si è ritenuto necessario replicare la stessa analisi per il Substrato 1

L'analisi ottica delle cross-sections attaccate chimicamente ha evidenziato:

- superiorità di caratteristiche microstrutturali e morfologiche dei "SLs" costruiti a 600W
- superiorità di sovrapposizione laterale delle single trace costituenti i "SLs" costruiti a 600W

- forte inomogeneità delle deposizioni ottenute a 400W
- la Potenza laser di 600W rappresenta il valore di P ottimale da adottarsi nel caso applicativo considerato
- la “hatching distance” Hd di 0,3 mm e la velocità di scansione F of 750 mm/min come coppia di parametri adatta a minimizzare le defettologie e massimizzare la produttività.

- *6.3 Cubes*

L’analisi ottica delle “cross-sections” attaccate chimicamente ha rivelato:

“Bottom”

- una crescita dendritica colonnare che si protende a partire dal substrato fino al centro della parte
- che l’interfaccia compresa fra il substrato e la parte è omogenea e coerente mostrando una ZTA ridotta

Core

- l’assenza di defettologie tipiche quali “Key hole” e “Lack of fusion”
- che la crescita dendritica attraversa le diverse tracce e strati all’interno della parte a suggerire una crescita epitassiale
- che la strategia di scansione unitamente al forte carattere di solidificazione direzionale tipico del DED, hanno comportato una forte anisotropia microstrutturale.

Top

- una zona di transizione nelle vicinanze dei bordi delle parti, a ripartire una crescita cellulare equiassica da una dendritica e colonnare

L’analisi SEM/EDS ha invece riportato:

- una considerevole presenza di fasi “Laves” nelle regioni interdendritiche non direttamente quantificabili mediante le metodologie di analisi utilizzate
- presenza di fasi di “Laves” in prossimità della superficie nonostante questa in costruzione fosse interessata da modesti gradienti termici locali
- presenza di carburi ricchi in Nb e Ti dispersi nella matrice γ
- presenza di ossidi di Ti e Al
- fasi “delta”
- ossidi di Ti e Al nello strato di ossido ricoprente la parte; di spessore 72 μ m e 15 μ m rispettivamente sulla sommità e sulle pareti.

Per concludere, i parametri di ottimizzazione scelti al fine di massimizzare l’efficienza del processo DED sono: potenza laser P di 600W, velocità di scansione F di 750 mm/min e Hatching distance di 0,3 mm.

Abstract

In this Thesis assignment, the goal was to find the optimum process parameters to produce Inconel 718 alloy via Directed Energy Deposition (DED). Therefore, for this purpose, the experimental analysis considered three different steps in which the optimum process parameters are achieved step by step. More in detail, the characterisation regarded: 40 “Single Scan Tracks” (SSTs), 24 “Single Layers” (SLs) and 3 “Cubes”. Indeed, the laser-related parameters like laser power (P), laser scan speed (SS) were selected according to the SSTs analysis, whereas the optimum hatching distance (Hd) was estimated according to the SLs. The best melt pool in terms of residual defect and geometrical regularity was chosen as the best-deposited melt pool, and accordingly, the process parameters associated with that melt pool were selected as the optimum parameters. Thereafter, the best Hd were considered according to the cross-section analysis of SLs in which the densest SLs with the most surface regularity revealed the optimal Hd. The outcomes show that P 600W, F 750 mm/min and Hd 0.3 mm, are the optimum DED process parameters to fabricate In718 parts. All in all, it can be concluded that this method of optimisation of process parameters is very promising to be implemented for optimisation of process parameters. It means, through the SSTs and SLs analyses, it would be possible to develop the process parameter of IN718 in a short and economical way without wasting time and material.

1. Introduction

Defined by “McKensey &Company” as one of the co-protagonist of the “Ops 4.0 Revolution”, Additive Manufacturing (AM), in the same way as Big Data science, advanced analytics, robotics and artificial intelligence, proposes itself as one of the leader sectors that will boost the productivity by the 20% in the next years (McKinsey&Company, 2018). AM thanks to its features of flexibility, versatility and its various advantages, has found fertile soil in varied and countless technological fields in which its impact has been defined by several authority figures “Disruptive”!

In the face of all the different types of AM families, Metal Additive Manufacturing is one of the most promising technologies that attracted considerable interest from the R&D divisions of some most essential Leaders companies in the Aviation field such as “GE” and “Siemens”.

This Master Thesis assignment concerns about the broad and ambitious framework of the European Project “4DHybrid”, which aims to “*develop a new concept of Hybrid Additive Manufacturing based on the modular integration of compact, low-cost modules including laser source, deposition head, sensors and control*”. Also, in cooperation with “GE”, “Siemens” and “Globotics Industries”, the solutions will be tested (European Project ‘4D Hybrid’, 2019).

The contribute here provided, pursues the goal to provide a process parameters optimisation concerning a campaign dealing with the Nickel-based Superalloy IN718. The features in question are IN718 Single Scan Tracks (SSTs), Single Layers (SLs) and Bulks (Blks) deposited on a not-preheated IN718 substrate as well, by Direct Energy Deposition (DED). The “SUPSI” Swiss University has furthermore performed the deposition operations.

First of all, is presented bibliographic research so that it was possible to introduce the overall framework highlighting the main issues related to the Metal AM for what concerns its employment within the Aviation-Aerospace field. Pursuing this purpose, a comparison between the two leading Metal AM families, Powder Bed (PB) and Direct Energy Deposition (DED), has also been provided. More specifically, the two different types of technology, have been compared in their advantages and disadvantage as well as in their process hallmarks and parameters.

Secondly, it has been taken into account also a deepening on the Ni-based Superalloys concerning their chemical composition through their history and distinguishable features that make them so fundamental for the applications in this Thesis considered. Finally, the Ni-based Superalloys have been studied explicitly regarding their IN718 class when manufactured by DED.

Thirdly, “Materials and Methods” employed during the characterisation, have been discussed and detailed, wanting to explain better how practically it has been possible to get hold of the results obtained.

Finally, the results concerning the different features characterisation, just above mentioned, have been widely discussed in terms of their Defectology as well as their Morphological, Microstructural aspects.

More in detail, for the SSTs a porosity detection as well as a regularity and a microstructural analysis, has been accomplished. Besides, the Single Layers, have been characterised in their superficial roughness, porosity content and morphology and microstructure. Finally, a porosity analysis and a microstructural study have been figured out.

2. Metal Additive Manufacturing

2.1 Introduction

In the face of all the manufacturing technologies developed nowadays available in the market, the Additive Manufacturing seems to represent one of the most promising productive technology that will have a disruptive impact in the manufacturing world in the next years.

Unlike from the Subtractive Manufacturing, the AM is a manufacturing process based on the assumption of adding material only where needed, instead of subtracting it from a raw or a bulk material as well, to realise complex parts. More specifically, the ASTM F2792 – 12, defines the AM as *“a process of joining materials to make objects from 3D model data, usually layer upon layer, as opposed to subtractive manufacturing methodologies”* (Gibson, Rosen and Stucker, 2013).

According to this definition, it is possible to guess the AM innovativeness and how this process can lead to breaking the mould mindset in design.

In a more and more demanding market characterised by a fierce competition to provide performant and ecofriendly solutions, costs minimising, time-saving, reliability and on-demand production, are only a few of the requirements requested by retailers and customers. At this purpose, the AM also known as 3Dprinting thanks to its varied hallmarks, propose a wide range of techniques and technical solutions times to fulfil these expectations in several fields.

Wanting to mention only two of all the relevant fields in which AM has been successfully employed so far, there is no doubt that the Aviation and the Aerospace sectors have offered to this technology fertile soil to play its cards.

Although not yet arrived in its maturity, the 3Dprinting seems to be more than willing to face with hard challenges where, aside from the already mentioned, smart production, weight-saving and tailored manufacturing are pivotal points.

Another critical parameter that makes this manufacturing process noteworthy is its attitude to smartly process varied materials classes thanks to its diversification in a variety of apparatus. Although the material availability for AM is still an open field, up to seven different types of AM apparatus capable of manufacturing components in polymeric, composites, ceramic and metallic materials as well, are nowadays recognised by the ASTM F2792 – 12 (Gibson, Rosen and Stucker, 2013).

As an example, in the Aviation field just mentioned before, a climax opportunity for AM is represented by the exigency to optimise the Ni Superalloys based components in weight, performances, damage tolerance and assembly simplification. In this chapter, a brief history of AM and Ni Superalloys as well will be at first reported as a starting point to introduce the basic principles on which this technology and material specialised. Secondly, the main AM categories will be briefly listed and detailed in their features according to the ASTM Standards. Finally, a typical Additive Manufacturing process will be illustrated and explained since the 3D CAD designing up to the part realisation.

2.2 Brief AM “Pre-History” and “History”

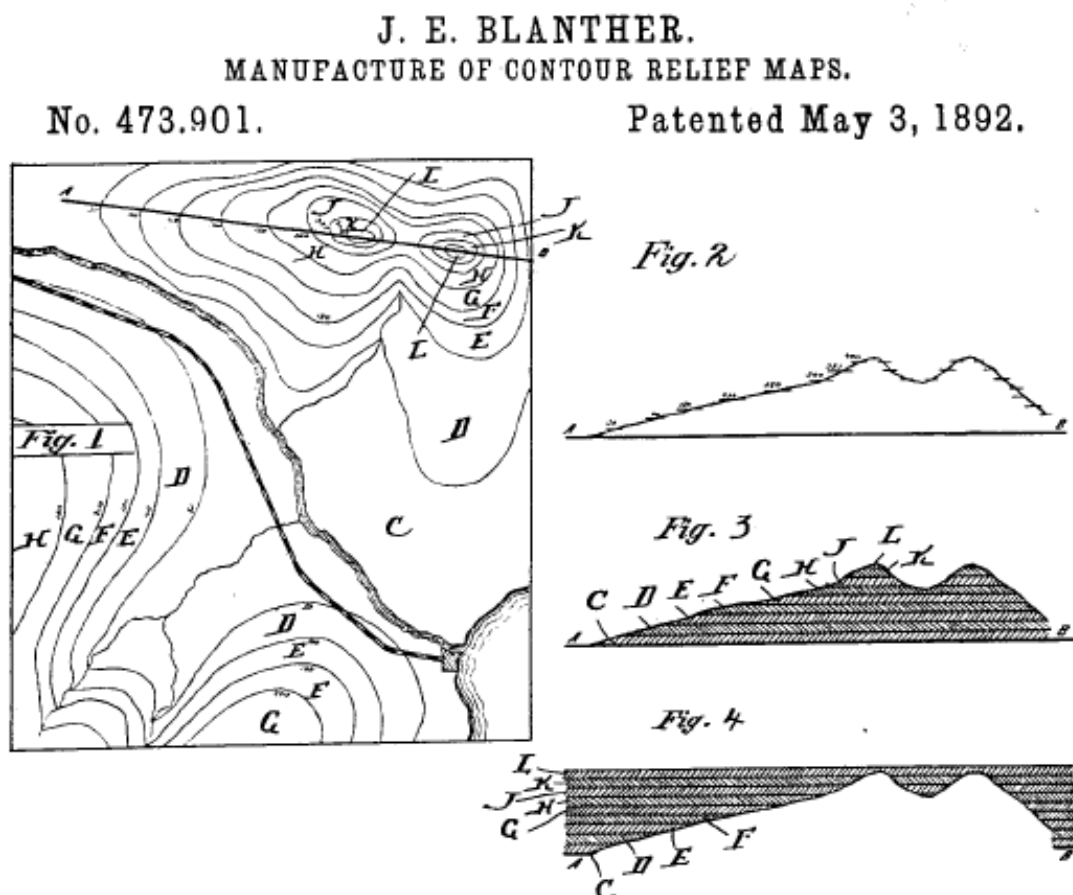
As widely known, the Charles W. Hull patent filed in 1984 conventionally marked the Additive Manufacturing birth.

More specifically, according to what reported by Michael Molitch-Hou, Mr Chuck Hull was recognized as the inventor of AM after that GE France and CILAS abandoned the patent deposited by their workers Alain Le Méhauté, Olivier de Witte, and Jean Claude André just three weeks before that Mr Chuck did it (Molitch-Hou, 2018).

However, these events and patents refer to the AM birth and to how this technology is nowadays conceived, but not to its more atavic roots!

According to Joseph J. Beaman, the Solid Freeform Fabrication (SFF), more widely known as Rapid Prototyping (RP) and as a subcategory of AM, has its roots in Topography and Photo sculpture (Beaman, 2001),(Bourell *et al.*, 2009).

In 1892 J.E. Blanthier filed a patent of a manufacturing process times to realise layered wax moulds employable to report reliefs on topographical maps. Recreating the 3D profile desired by jointing wax layers appropriately shaped and dimensioned, J.E. Blanthier was able to create two halves wax mould respectively split into a “negative” and “positive” shape. After the mould backing, it was so possible to realise raised relief maps by squeezing a map sheet between the two mould halves (Figure 2.1) (Beaman, 2001).



Carlo Baese’s invention concerning Photo sculpture constitutes another climax example of rapid prototyping insight. In 1904 Baese filed its patent of the “*Photographic Process for the reproduction of plastic objects*” (Figure 2.2). The purpose of this invention was to realise a faithful reproduction of an object irradiating it and impressing layers of a photosensitive gelatin mixture, which expanded underneath the deflected light effect whether treated with water. The overlapping of the several layers realised, provided a 3D reproduction of the object to be copied (Beaman, 2001),(Carlo Baese, 1902).

No. 774,549. PATENTED NOV. 8, 1904.
 C. BAESE.
 PHOTOGRAPHIC PROCESS FOR THE REPRODUCTION OF PLASTIC OBJECTS.
 APPLICATION FILED MAY 17, 1902.
 NO MODEL. 3 SHEETS—SHEET 1.

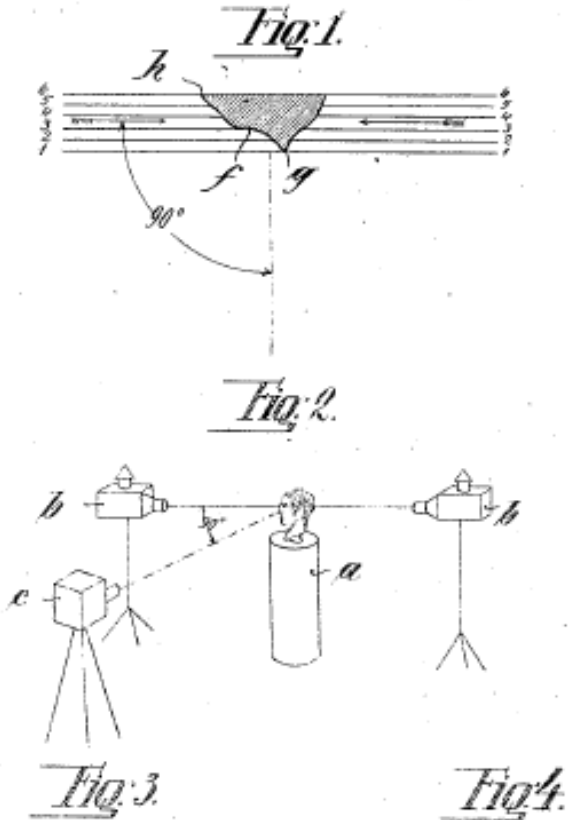


Figure 2.2: C. Baese patent No 774,549 (Carlo Baese, 1902)

After around seventy years from Baese’s invention, Wyn Kelly Swainson proposed a new way of conceiving the “Additive” approach. In 1968 [5] (patent filed in 1977) Swainson invented a new technology dedicated to producing 3D parts thanks to a complex system equipped with sophisticated tools such as interferometers, lasers and a computer unit (Figure 2.3). In this instance, the object to be reproduced was subjected by a laser scan actuated by one or multiple interferometers. Thereby, employing conductors and sensors, was possible to forward electronic signals to a double laser system hence able to reproduce a path following the original

object to be copied. Furthermore, the two laser beams controlled by galvanometer-mirror systems were projected through a photosensitive bi-component means generally polymeric. The new object was therefore built with a layer by layer approach by either degradation or curing [8].

Despite the advancement in technology, what seems to mark the line with the two previous inventions mentioned, are the purposes expressed by Swainson in its patent. In the face of all the objectives for which this technology should have been suitable for, could be remarkable notice his purpose to “provide a three-dimensional optical memory store for computer applications with the advantage of rapid operation and large volume data capacity.”

(Swainson, 1971).

Despite the advancement in technology, what seems to mark the line with the two previous inventions mentioned, are the purposes expressed by Swainson in its patent. In the face of all the objectives for which this technology should have been suitable for, could be remarkable notice his purpose to “provide a three-dimensional optical memory store for computer applications with the advantage of rapid operation and large volume data capacity”

(Swainson, 1971).

Therefore, although according to J.J. Beaman, no commercial solutions were available at that time, it can be nevertheless recognised in Swainson’s words, the intention to dedicate his discoveries to a manufacturing finality (Beaman, 2001).

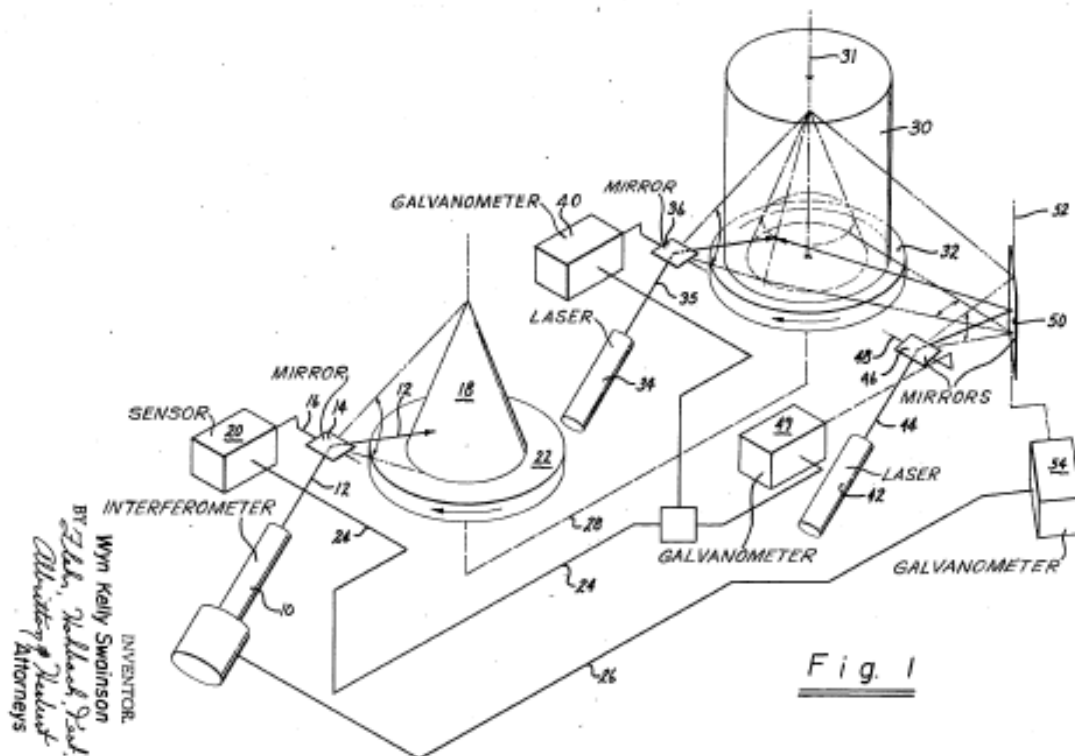


Figure 6.3: Swainson's patent No. 4,041,476 (Swainson, 1971)

In 1971 (Beaman, 2001) (patent filed in December 1972), Pierre Alfred Leon Ciraud proposed a new type of SFF technology that unlikely from his predecessors mentioned, expected to use a powder material to be melted, hence jointed, thanks to one or more laser sources. Almost all weldable materials were, therefore, employable to realise complex shapes with a layer by layer approach, as shown in Figure 2.4 (Pierre Alfred Leon Ciraud, 1972). Furthermore, from the equipment described in Ciraud's patent, unmistakable signs of commonality with the modern Direct Energy Deposition (DED) process can be recognised.

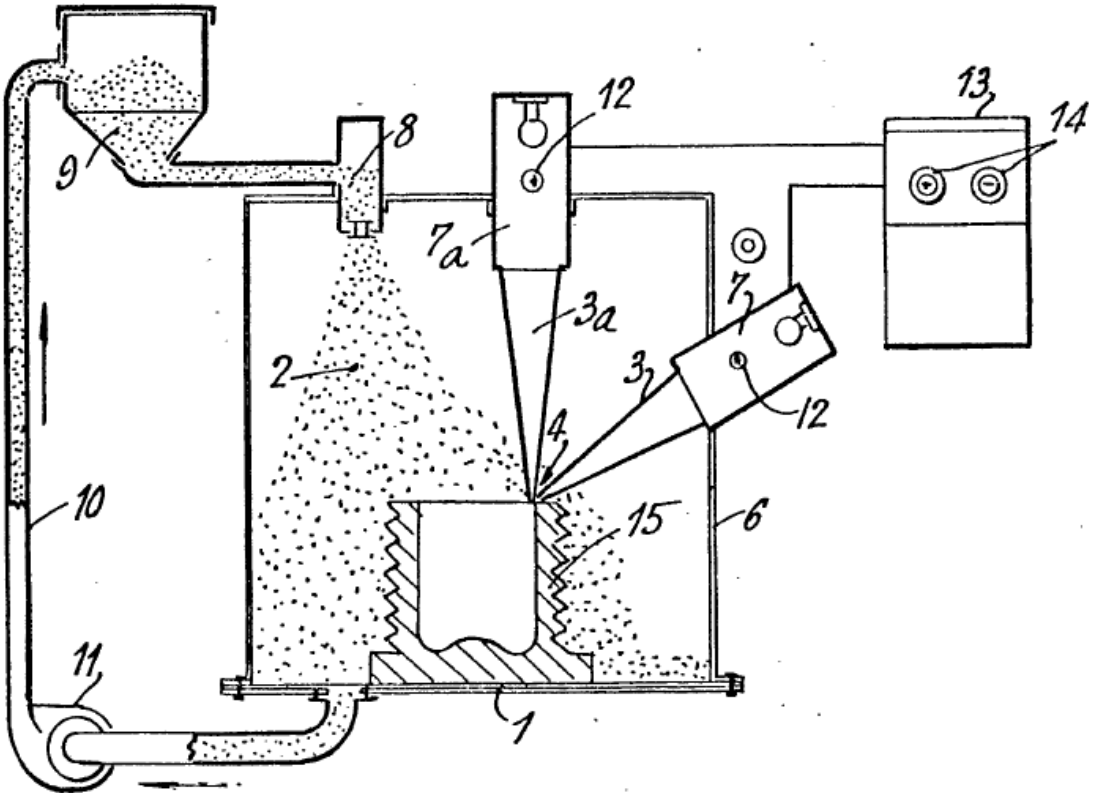


Figure 2.4: Ciraud's Invention scheme (Pierre Alfred Leon Ciraud, 1972)

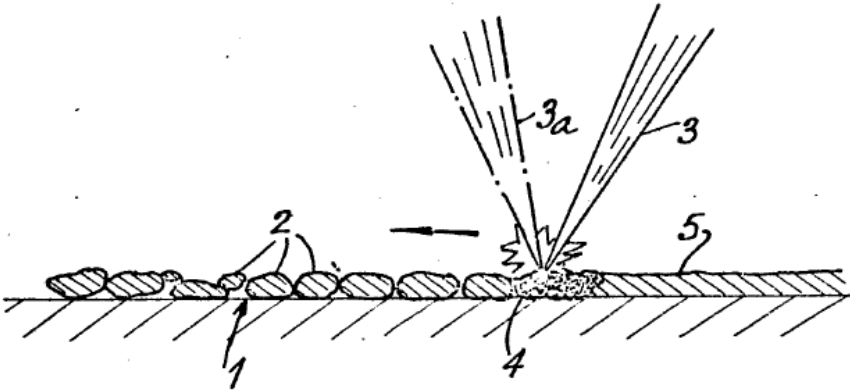


Figure 2.5: Ciraud's layer by layer approach (Pierre Alfred Leon Ciraud, 1972)

After Ciraud, several authority figures and inventors such as Housholder (1979), Kodama (1981) and Herbert (1982) filed their patents. Housholder conceived a sort of SLS apparatus equipped with a laser source and a mirrors system which deflecting the laser spot onto a powder bed selectively sintered the granules. On the other hand, Kodama provided a new apparatus times to cure photosensitive polymers by UV exposure. Three were the different approaches exploited to pursue a layer by layer vat photopolymerization (Beaman, 2001). The first two procedures, expected to cure the polymer thanks to a UV source projected through a mask placed respectively either on the top or at the bottom of the tank collecting the liquid resin (Beaman, 2001). With this shrewdness, it was so possible to cure the polymer and realise 3D objects by the overlapping of different dense polymer sections. Otherwise, the third approach considered to exploit an optical fibre animated on a plan to cure polymer layers successively (Beaman, 2001).

Finally, also Herbert realised his vat polymerisation apparatus in the same period. However, in this instance, the energy source was a laser beam conveyed from the top downwards into the resin vat, controlled by a computer device as it happens in a today SL apparatus even though in this case the new resin was added time after time (Bourell *et al.*, 2009).

Completing the circle, as just mentioned before, in 1984 Alain Le Méhauté, Olivier de Witte, and Jean Claude André and just three weeks after Chuck Hull filed their vat polymerisation patents. Is in 1986 that Chuck Hull founded the worldwide known 3D Systems company (Molitch-Hou, 2018) which first introduced in 1987 the “.STL” format file nowadays broadly employed as communication language between 3D CAD software and almost all AM devices (Wong and Hernandez, 2012).

Entering in the “modern era”, a plethora of new AM machines based on varied concepts have been invented, that quickly caught on the market scene.

In 1992 “Stratasys” was founded and thanks to S. Scott Crump the market knew the Fusion Deposition Modeling (FDM) technology. Based on the extrusion of thermoplastic materials, this technology allowed to realise 3D plastic parts by deposition of a melted polymeric cord thanks to a nozzle displaced through a 3D axis path. In the same year, before being acquired by “3D Systems” in 2001, “DTM Corporation” spread out on the market its SLS technology times to selectively sinter layers into a polymeric powder bed. In 1994, “Electronic Optical Systems” (EOS) launched into the market its SLS machines early becoming one of the most significant Additive Manufacturing company in the world. Two years later was the turn of the Binding Jet technology (BJ), first invented by the MIT and then made commercially available by “Z Corporation” these machines were capable to build 3D parts releasing binder as well as ink droplets into a gypsum powder bed consolidating the object layer by layer (Molitch-Hou, 2018). Wanting to mention the commercialisation of metal AM machines directly, it results preliminary to mention the availability on the market of the Powder Bed (PB) technologies. In 1995, “EOS” was the first to provide the manufacturing world of a powder bed metal technology termed as Direct Metal Laser Sintering (DMLS). In the same period, also the “Fraunhofer Institute for Laser Technology” provided a usable metal AM technology: The Selective Laser Melting (SLM). Unlikely from DMLS, the SLM apparatus melted the particles together instead of leads them to be joined by sintering phenomena due to laser exposure. As a result, the parts built did not need post-processing to aim for higher material densification (Molitch-Hou, 2018).

Not much later, in 1997 was founded the “Arcam EBM” company which already in early 1993 filed a patent describing a technological process able to melt metal particles using an electron beam source. However, the birth of the Electron Beam Technology (EBM), a subset of the PB technology, is imputable to the company cooperation with the “Chalmers University of Technology” in Gothenburg. The company released the first production model in 2002 (Arcam EBM, 2019).

In the same 1997, F. G. Arcella developed the Direct Energy Deposition (DED) at “Johns Hopkins University” and then commercialised his new apparatus through “AeroMet” (Molitch-Hou, 2018).

To conclude, thanks to J.J. Beaman and wanting to summarise the events just mentioned, it has been reported a tree charts to better display their temporal collocation in Figure 2.6.

TOPOGRAPHY		PHOTOSCULPTURE	
Blanthier patent filed	1890	1860	Willeme photosculpture
Perera patent filed	1937	1902	Baese patent filed
Zang patent filed	1962	1922	Monteah patent filed
Gaskin patent filed	1971	1933	Morioka patent filed
Matsubara patent filed	1972	1940	Morioka patent filed
DiMatteo patent filed	1974	1951	Munz patent filed
Nakagawa laminated fabrication of tools	1979		
	1968		Swainson patent filed
	1972		Ciraud disclosure
	1979		Housholder patent filed
	1981		Kodama publication
	1982		Herbert publication
	1984		Maruntani patent filed, Masters patent filed, Andre patent filed, Hull patent filed
	1985		Hellsys founded Denken venture started
	1986		Pomerantz patent filed, Feygin patent filed Deckard patent filed, 3D founded, Light Sculpting started
	1987		Fudim patent filed, Arcella patent filed, Cubital founded DTM founded, Dupont Somos venture started
	1988		1st shipment by 3D, CMET founded, Stratasys founded
	1989		Crump patent filed, Hellinski patent filed Marcus patent filed, Sachs patent filed EOS founded, BPM founded
	1990		Levent patent filed, Quadrax founded, DMEC founded
	1991		Tejlen Seiki venture started Foeckele & Schwarze founded, Soligen founded Melko founded, Mitsui venture started
	1992		Penn patent filed, Quadrax acquired by 3D Kira venture started, Laser 3D founded
	1994		Sanders Prototyping started
	1995		Aaroflex venture started
	1997		Aeromet formed, Optomec restarted, Z Corp started
	1998		Objet founded
	1999		POM founded, BPM closed
	2000		Hellsys closed, Solidica started
	2001		3D and DTM merge

Figure 2.6: Some chronological events of AM Pre-History and History (Beaman, 2001)

2.3 Additive Manufacturing Technologies and Standards

So that is possible to communicate worldwide about materials, products, systems and services avoiding misunderstandings and communicating with a universal technical language, it results somewhat important to adopt conventions and standards. In the interest of individuals and collective, the ASTM International (one of the largest not-for-profit developing standards organization in the world) defines and spread shared conventions in cooperation with suppliers, companies, several institutions and more, in general, all the stakeholders (ASTM International, 2019a). Wanting to introduce the main AM technologies classes nowadays available, are therefore reported in this paragraph the ASTM standards regarding the Additive Manufacturing distinction in seven different processes classes described in the ISO/ASTM 52900:2015 (ASTM International, 2019b):

- **Binder Jetting:** AM process in which a liquid bonding agent is selectively deposited to join powder materials
- **Directed Energy Deposition:** AM process in which focused thermal energy* is used to fuse materials by melting as they are being deposited.
** “Focused thermal energy” means that an energy source (e.g. laser, electron beam, or plasma arc) is focused to melt the materials being deposited.*
- **Material extrusion:** AM process in which material is selectively dispensed through a nozzle or orifice.
- **Material Jetting:** AM process in which droplets of build material* are selectively deposited.
**materials include photopolymer and wax.*
- **Powder Bed Fusion:** additive manufacturing process in which thermal energy selectively fuses regions of a powder bed.
- **Sheet lamination:** AM process in which sheets of material are bonded to form a part.
- **Vat photopolymerization:** AM process in which liquid photopolymer in a vat is selectively cured by light-activated polymerization (ASTM International, 2019b).

2.4 Additive Manufacturing Advantages and Disadvantages

Since this new technology entered in the Hi-Tech field, and then into the market, it has introduced great opportunities and opened new horizons so representing a more efficient and sophisticated way to manufacture goods. Nevertheless, the A.M. great potential can be insight by the fact that its equipment embeds in synergy, a relevant bunch of the most advanced technologies and systems nowadays available to achieve the most advanced manufacturing performances possible. In support of what just said, almost all the A.M. apparatus own sophisticated technologies such as laser sources, vacuum or inert gas systems, piezoelectric actuators, thermal sensors. Furthermore, another significant part of hallmarks and benefits derives from the AM nature based on the composition of those as mentioned earlier “hard” technologies with the digital world. The alignment of the two provides an enormous versatility. According to that, it found, therefore, explain the reason why of its branched development tapping into a manifold and so different sectors such as the Aviation, Aerospace, Automotive and Biomedical ones.

Since its young birth, the industrial and scientific community broadly shared the forecast of the exponential growth of AM By 2023, thanks to essential and substantial investments undertaken by the 3D apparatus suppliers companies to overcome the building volume and production

speed constraints, a production saving of around 50% on the built parts in conjunction with a production speed increase of 400% are expected (Figure 2.7) (Attaran, 2017).

However, despite its remarkable innovativeness and efficiency, several studies highlight quite clearly that the AM potential is not appointed to either replace or subtract domains to the traditional manufacturing, but rather to affirm itself in very specialised and demanding realms. A climax example of how AM can make feasible to adopt applications never supposed before, can be represented by the study carried out by NASA on zero gravity AM aiming to provide the astronauts with on-demand manufacturing when in mission (Attaran, 2017).

Wanting to directly and specifically address the reader to the main overall advantages and disadvantages (or else constraints), is here just below presented a summary of the most important aspects to be considered while assessing the AM employability.

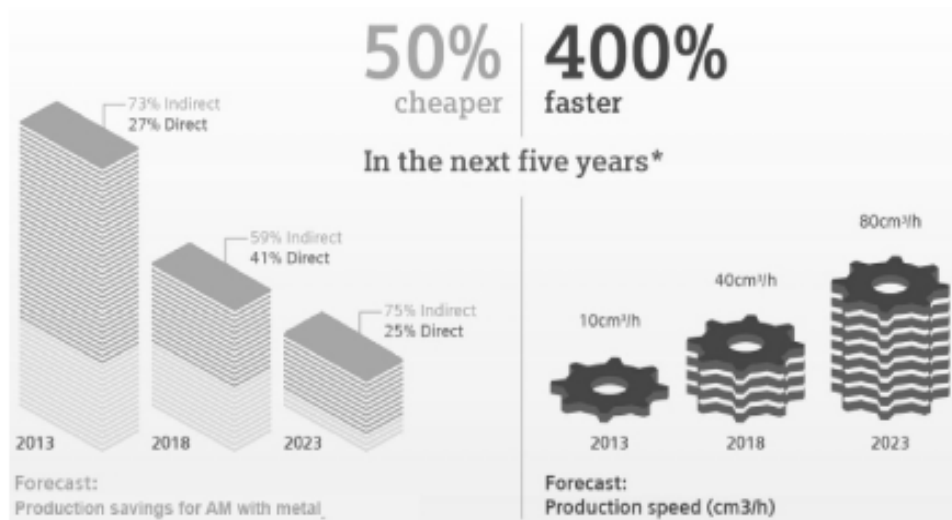


Figure 2.7: Production savings and speed forecast by Siemens (Attaran, 2017)

Advantages (Attaran, 2017), (Thompson *et al.*, 2015), (Singh and Singh, 2017)

- Reduction of time to market
- Reduction of repairing times
- Reduction of investments in tooling
- Mass customisation is possible
- Production of very complex parts at low cost
- Relatively inexpensive production of small lots
- Supply chain simplification
- Improved parts quality
- Manufacturing in remote locations and goods delivery is no longer a restriction
- Elimination of penalties for a redesign (Attaran, 2017)
- Manufacturing decentralisation
- Assembly parts realisable as integral components (Thompson *et al.*, 2015)

- Possibility to quickly change the design
- Products optimisation for function (embedded features such as cooling channels) (Singh and Singh, 2017)

- Damaged components repairing possible with some AM apparatus
- Process flexibility
- Material utilisation close to 90-100%
- On-demand production
- Coupling with a CNC apparatus or a laser cutting system is possible
- Topologic optimisation and software simulations adoptable

Disadvantages (Attaran, 2017)

- Building volume limited by the AM apparatus sizes (PBF, BJ)
- Sometimes it is necessary to produce parts in their fractions hence assembling them successively
- Production often still advantageous only for limited editions in terms of costs
- Material for AM are generally expensive
- Not very large availability of materials employable
- Expensive equipment (Attaran, 2017)
- Sometimes post processing and subtractive operations as well, are required for the allowances control
- Sometimes post-processing heat treatment is preliminary to achieve the functionality and the component reliability desired.
- Weldability issues can occur
- The adoption of an inert atmosphere or keeping a vacuum regime within the chamber is somewhat expensive.

2.5 The Additive Manufacturing “Approach”

Although the great variety of diversified AM apparatus existence, it is possible to recognise the main process chain that unites all of them. However, varied adjunctive design and process variations can be adopted relative to the specific application.

Wanting to better detail the main steps followed by a designer starting from the first digital conceiving of the components to be manufactured up to its realisation, the following chart (Figure 2.8) represents a reliable benchmark. However, it is necessary to premise that the process steps illustrated as follows, are specifically referred to the PBF technology and therefore the flow chart presented has just the intention to provide the main idea on which an AM process could be based.

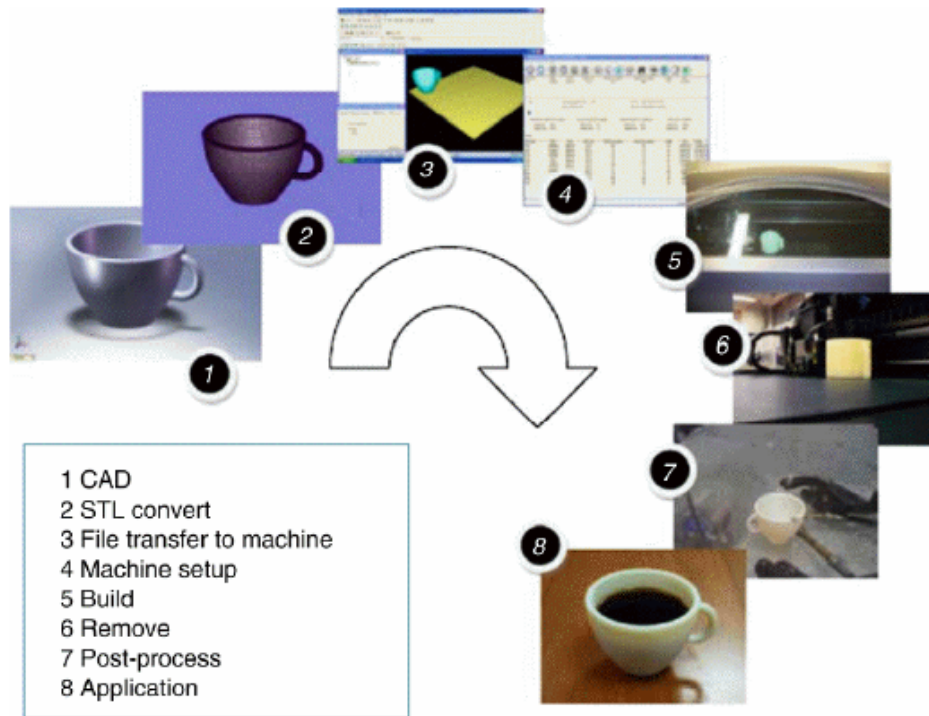


Figure 2.8: Main part design and realisation steps via Additive Manufacturing (I. Gibson, D.W. Rosen, 2010)

(Flowchart description)

1. Design phase:

In general, to realise the 3D CAD file, two main design approaches are pursuable: a “Forward Engineering” or a “Reverse Engineering” (Michael Ashby, Hugh Shercliff, 2009).

In the former case, the component is realised from zero starting from “Blueprints” and technical data left to be read by the designer who, also thanks to his creativity, practically interprets them into a digital 3DCAD model. In this case, it may be possible that does not exist specific knowhow to realise the specific part in question.

On the other hand, a product launched into the market could not fulfil the customer expectation or else it could be not aligned with fundamental requirements such as profit margin and competitiveness on the market. In this instance, a product reverse engineered could represent the best choice to realign its design, exploiting an already existing and specific know-how (Michael Ashby, Hugh Shercliff, 2009).

At this purpose, thanks to appropriate 3D scan software, it is possible to obtain a digital representation of already existing components, which can be modified and implemented by the designer. As an example, the software “*PoliWorks|Modeler*” is capable of extracting CAD data from 3D models, allowing to successively modify their shape and specifics by a conventional 3DCAD tool (innovametric, 2019).

2. .STL conversion

Successively to the digital 3D part design, the 3DCAD file is converted (or exported) into a “.STL” file. In this passage, is performed an object meshing so that it will be further possible interpreting the part geometry and hence the slicing planes. The meshing setup is customizable accordingly the designer accuracy needs.

3. Printing set up

Thanks to appropriate slicers software, is possible to report the 3D part previously designed into a virtual printing chamber. In this step, it is possible to handle essential process parameters such as the number of replicas, their disposition within the machine chamber, their spatial orientation and all matters related to the possible setbacks occurring because of the building process.

4. Machine set up

Concluding the pre-processing phase, are implemented all the process parameters in the virtual machine interface. Depending on the different nature of the A.M. apparatus, some process parameters can vary, although, the major part of them is shared at least in concept.

5. Building process

The A.M. building process is generally wholly automatized. However, the supervision of an operator is anyhow needed to oversee (and eventually stop in case of drawbacks occurring such as re-coater crashing or part collapsing) the process.

6. Part removing

The part(s) removing, and cleaning always requires manual intervention. As an example, in the case of a PBF building process end, the exceeding powder, still sticking in the parts' cavities, is usually sucked by an aspirator to be recycled, and the building plate extracted from the printing chamber by a specialised technician. Furthermore, manual intervention is also fundamental to remove the expendable supports still part of the as-built component at the end of the additive process.

7. Post-processing

Once that the component is cleaned and released by the redundant building supports, the part can be treated with post-processing operations whether required. Not always a 3D part after its removing is ready to use, but somewhat further subtractive CNC operations, as well as heat treatments, can be needed so that the part matches the functionality requirements. Is in this process step that, where appropriate, allowances, surface finishing and part densification are improved.

2.6 Metal AM categories

In the face of all the AM families, one of the most promising is the Metal AM According to the *2019 Whoolers Associates* report, the metallic materials for AM are yearly marking a revenue growth of more than the 40%, so making hope that the metal AM applications are still increasing in the next years (Digital Engineering, 2019). The merge of peerless freedom of manufacturability provided by AM, and the metals thermo-physical properties can provide very

complex parts capable of withstanding in severe conditions of loads and thermal phenomena, endowed of essential functionalities such thermal and electrical conductivity (Ngo *et al.*, 2018). Furthermore, metal AM counts among its advantages the capability to produce unique parts, embedding a large amount of very sophisticated features making so obsolete the need to build several components to be respectively assembled. As a result, pursuing this route is possible to realise parts (as well as assemblies) less expensive, lightweight and with performing physical-mechanical properties (Zhang *et al.*, 2017). Nevertheless, thanks to the remarkable hallmarks just described, this type of technology is nowadays broadly employed in very demanding fields such as aviation, aerospace and automotive, where costs and weight reduction as well as performances optimisation and power density improvement, represent some of the critical factors on which is based the today research. In the overall, the part realisation is performed starting from a feedstock material generally in powder or wire form, then melted (or in some instances sintered) by either a laser or an electron beam source and made solidifying in overlapped layers successively deposited. More precisely, this manufacturing approach is shared by the two main AM Metal categories: The Direct Energy Deposition (DED) and The Powder Bed Fusion (PBF). However, more recent techniques such as Binding Jet (BJ), Cold Spraying (CS), Friction stir Welding, Direct metal writing and diode-based processes exploit different way to consolidate the object (Ngo *et al.*, 2018).

Wanting to clarify better and categorise the different Metal AM technologies, their main classes and most common nomenclature, are reported as follows (Table 1) (Najmon, Raeisi and Tovar, 2019).

Table 1 Metal AM classification (Najmon, Raeisi and Tovar, 2019)

Direct Energy Deposition (DED)	Powder Bed Fusion (PBF)	Others Metal AM processes
<ul style="list-style-type: none"> • Laser Metal Deposition (LMD), Laser Beam Metal Deposition (LBMD) • Laser Engineering Net-shaping (LENS) • Electron Beam Welding (EBW) • Electron Beam Freeform fabrication (EBF) • Wire Arc Additive Manufacturing (WAAM) 	<ul style="list-style-type: none"> • Direct Metal Laser Sintering (DMLS) • Selective Laser Melting (SLM) • Electron Beam Melting (EBM) 	<ul style="list-style-type: none"> • Binding Jet (BJ) • Cold Spraying (CS) • Friction Stir Welding (FSW) • Sheet Lamination (SL*) (Molitch-Hou, 2018) <p><i>(* The nomenclature “SL” is also commonly employed as the acronym of “Stereolithography”)</i></p>

2.6.1 Powder Bed Fusion (PBF)

The Powder Bed Fusion process (PBF), exploits either a laser or an electron beam which is focalised into a powder bad to melt the particles selectively. In the former case, the particles are melted and then jointed via photoabsorption whereas, in the latter instance, the powders melt because of the electrons kinetic energy transfer to the particles. In particular, these are the two principles on which, the Selective Laser Melting (SLM) and the Electron Beam Melting (EBM) processes are based (Zenou and Grainger, 2018).

2.6.1.1 Laser Powder Bed Fusion (LPBF)

The process starts when a precise dose of powder (contained into a powder hopper) is lifted at the level of the build plate by an elevator. Firstly, the heap of powder is spread homogeneously by a re-coater (or roller) forming a thin powder layer hence thick as the “layer thickness”, and secondly a focused laser beam selectively melts the metal powder accordingly a 2D prescribed journey according to the “Hatching Strategy” or “Deposition Pattern”. The first layer formed adheres with the build plate (pre-heated or not) which is generally constituted by the same material of the part building. In the case of the pre-heated plate, its temperature generally is kept at around 80°C to reduce the thermal gradient (and the cooling rate) rising because of the high temperatures generated by the laser source.

The process is then iteratively repeated, in conjunction with the building plate withdrawing at every layer deposition, so forming with a layer by layer approach the 3D component (Figure 2.10). Furthermore, the SLM process is generally run in an inert gas atmosphere (Argon or Nitrogen) in order to prevent the component oxidation and to reduce the explosions risk in case of highly flammable metals employed (Fayazfar *et al.*, 2018).

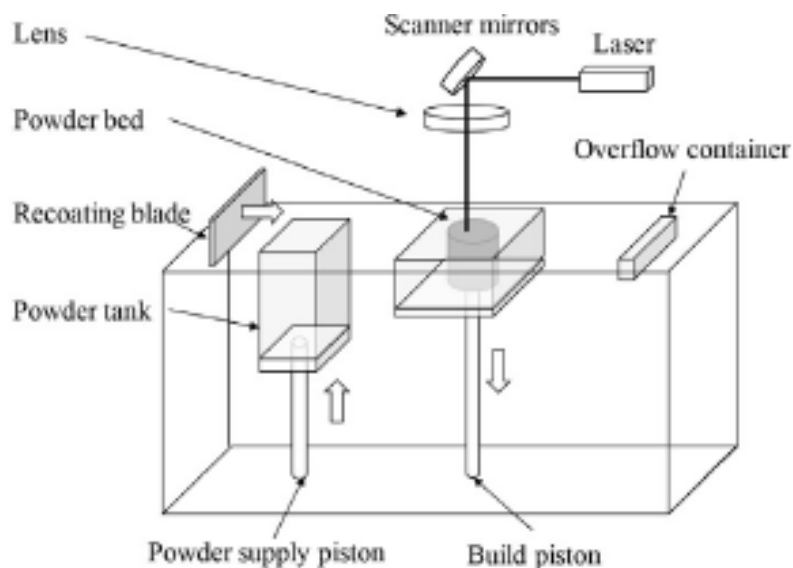


Figure 2.10 Scheme of the Selective Laser Melting (SLM) apparatus (Zhang *et al.*, 2018)

Advantages (Zenou and Grainger, 2018),(Fayazfar *et al.*, 2018)

- High resolution (layer thickness around 20-100 μm) and accuracy
- Tailored material texture
- Complex shapes and cantilever surfaces/features
- A large amount of the powder not melted is reusable
- The process exploits a controlled atmosphere
- Parts different in geometry can be together allocated in the build volume and simultaneously realised.
- Open and customizable parameters (Zenou and Grainger, 2018)
- Lightweight and complex part attainable (Fayazfar *et al.*, 2018).

Disadvantages (Zenou and Grainger, 2018),(Fayazfar *et al.*, 2018)

- High part residual stresses due to the high thermal gradients generated the process
- Relatively slow process in the face of the other AM techniques
- Risky user exposure to carcinogenic metal powders (Zenou and Grainger, 2018).
- Low build rate
- Cavities cleaning is needed to remove the exceeding powder (Fayazfar *et al.*, 2018).

Defectology (Fayazfar *et al.*, 2018),(Debroy *et al.*, 2018)

- Over-melting as well as under-melting cause porosity which can promote cracks initiation (Fayazfar *et al.*, 2018)
- Residual porosity due to gas entrapment
- Lack of fusion due to an inappropriate source energy set resulting in an insufficient molten pool penetration of the underlying layer
- Cracking and delamination due to the different cooling parameters of the new layer deposited and the overlaying material already solidified.
- Residual stresses and thermal distortions affect the as-built parts (Debroy *et al.*, 2018).

2.6.1.2 Electron Beam Melting (EBM)

The approach used by the EBM apparatus to 3D realise the parts is similar to that exploited in the SLM technique, although in this case, the primary energy source focalised on the powder-bed is an electron beam instead of a laser source. Before selectively melting the particles, the electron beam is de-focalised and made scanning the powder bed with a low energy regime to pre-sintering the powder. Furthermore, thanks to this adjunctive step, is so possible minimise the support generation needs conferring a preliminary strength to the pre-consolidated layer times to sustain it during the forming phase (Zenou and Grainger, 2018).

The process is generally run in low pressure or vacuum conditions with only a small amount of helium to avoid undesired beam scattering phenomena (Zenou and Grainger, 2018).

The temperatures involved are sensitively higher than that occurring in the SLM. For instance, during the building process, depending on the type of metal alloy processed, the bed can easily reach temperatures up to 1000°C. These thermal conditions, due to the high electron energy source, lead moreover to a medium-low cooling rate, therefore, to modest residual stresses within the parts.

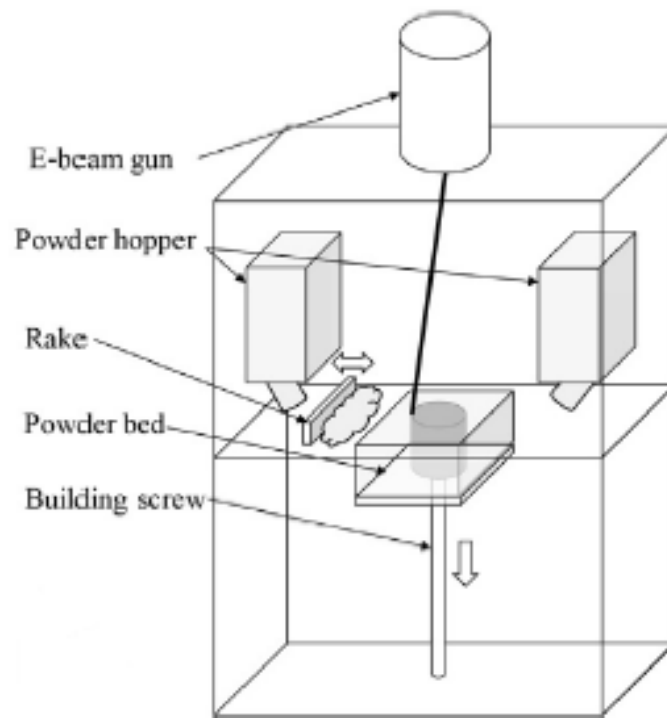


Figure 2.11: Scheme of the Electron Beam Melting (EBM) apparatus (Zhang et al., 2018)

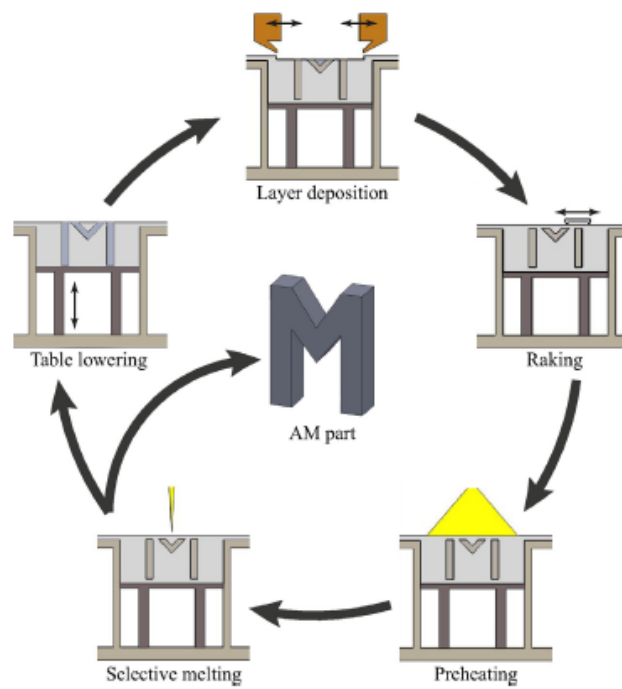


Figure 2.12: Main EBM forming steps (Galati and Iuliano, 2018).

Advantages (Zenou and Grainger, 2018)

- Modest residual stresses due to the high temperatures involved
- Faster than SLM because of thicker layer melted
- Suitable to build relatively large components
- Reduced need of support generation thanks to the pre-sintering phase giving more stability to the overhanging surfaces (Zenou and Grainger, 2018).

Disadvantages (Zenou and Grainger, 2018)

- Only conductive powders are processable
- The necessity to treat residual powder to make it reusable because heat-treated
- Alloying elements evaporation can occur because of too meagre vapour tension (Zenou and Grainger, 2018).

Defectology (Villeneuve *et al.*, 2018)

- Tolerances errors and surface defects:
- Staircase defect due to layer thickness and part orientation
- Not compliant beam positioning
- Error in platform positioning
- Overhang surfaces warping and curling
- Loss of thickness and loss of edge (Villeneuve *et al.*, 2018).

2.6.2 Directed Energy Deposition (DED)

Unlike PBF technologies, the Direct Energy Deposition technique enables to build functional parts, directly on the base plate, melting the material when it is depositing so realising in-situ dense parts thanks to the high cooling rate involved which allows a rapid material solidification (Gibson, Rosen and Stucker, 2014).

More in general, two different subsets of DED technology can be distinguished: the “Blown Powder” DED system (Powder Feeding), and the “Wire” DED system (Wire Feeding). These two, differ for the feedstock material form employed to be melted and welded with the substrate or with the already solidified deposited layers (Gibson, Rosen and Stucker, 2014). For a more detailed classification of the DED processes, the reader is reported to Table 1.

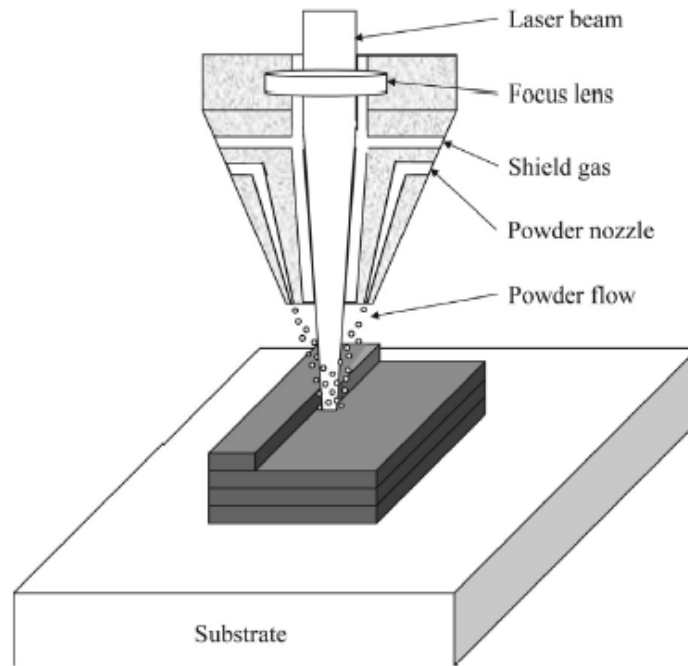


Figure 2.13: Scheme of the Laser Engineered Net-Shaping technique (Zhang *et al.*, 2018)

2.6.2.1 DED-Wire Feeding

The WAAM technique, as a subset of the DED processes, can be furtherly categorised in three main classes distinguished on the type of energy source that they exploit: “Gas Tungsten Arc Welding” (GTAW), “Gas Metal Arc Welding” (GMAW) and “Plasma Arc Welding” (PAW) (Wu *et al.*, 2018).

Similarly to the Blown Powder systems, the deposition by WAAM can occur either in a sealed chamber with a controlled atmosphere or in the atmosphere employing a shielding gas system. Furthermore, keeping the parallelism, in both cases, the deposition tools are driven by robotic arms which guarantee high building freedom. Furthermore, to control the process performances and the process parameters such as the involved temperatures, the bead regularity and the material behaviour, the apparatus is equipped with sophisticated transducers and sensors (Wu *et al.*, 2018).

More specifically, the deposition starts when a laser or an electron beam source melts the wire feedstock to the substrate realising the first layer (or Single Scan Track as well). Therefore, the part is realised for successive layers over positions forming a 3D component. Thanks to the fully dense feedstock material, following an appropriate deposition strategy, the WAAM technique is generally capable of realising not too complex 3D parts, with no porosity imputable to the process and with a material utilisation of about 100%. For this reason, this technique is broadly used to realise structural and functional parts as well as for cladding operations. However, even though the lack of porosity within the part built represents a remarkable advantage in terms of structural performances and part functionality, the dimensional accuracy and the surface finishing result to be very meagre. As a result, post-process subtractive operations are fundamental before implementing the component in its application (Gibson, Rosen and Stucker, 2014).

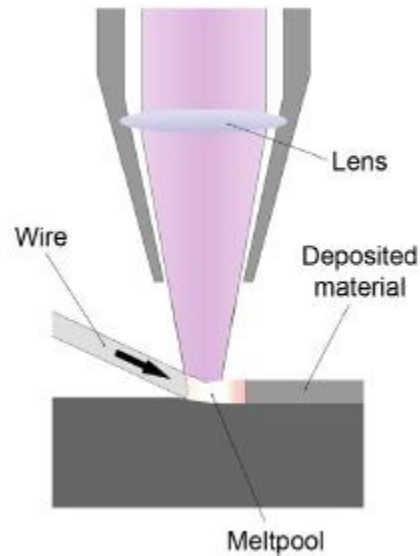


Figure 2.15: General scheme of the Wire Arc Additive Manufacturing (WAAM) technique (Molitch-Hou, 2018)

Advantages (Cunningham *et al.*, 2018), (Gibson, Rosen and Stucker, 2014)

- Material utilisation close to 100%
- Generally, very meagre porosity (also depending on the material type and the process parameters)
- Possibility to build structural components (Gibson, Rosen and Stucker, 2014)
- No powder recovery system required
- Cheaper than Blown Powder DED
- Capability to process a great variety of materials
- Relatively low capital investment for the equipment
- Reduced health risk compared to that promote by powder usage
- High deposition rate 1-10 Kg/h (Cunningham *et al.*, 2018).

Disadvantages (Gibson, Rosen and Stucker, 2014), (Cunningham *et al.*, 2018), (Greer *et al.*, 2019)

- Inadequacy to realise too complicated parts
- Not suitable to implement features with layer thickness transitions
- Dimensional and surface finishing inaccuracy (Gibson, Rosen and Stucker, 2014)
- Large grains' growth undesired for room temperature applications
- Difficulty in monitoring the “inter-pass temperature” to reduce the heat storage within the part
- Difficulties in obtaining fine microstructure (Cunningham *et al.*, 2018)
- Machining always needed to release support structures (Greer *et al.*, 2019)

Defectology (Wu *et al.*, 2018), (Cunningham *et al.*, 2018)

- High residual stresses and cracking whether a poor deposition pattern is implemented
- Thermal deformation due to high heat storage within the part
- High-temperature fatigue
- Severe oxidation fo Ti-alloys
- High residual porosity for Al-alloys
- Low surface finishing and dimensional distortions for Steel (Wu *et al.*, 2018)
- Micro fissures
- High anisotropy
- Surface waviness (Cunningham *et al.*, 2018)

2.6.2.2 DED-Powder Feeding-LBMD

The apparatus typically consists of the main nozzle mounted into a two- or three-axis mechanic arm system, in which is embedded the primary energy source; this latter is either an Nd-YAG or CO₂ laser, or an electron beam. The building plate is tight to a separate mechanic system which makes its motion viable in two- or three-axis and independent to the nozzle's motion. Therefore, the high mobility of the primary mechanic arm and the base plate, allow in the overall to build the part with up to nine freedom degrees (Zenou and Grainger, 2018).

Besides, in order to monitor and optimise the deposition, the system is equipped with an “integrated feedback system” recording and analysing the data of the ongoing deposition process. Through apposite sensors detecting the light in the deposition zone (infrared cameras or pyrometers (Thompson *et al.*, 2015)), the open parameters, such as laser power and scan speed, can be retroactively handled to optimise the deposition (Mazumder, 2017). Furthermore, it is also possible to couple the DED technology with a CNC apparatus, therefore, creating a hybrid system able to perform additive and subtractive operations simultaneously [31].

Thanks to this latter capability, this type of technology allow repairing damaged parts adding material to an already existing part and subtracting the exceeding one in order to control the dimensional allowances and the surface finishing. Is moreover possible, to realise surface coatings employing a multicomponent feedstock.

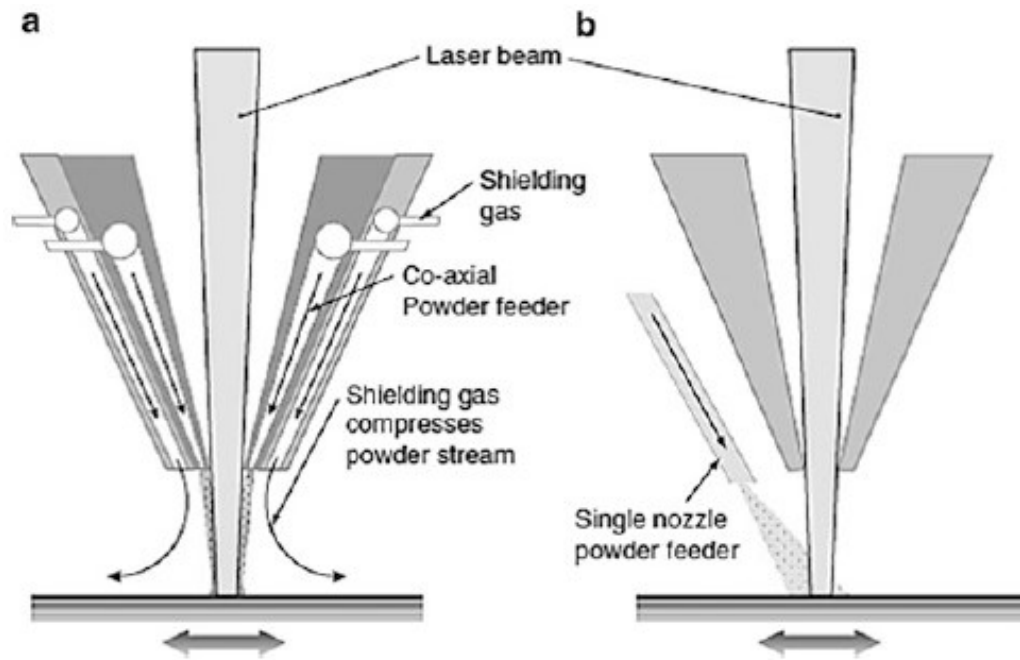


Figure 2.14: Scheme of the Laser Beam Metal Deposition (LBMD) technique - a) coaxial nozzle feeding, b) single nozzle feeding (Gibson, Rosen and Stucker, 2014)

More in detail, the layers deposition is performed by a “deposition head” embedding a feeding system composed by one or multiple channels, fluxing a mixture of metal powder and carrier gas in conjunction with shielding gas. This latter is fundamental to prevent the impurities embedding, as well as the material oxidation, whether the deposition is performed in the atmosphere. The channels just described face to the centre of the tool conveying the blend of powder and gas towards the laser beam focused in the central zone of the head.

When the laser source interacts with the plate, the substrate melts creating a “Melt Pool” in which the fluxing particles become entrapped. Depending on the “open” process parameters set, the particles can be either melted in flight before they reach the Melt Pool or else when they enter within the melt pool itself. Commonly, this later instance is that one typically adopted (Gibson, Rosen and Stucker, 2014).

However, not all the powder fluxed towards the building zone is exploitable by the process since part of it ricochets on the substrate without interacting with the molten material.

2.6.2.2.1 Process parameters - LBMD (Powder Feeding)

Since the LBMD process is at open parameters, it is possible to effectively and accurately manage the same to optimise the deposition, so manufacturing complex parts endowed with particular mechanical, geometrical and functional properties.

As a matter of the fact that the as-built part’s properties are tightly related to the process parameters setting, the “*Transverse Speed*”, “*Laser Power*”, “*Feed Rate*”, “*Powder Stream*” and “*Hatching strategy*” play a fundamental role influencing the cooling rate, the part geometry and the surface finish, besides the mechanical properties hence, the microstructure.

(Transverse speed)

As the process starts, the primary energy source melts the substrate, so creating the Melt Pool, semicircularly shaped in its cross-section, with dimensions in the range of 0,25-1mm in diameter and 0,1-0,5 mm in depth (Gibson, Rosen and Stucker, 2014).

From a physical perspective, as the deposition head is spatially displaced, the dynamic deposition of the material can be interpreted as the Melt Pool's elliptical trailing, moving at a velocity set. Therefore, it appears clear that the transverse speed, or else the deposition head velocity (typically ranging between 1-20 mm/s), directly affect the tracks' profile and width, beside the productivity rate. Nevertheless, selecting the appropriate Transverse speed value, it must also be considered its correlation with the cooling rate, which as already said influences the microstructure (Thompson *et al.*, 2015).

Furthermore, in order to achieve a homogeneous deposition, the Laser Power "P" must be increased together with the deposition speed, to properly melt the amount of flowing particles fluxed in the unit of time. As a result, a severe increase of these two parameters entails to very high-temperature gradients spread out in a heat-treated zone, in conjunction with a very brief time given to the molten material to cool down.

Therefore, the transverse speed directly affects the Melt Pool's cooling rate (generally ranging in $10^3 - 10^5$ °C/s) hence the microstructure's morphology and properties (Gibson, Rosen and Stucker, 2014).

For instance, a high transverse speed leads to high cooling rates promoting a fine and columnar grains' growth, whereas, modest transverse speed values produce low cooling rates responsible for a coarse microstructure (Shamsaei *et al.*, 2015).

(Laser Power)

Aside from the transverse speed, the cooling rate is also affected by the molten metal superheating as a consequence of the Laser Power level employed (generally it varies in the range of 100 – 5000 W (Thompson *et al.*, 2015)). Inversely to the Transverse speed, a high Laser Power level promotes a coarse microstructure whereas modest laser energy leads to fine and columnar microstructures. However, to undertake an accurate analysis of the deposition performances, the nominal P-value it is not sufficient to accurately define the fusion results. It is indeed necessary to consider the real energy absorbed by the material, not taking into account the radiation reflected by the substrate or by the deposited material as well (Shamsaei *et al.*, 2015). A deepening on this point is provided in section 2.6.2.2.1 when dealt with the "Specific Energy".

(Flow rate)

Definable as the mass of powder fluxed by the nozzle(s) in the unit of time, the powder feed rate (g/min), directly influences the deposition homogeneity and compliance (Mahamood and Akinlabi, 2018).

Since its conception, when the laser cladding technologies have been introduced, it represents one of the most challenging parameters to be handled because of the difficulty to make this parameter predictable. Although the major part of studies and applications consider the feed rate as a constant variable, according to Lie Tang *et al.* a better strategy to achieve a uniform and homogeneous deposition, is to consider the flow rate as a dynamic parameter. According to that, it is indeed possible to take into account the deposition head accelerations and deceleration occurring during the deposition process, thanks to a control

system termed “*Variable powder flow rate control*” (VPRC) based on optoelectronic sensors (Tang *et al.*, 2008). In particular, high flow rate (generally ranging between 1 – 10 g/min) values result in an increased melt pool density due to the significant amount of particle mass fluxed in the same unit of time besides providing an enhanced layer thickness. However, the flow rate effectively influences the deposition accordingly to what just stated only at relatively low Laser Power levels, whereas, for high energy values employed, its effect is meagerly recordable (Thompson *et al.*, 2015),(Shamsaei *et al.*, 2015).

Furthermore, it results important also to optimise the relationship existing between flow rate and transverse speed, for instance, running custom software analysis before the deposition process in order to avoid feeding breaks or else drawbacks.

(Laser beam and powder stream)

Together with the influence of the singles exposure parameters, it must be considered their dynamic coupling. In fact, since the powder stream and the laser beam coupling can be not considered as fixed, the nominal values do not represent unique data to optimise the deposition. Nevertheless, different head deposition orientations affect the powder stream percentage effectively interacting with the laser beam and then with the dynamic Melt Pool. Different Laser Beam - Powder Stream coupling configurations can indeed arise during the process depending on the 3D path that the deposition head follows to realise the component and on the equipment settings(Figure 2.15). For instance, if the deposition head is inclined to the horizontal, the powder stream can be subjected to the gravity effect and easily be deflected downwards decoupling in part from the area of laser interaction. Therefore, as a consequence of an optimised interaction or not between laser source and powder stream direction, different layers’ height and boundary conditions are achieved at the deposition end (Shamsaei *et al.*, 2015).

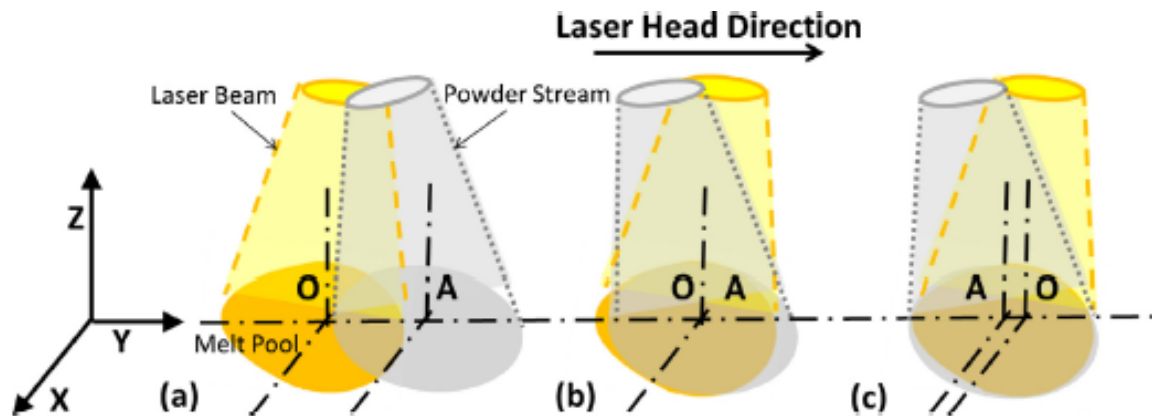


Figure 2.15: laser beam and powder stream dynamic configurations.

(Hatching Strategy)

With “*Hatching Strategy*” it is intended the repetitive pattern followed by the nozzle when depositing the material in a 2D area. How the layers are successively deposited and overlapped, largely influences the residual stresses, the thermal distortions, the eventual part deflection and the porosity morphology and percentage within the final part. According to that, the Hatching

strategy must be designed with the intent to minimise and avoid these drawbacks as more as possible (Shamsaei *et al.*, 2015).

Although a great variety of them exists seeing its “open” nature, the scan patterns to choose from and broadly employed are commonly four: “Raster”, “Bi-directional”, “Off-set” and “Fractal”. The scan pattern often preferred among these, thanks to its easiness to be implemented and its high adaptability to be employed independently from the part’s shape, is the Raster pattern. However, the “Off-set” and the “Fractal” patterns, even though generally less exploited, ensure an enhanced geometrical accuracy in conjunction with an energy consumption saving. Furthermore, these latter have been found to provide the lower substrate deformations after the part’s cooling (Shamsaei *et al.*, 2015).

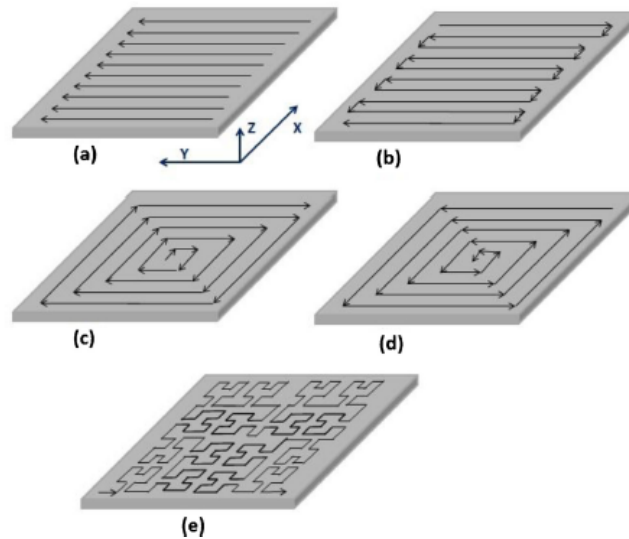


Figure 2.16: Different scanning strategies: a) Raster, b) Bi-directional, c) Off-set out, d) Off-set in, e) Fractal (Shamsaei *et al.*, 2015)

2.6.2.2.2 Parameters correlation

According to what just reported in the description of the specific parameters, it is fundamental to notice how they are interrelated one to each other. Therefore, to pursue an optimal and homogeneous deposition, it results necessary to rationalise the mutual influences of Laser Power, Feed Rate and Transverse speed in combined parameters. The two here deemed as essential and as the starting point on which base a deposition optimisation are: the “Specific Energy” and the “Powder Feed Density” (Shim *et al.*, 2016).

(Specific Energy)

Wanting to determine the optimal process parameters value, so that is possible to ensure a proper material melting beside a prediction of the layer height/width ratio, it has to be considered the “Specific Energy E ” (J/mm^2). This latter, correlates the Laser Power P (W), the laser spot diameter d (mm) and the transverse speed v (mm/s) as reported just below in the Equation (2.1)

$$E = \frac{P}{dv} \tag{2.1}$$

This parameter defines the optimal energy value, thresholding in its lower limit, a lack of fusion and in its upper limit a too high dissolution (Shim *et al.*, 2016).

(Powder feed density)

Otherwise, the powder feed density correlates the Feed/Flow Rate with the laser spot diameter and the transverse speed, instead of the laser power. The Powder feed density F (g/mm^2) is defined as follows in Equation (2.2) where G is the Powder Flow Rate (g/min), d the laser spot diameter (mm) and v the Transverse speed (mm/min) (Shim *et al.*, 2016).

$$F = \frac{G}{dv} \quad (2.2)$$

(Layer thickness calculation)

As already mentioned, it is possible to highlight a direct correlation respectively between the laser power and the feed rate with the layer thickness. As a consequence, it can also be noticed the direct relationship with the layer thickness and the Specific Energy and the Powder feed density as well. Therefore, is finally possible correlate all the exposure parameters previously analyzed with the layer thickness “ t ” (mm) as parameter representative of the crucial and primary feature of an optimal deposition, thanks to the implementation of the two combined parameters “ E ” and “ F ” respectively in the two experimental equations (2.3) and (2.4) (Shim *et al.*, 2016).

$$t = 12.64 + 2.55E \quad (2.3)$$

$$t = 22.85 + 2.75F \quad (2.4)$$

(Deposition optimisation Map)

To complete the framework of the process parameters correlation, is here just below drafted a typical process map considering the Laser Power and the Scan velocity as reference parameters. These maps intend to display a safety region in which run the deposition to avoid the defectology occurring.

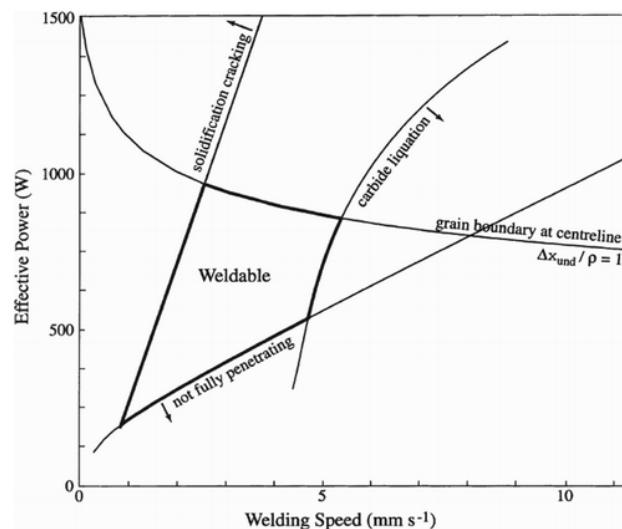


Figure 2.17: Deposition optimisation map for a DED process, safety window and main defectology categories (Sames *et al.*, 2016).

Advantages (Molitch-Hou, 2018), (Zenou and Grainger, 2018), (Zhong *et al.*, 2019), (Gibson, Rosen and Stucker, 2014)

- Possibility to repair damaged components
- Very high productive rate compared to that of PBF
- It is possible to dispose of hybrid DED – CNC apparatus (Zenou and Grainger, 2018).
- Employable for surface modification and laser cladding
- Very fine microstructure due to the high cooling rate (Zhong *et al.*, 2019)
- Possibility to build very large components
- The deposition is performable with multiple degrees of freedom, thanks to the multi-axis motion of the deposition head as well as of the build plate (Molitch-Hou, 2018).
- Capability to deposit multi-component materials (in-situ composites)
- Microstructural control thanks to the mixture and cooling rate handleability
- Solidification direction control and monocrystal manufacturability (Gibson, Rosen and Stucker, 2014)

Disadvantages (Najmon, Raeisi and Tovar, 2019), (Zenou and Grainger, 2018), (Zhong *et al.*, 2019), (Gibson, Rosen and Stucker, 2014)

- High residual stresses in the as-built part
- Whether the apparatus includes a sealable chamber, a large amount of inert gas (Nitrogen or Argon) is required in conjunction with an appropriate lead time to reach the oxygen level desired.
- Poor resolution and surface finish
- Accuracy not better than 0.25mm and surface finish at least of 25 μm
- Supports removal needed (Gibson, Rosen and Stucker, 2014)
- Anisotropy especially employing the WAAM technology (Najmon, Raeisi and Tovar, 2019)
- Are often required further finishing operations such as machining, in order to control the dimensional allowances and the surfaces features (Zenou and Grainger, 2018).
- Generally limited deposition rate in the range of 0.5 Kg/h (Zhong *et al.*, 2019)

Defectology (Gibson, Rosen and Stucker, 2014), (Thompson *et al.*, 2015)

- Cooling rate changing can occur especially in thin-walled structures
- Cracking due to residual thermal stresses
- Cracking and delamination occurring as a consequence of repeated thermal cycles
- Porosity and balling effect in case of not optimised process parameters (Gibson, Rosen and Stucker, 2014).
- Porosity due to gas entrapment
- Irregular deposition due to powder stream not correctly aligned
- Lack of fusion in case of not optimised process parameters (Thompson *et al.*, 2015).

2.6.3 DED and PBF comparison

The two primary metal A.M. categories are compared in their main hallmarks as follows, taking into considerations their three main LMD, SLM and EBM subcategories.

Table 2: General differences of process parameters and equipment capabilities between LMD, SLM and EBM (Zenou and Grainger, 2018),(Thompson et al., 2015),(Gibson, Rosen and Stucker, 2014) (Zhong et al., 2019).

LMD	SLM	EBM
<ul style="list-style-type: none"> • Nd-YAG or CO2 laser (100 – 5000W) • Ar/He shielding gas • Powder preheating not necessary • Base plate preheating • No build size limitations • Melt Pool size width 0,25-1mm • Layer thickness 100-200µm • Surface finish > 25µm • Geometric tolerance ± 25 mm • Building rate ~ 0,5Kg/h • Repairing • Generally lower mechanical properties than SLM and EBM (coarser microstructure) 	<ul style="list-style-type: none"> • One or more fibre laser (200-1000W) • Ar/N2 atmosphere • Powder preheating at 100-200° C • Base plate preheating • Build size limited by the chamber volume (ex. 500x350x300 mm3) • Melt Pool size width 0,1-0,5 • Layer thickness 20-100µm • Surface finish 4-11 µm • Geometric tolerance ± 005-0,1 mm • Building rate ~ 20/35 cm3/h • No repairing 	<ul style="list-style-type: none"> • High power electron beam source (up to 3000W) • Vacuum/He atmosphere • Powder pre-sintering at 700-900° C • Base plate preheating • Build size limited by the chamber volume • Melt Pool size width 0,2-1,2 • Layer thickness 50-200µm • Surface finish 25-35 µm • Geometric tolerance ± 0,2 mm • Building rate ~ 80 cm3/h • No repairing

2.7 Metal AM Applications

Although the Additive Manufacturing has been mainly thought as a Rapid Prototyping technique so far, a clear trend to turn this technology into a convenient and sustainable manufacturing process is nowadays evident.

In the face of all the markets branches, the Aerospace/Aviation, the Automotive and the Bio-medical fields, are indeed the main sectors driving the AM advancement in conjunction with specialised companies and the academia.

(Aerospace/Aviation)

Dealing with the Aviation and the Aerospace field, the AM finds a role in manufacturing functional and structural components, for rapid tooling and rapid prototyping, and for repairing operations as well.

The AM success in this field is imputable to its remarkable flexibility and its capability to break down several constraints affecting the traditional manufacturing processes. Furthermore, complementarity between the aerospace components requirements and the AM distinguishable features can be recognised. To clarify this perspective, a parallelism between the aviation components needs and the AM hallmarks acts to satisfy them is reported in Table 3 (Liu *et al.*, 2016).

(Automotive)

Likewise, in the Automotive field, the costs and weight reduction, represent the most modern binding challenge that all automotive companies are facing.

At this purpose, these are applying and extending the number of AM applications seeing the 3D printing capability to manufacture sophisticated, light-weight and functional parts (Singh and Singh, 2017).

Relatively to short production runs, is in this way possible cut off costs and lead times. Also, the freeform fabrication techniques allow a without precedents parts customisation; this latter feature critical to differentiate the product in a full field, where the competition is fierce.

(Bio-Medical)

The main AM distinguishable feature of which the Bio-Medical sector benefits, is the capability to conceive and realise tailored components. Is indeed possible, to realise prosthesis as well as scaffolds, in multi-material and with variegated textures in the same object. Nevertheless, the studies concerning the possibility to employ metallic materials appointed to be used in the Bio-Medical sector, have led to outstanding results. Nowadays it is not unexpected realise 3D parts in a great variety of metals and alloys such as titanium alloys (such as Ti-6Al-4V), Co-Cr alloys, Inconel, stainless steels, aluminium, hard and amorphous metals, copper, niobium and beryllium (Singh and Singh, 2017).

Table 3: Aerospace components requirements vs Additive Manufacturing contextual hallmarks

Avio - Aero requirements	AM contextual hallmarks
Complex geometries and high envelope to volume ratio (Liu <i>et al.</i> , 2016)	Freeform fabrication capability (Liu <i>et al.</i> , 2016)
Difficult machinability & buy-to-fly ratio (Liu <i>et al.</i> , 2016)	Capability to process advanced and hard materials such as Ni-, Ti-, special steel- alloys with very high material utilisation (Liu <i>et al.</i> , 2016)
Small production runs (Liu <i>et al.</i> , 2016)	No tools need resulting in cost-saving and high process competitiveness for small quantitative (Liu <i>et al.</i> , 2016)
Quick turnaround parts (Liu <i>et al.</i> , 2016) and lead time reduction	Fast on-demand production
High strength-to-weight ratio, resistance at high temperatures, fatigue loads and aggressive environments (Liu <i>et al.</i> , 2016)	High parts customisation (Liu <i>et al.</i> , 2016) and parts topologically optimizable to reduce weight Generally improved mechanical and microstructural properties respect to wrought components
Real-time cooperation with the decentralised manufacturing plant	Remote manufacturing capability

2.7.1 DED Aerospace/Aviation Applications

The DED system can process varied types of metallic materials of Aerospace/Aviation interest, such as titanium, Inconel, stainless steel, aluminium and their alloys. Furthermore, it is also possible to produce functional components or coatings as well, with graded materials, charging different powder types in the separate hoppers; hence, fluxing them by different nozzles. Furthermore, since the DED apparatus can be coupled with a CNC unit in a hybrid machine, it is possible to realise parts in multiple exploiting different axis of work, performing additive and

subtractive operations as well. Thanks to this versatility, hollow and complex parts embedding functional features, such as channels times to create a cooling system or thin wall structures as well, can be built without supports generation. The CNC unit can be moreover used to control the surface finish and the dimensional allowances spending an overall process time, ten times lower than that required from a PBF process with subsequent finishing operations. Finally, only the DED technology can overhaul damaged components otherwise from PBF and all the other metal AMTs (Liu *et al.*, 2016).

(DED Applications examples)

Wanting to report some applicative examples, a thin-walled helicopter engine combustion chamber (300 x 90mm) built of IN718 by LMD, is indicated in Figure 18. More specifically, the component has been realised with a 0.9 Kg/h deposition rate achieving a 99.5% of density throughout the part in remarkably short time-lapse of around 7.5 hours rather than in months. Furthermore, two Ti-6Al-4V airfoils embedding cooling channels (Figure 2.19) have been successfully realised by LMD at the International Institute of the National Research of Council in Canada (Liu *et al.*, 2016).

Finally, the main repairing steps of a turbine housing realisation employing a hybrid system has been reported as follows (Figure 2.20). As the sequence of the shots depicts, is possible to 3D print the component and then milling its surface to achieve the desired roughness value besides performing precision subtractive operations to control the dimensional allowances and to introduce new features. Noteworthy, are also the large component dimensions (180x150 mm) and the total realisation time of around 5 hours to obtain the finished part (Liu *et al.*, 2016).

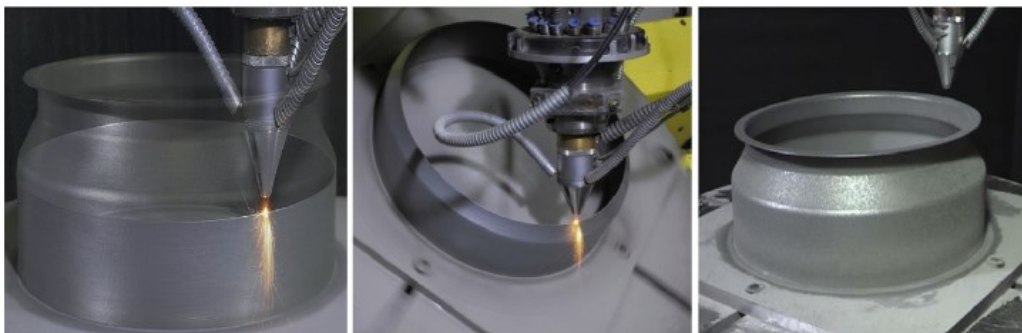


Figure 2.18: Helicopter engine combustion chamber built by LMD (Liu *et al.*, 2016)

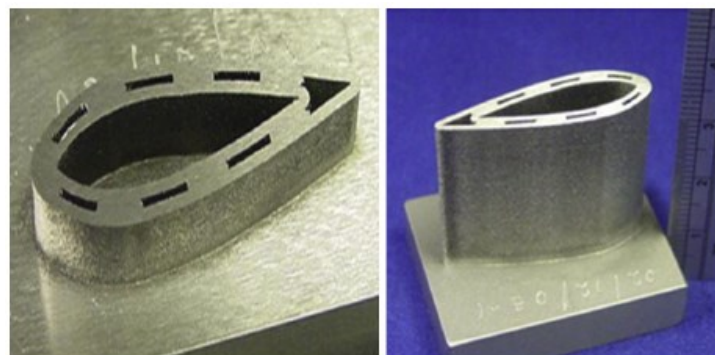


Figure 2.19: Ti-6Al-4V airfoils built by LMD (Liu *et al.*, 2016)

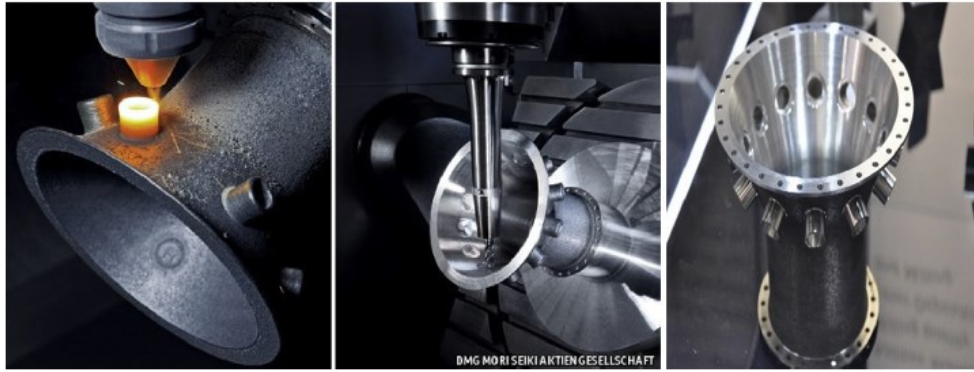


Figure 2.20: Turbine housing building employing a hybrid Additive - Subtractive apparatus (Liu et al., 2016)

2.7.2 Design philosophies and Repairing

As for most of the technological fields, the advancement of the air/space-craft structural safety has been pursued and Implemented throughout the years, thanks to a trial and error learning approach. Unfortunately, some remarkable improvements in this ambit have been promoted by air incidents that have led the engineers to understand the causes and to adopt the appropriate countermeasures (Alderliesten, 2018).

“Safe life”

The first and more ancient perhaps design philosophy adopted by the aircraft designers is the *“Safe-life”*. According to this approach, it was assumed that a structure maintains its integrity throughout its life independently from the environmental conditions, fatigue phenomena, accidental bumps and all related matters. Therefore, designing accordingly such philosophy meant to run a load analysis and over-dimensioning the components, only considering an appropriate “safety factor” (enlarging the part life), (Figure 2.21) fixing a retiring point in which the aircraft was decommissioned to be restored. However, this approach did not guarantee a costs optimisation and a lowering in the buy to fly ratio. Therefore, as the service life was increased aiming to reduce flights cost, the risk of failures dramatically increased because of not considering the deleterious effects of the fatigue and corrosion phenomena besides the presence of defects within the components (every time present after their manufacturing) potential cracks sites and initiators. (Alderliesten, 2018)

“Life-Safe”

As a consequence of repeated aircraft incidents, new design philosophy was developed. Wanting to increase the safety of the structure, was adopted the principle for which the primary structural components were made redundant so that possible damage or excessive load could be redistributed in the other counterparts. Therefore, a range of tolerance in terms of operational time in which the aircraft could continue to fly was introduced. Otherwise, from the *Safe-life* design philosophy, the new *“Life-safe”* concept, considered to keep in flight the plane before its restore even when partial damage or failure occurred (Alderliesten, 2018).

However, also this second design philosophy presented applicative constraints. Even though the loads' repartition provided advantages in the overall, it was not taken into account the Multiple Site Damage (MSD) occurring. This eventuality occurred indeed

when the first “homologue” feature failed; hence, the whole load amount was divided among the other ones. When the features did not sustain the load left, the fatal component failure, speedily occurred (Alderliesten, 2018).

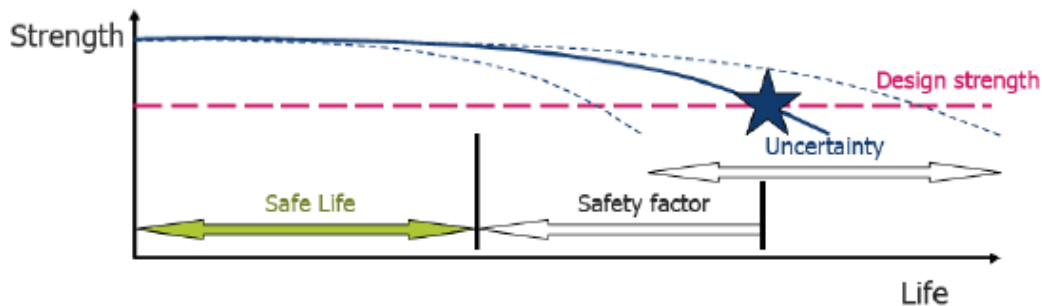


Figure 2.21: Safe-Life design philosophy (Alderliesten, 2018)

“Damage Tolerance”

As a response to the Safe-life and Fail-Safe philosophy lacks, was introduced a new design concept considering the strength of both of them so representing a trade-off between the same.

Since 1978, the FAR/JAR adopted the “Damage Tolerance” as design philosophy (Figure 2.22). This latter takes into account that, the manufactured components, owned unavoidable impurities and defects as a result of the process-induced chemical-physical phenomena. Also, it considers at the same time the operational, environmental and incidental conditions in which the parts have to withstand when in operation, so expecting the occurring of failure. With this perspective, a program scheduling the maintenance and repairing operations to restore the damaged parts was adopted (Alderliesten, 2018).

More specifically, a component is designed “damage tolerant” whether it is capable of sustain loads in conjunction with fatigue, accidental bumps/damages, corrosion and all related matters, before a scheduled inspection and eventually a repairing operation. In the case of damaged overhauled parts, repairing operations are run recovering the initial component strength and extending their operational life (Alderliesten, 2018).

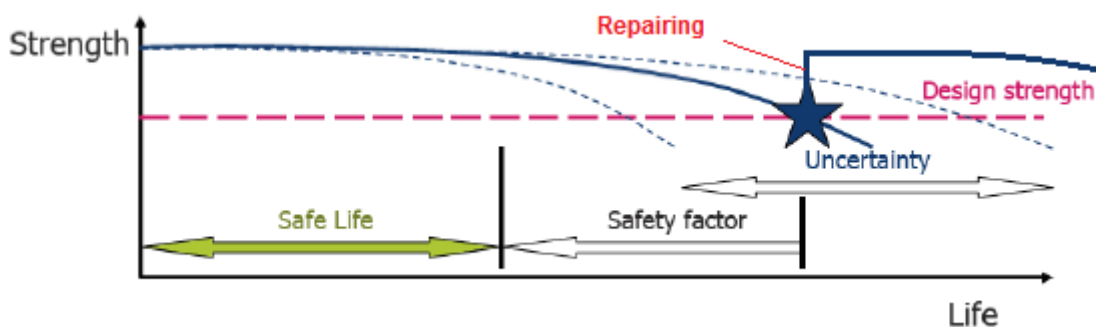


Figure 2.22: Damage Tolerance design philosophy (Alderliesten, 2018), Dark blue line: addition of a Repairing scenario.

According to the importance of restore wore and damaged parts, in the next paragraph will be described what the Additive Manufacturing role in this framework is, how it proposes itself as an excellent alternative to the conventional repairing processes and what are the main operational steps to be followed. Some applicative examples will also be provided to the reader.

2.7.3 Hybrid Additive and Subtractive Manufacturing systems for repair

As widely known, one of the primary AM constraints is represented by the expensiveness of the components built. The economic advantages achievable replacing traditional manufacturing with AM, are mainly limited to some specific applications. More in general, the AM represents an optimal trade-off between costs and complexity of parts built, when short runs or limited editions as well, are required.

Another preliminary requirement for which AM could be deemed as suitable to be employed is the need to create parts for very demanding fields where mechanical properties, part durability and accuracy are essentials. According to this scenario, is, therefore, reasonable to think that this type of processes is overlying to frontiers very hard to be overcome.

However, is nowadays possible to perform parts repairing by Hybrid LMD-CNC apparatus extending the components life conceiving a productive chain that considers building new functional components by DED, as well as by PBF, and repair them with hybrid DED-CNC equipment when damaged. Thereby, with this conception of 3D manufacturing-repair chain, is hence possible to repair very costly damaged components instead of replacing them, so sensitively reducing costs and lead time (Liu *et al.*, 2016). Furthermore, according to some studies run “3D repairing” would also lead to lowered emissions and modest environmental impact (Najmon, Raeisi and Tovar, 2019).

Otherwise from others repairing conventional processes, such as tungsten inert gas welding, plasma transferred arc welding, electron beam and plasma spraying, these DED based Hybrid machines allow to induce less component distortion and more deposition control with unique simpler equipment. (Liu *et al.*, 2016). More in detail, the best advantages in terms of deposition precision and material flexibility are recognisable to the DED Blown Powder technologies which overpass the Wire feeding DEDTs for what concerns the repairing operations and the implementation of new features in already existing parts (Gasman, 2019). Besides, the resulting Heat Affected Zone induced by a DED process such as LMD is remarkably lower compared to that generated in the others processes aforementioned due to the low energy input heat provided by the AMTs (Liu *et al.*, 2016).

Repairing Process:

According to R.Liu *et al.*, three different steps of the repairing process are distinguishable (Figure 2.23). Firstly, a “Repair preparation stage” is run in order to analyse and define the damage morphology and entity. Therefore, since it is possible to interpret the defect as a digital file finally, the damage is measured by either contact tools (feelers or touch-trigger probes) or by non-contact instruments (camera, laser sensors). As a consequence, the defect “negative” area is extrapolated comparing the data acquired to the first component area included in its 3D file. In this step, some evaluations on the repairing process feasibility in order to prevent nozzle collisions, blind areas and so on, are moreover made. Secondly, the material deposition by AM and the subtractive operations to control the dimensional and geometric allowances, are performed. Finally, in the third step is taken into account an analysis of the allowances and compliance, besides, perform microstructural characterisations and fatigue tests (Liu *et al.*, 2016).

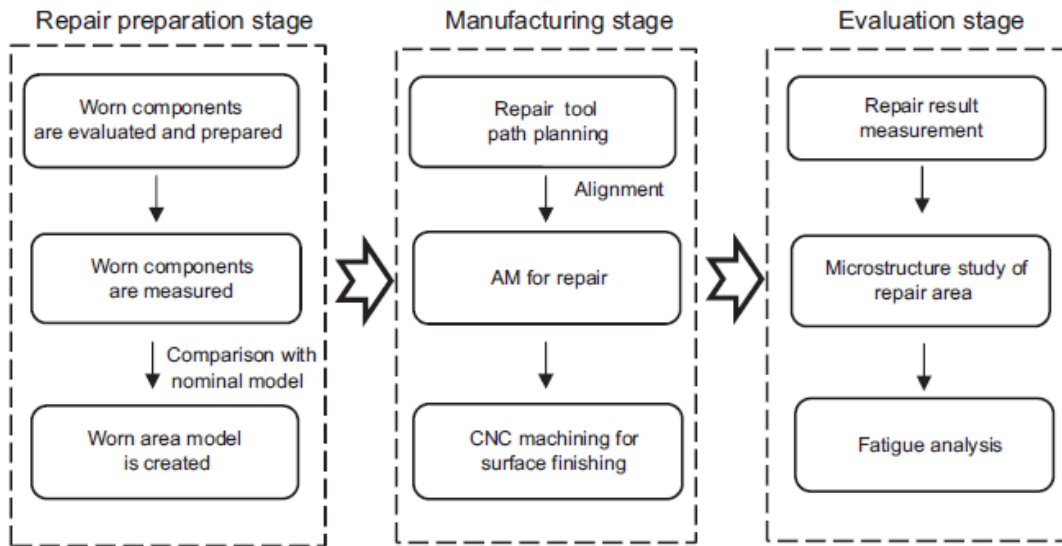


Figure 2.23: AM-CNC Hybrid repairing process main steps (Liu et al., 2016).

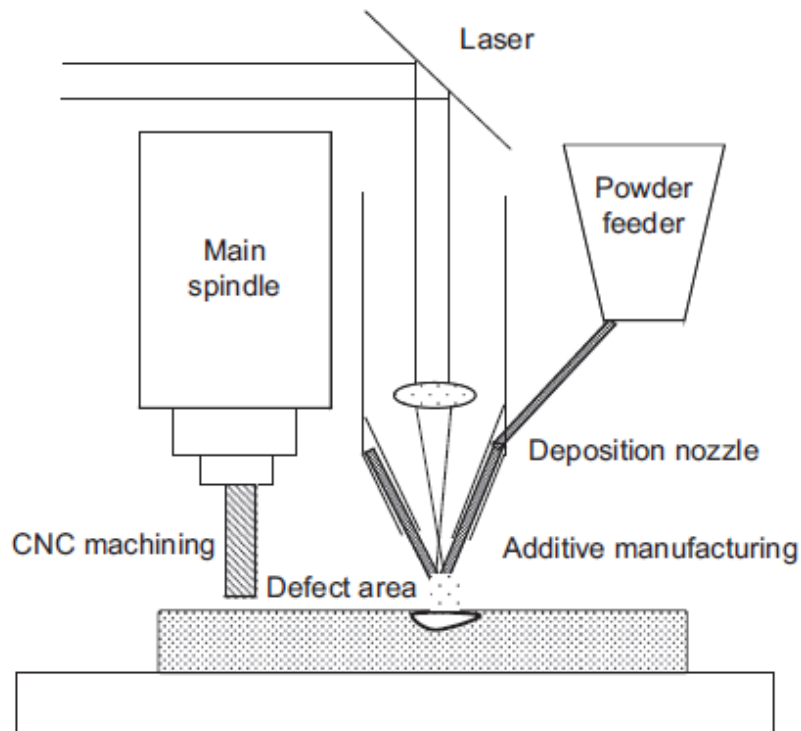


Figure 2.24: Hybrid AM-CNC apparatus (Liu et al., 2016).

(Case studies)

Referring to paragraph 2.7.2 is preliminary to say that not all the aerospace or aviation components as well, are designed a damage tolerance philosophy accordingly. Parts not subjected to critical environmental conditions, repetitive loads or not exposed to incidents can be easily designed following either a safe-life or a fail-safe approach. The same design strategy is adopted for components not easily attainable from the maintenance operators; therefore in these instances, an appropriate safety factor and controlled primary and secondary manufacturing operations are essentials.

However, in this paragraph are presented some representative examples of aviation components underlying to a damage tolerant design due to their operational functions and conditions.

A climax example for which the technology just described could be suitable for, is the turbine blades repairing. Metaphorically, we could also extend this application to turbine rotors repairing which embed a single blades row, otherwise termed “blisks”. As a turbine blade is damaged, it releases debris that affects the other blades and the whole component integrity. An example of blades leading edge repairing by LENS of a compromised Ti64 blisk, is depicted in Figure 2.25 (Liu *et al.*, 2016).

Another example of Avio component restore is reported according to the study run by Xue and Islam work, in which it has been possible to repair an IN738 turbine blade presenting a relevant lacking portion of its tip by LMD (Figure 2.26) (L. Xue, 2006).



Figure 2.25: T700 blisk repaired by Optomec LENS (deposition) and by CNC (finishing) (Liu et al., 2016).

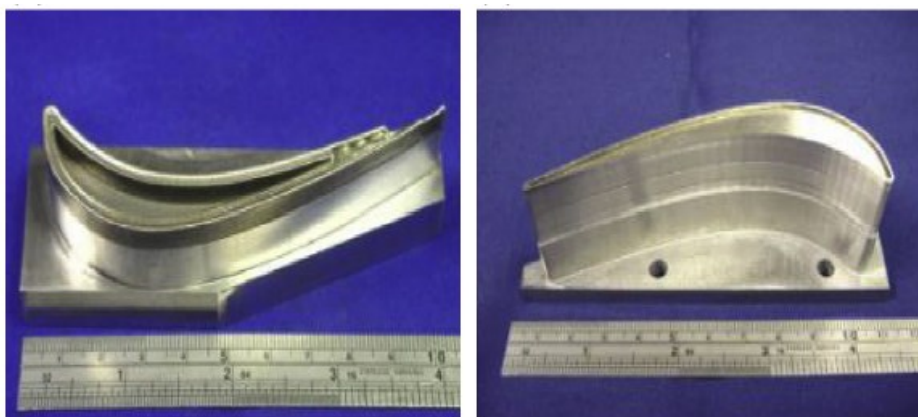


Figure 2.26: IN738 Turbine blade repaired by LMD (L. Xue, 2006).

2.8 Ni Superalloys and AM

Commonly, the Ni-“Superalloys” are defined as a subset of the metallic alloys, that according to a general classification provided by Kevin Minet *et al.*, can be formulated as Iron-Nickel based or Cobalt-based or Nickel-based (Minet *et al.*, 2019).

Their first introduction to the market dates to the '40s during World War II, where this new class of advanced materials were employed to manufacture jet engines as well as military gas turbine components. Successively, in the '50s – '60s the superalloys development and usage in fields such as high-temperature helium reactors, heat exchangers, furnaces, sour gas implants and obviously in aero engines and gas turbines, soared. Otherwise, the superalloys manufacturing processes improvement caught on lately in the 70s–80s. As a result, the new manufacturing techniques, led to the new possibility of the alloys chemical design, besides several productive advantages. For instance, thanks to the introduction of new processes to manufacture single-crystal components, the employment of Mo, W and Ta to promote carbides formation resulted obsolete. Their presence times to strengthen the material acting as pinning particles for the dislocations at the grain boundaries was in this instance inutile (Sims, 1984). Although new manufacturing processes allowed to influence the Superalloys chemical composition, their microstructure is still very complex and characterised by varied elements and phases. Nevertheless, this complexity of phases and microstructures is what makes these types of materials so outstanding.

More precisely, the most significant Superalloys' hallmarks that in the overall made them so precious and suitable to fulfil the design needs of very demanding sectors, as the Aviation and Aerospace are, can be listed as (Minet *et al.*, 2019):

- their capability to withstand under very high temperature keeping their mechanical resistance untouched up to around 80% of their melting temperature
- their enhanced oxidation and corrosion resistance (Minet *et al.*, 2019).

Wanting to address better the main issues related to the synergy intercurrent between material and process, it must be considered that even though the “new” casting processes introduced around the '80s brought essential advantages, the today market needs present in some instances obstacles hardly surmountable by them. Conversely, the metal AMTs are nowadays the driving force pushing forward the manufacturing, when highly performant, tailored and sophisticated components are demanded. About the materials availability, even though initially the Ni-Superalloys have been formulated accordingly casting needs, it is nowadays possible to dispose of a significant variety of superalloys for AM to produce and repair complex components such as turbine blades in IN738 or MAR-M247 by A.M (Minet *et al.*, 2019).

Furthermore, as the Ni-Superalloys born and developed relatively to the gas/Jet turbines, Figure 2.27 shows the various components for which these advanced materials can be used.

However, before describing how the metal AM comes into play processing the Ni-Superalloy and with what results, is reported in the paragraphs as follow a summary of the main phases and microstructural elements characterising a Ni-based superalloy.

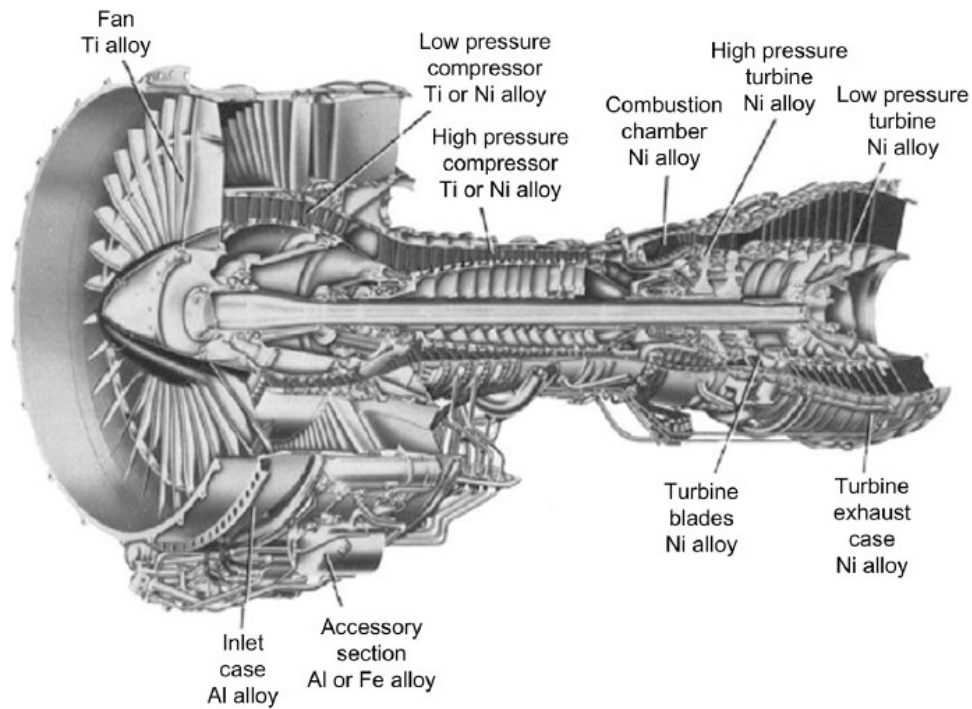


Figure 2.27: Jet Turbine engine section depicting some fundamental components and indexing the materials with which they are manufactured (Minet *et al.*, 2019)

2.8.1 Microstructure description and Phases

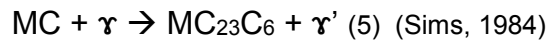
Although, the superalloys chemical composition is variegated and complicated because of the large number of chemical elements present, it can be said that all Superalloys Ni-based share a primary Face Cubic Centered (FCC) γ phase. Otherwise, the Iron and Cobalt-based Superalloys commonly owns a body-centred Cubic (BCC) lattice at room temperature. However, also, this latter can preserve an Austenitic FCC phase in the case of Ni- is present within the alloy's chemical composition (Minet *et al.*, 2019).

Starting from the first thirty years of the 20th century, several studies have been run on the Superalloys' microstructure in order to optimise and better understand their chemical composition.

In the years 1929-1930, adding aluminium and titanium the new "age hardening", the cubical and coherent phase γ' $\text{Ni}_3(\text{Al}, \text{Ti})$ was discovered (Figure 2.28). Thus, firstly introduced in the "Nimonic 80", in the "Tinidur" and in the "A-286" Ni-based Superalloys, presented an FCC austenitic structure providing a strengthening effect when in coexistence with the γ matrix. However, it was early discovered that the strengthening effect could be achieved only whether the Ti and the Al adding happened simultaneously. Otherwise, in the presence of only Ti added, a deleterious plates structure to strength was generated. Successively, in the late '50s, the further strengthening FCC two cubes stacked secondary phase γ'' , was discovered by "Eislestein" during its compositional experiments concerning the IN718 Superalloy (Sims, 1984).

Nevertheless, γ' and γ'' was not the only peculiar phases discovered and of which the metallurgists benefitted. It was also taken advantage from M_{23}C_6 , M_6C and MC carbides formation, which provided strengthening either by heat treatment or by the formation of adjunctive γ' thanks to the MC interaction with the γ matrix, the former acting as sumps

providing carbon for the phase transformation. As the representative of this latter case, is here just below reported the reaction expression (5) (Sims, 1984).



Furthermore, in the same '50s, the $M_{23}C_6$ were also discovered to be as dispersed phases within the gamma matrix, acting like bonding agents between different grains, therefore, creating a further strengthening configuration. However, around 1970 was discovered the far better Hafnium strengthening effect. The Hafnium addition, promoted indeed a contort grain formation hence, generating a grains interrelated network that physically made obstruction to the displacement of the components (Sims, 1984).

With the advent of the '60s, the Oxides dispersion strengthening (ODS) were introduced as promoters of improved creep resistance. With the oxides insertion of ThO_2 and Y_2O_3 , was hence possible to keep the superalloy's mechanical properties unchanged up to approximately 80-90% of the material's melting temperature. Another method adoptable wanting to improve the superalloys mechanical properties, instead of modifying its chemical composition, is to promote a rapid and directional solidification. In this way, it was indeed possible to create fibrous eutectic phases starting from TaC, $M_{23}C_6$ and δ -phase reserves. Moreover, a rapid cooling was discovered to be an optimal means to suppress deleterious phases such as σ -phase, μ -phase and Laves-phase besides to induce a directional grain growth. These, have been indeed dreaded from the metallurgists because of their brittleness and plate shape, inducing cracks formation whenever the component was subjected to creep conditions (Sims, 1984).

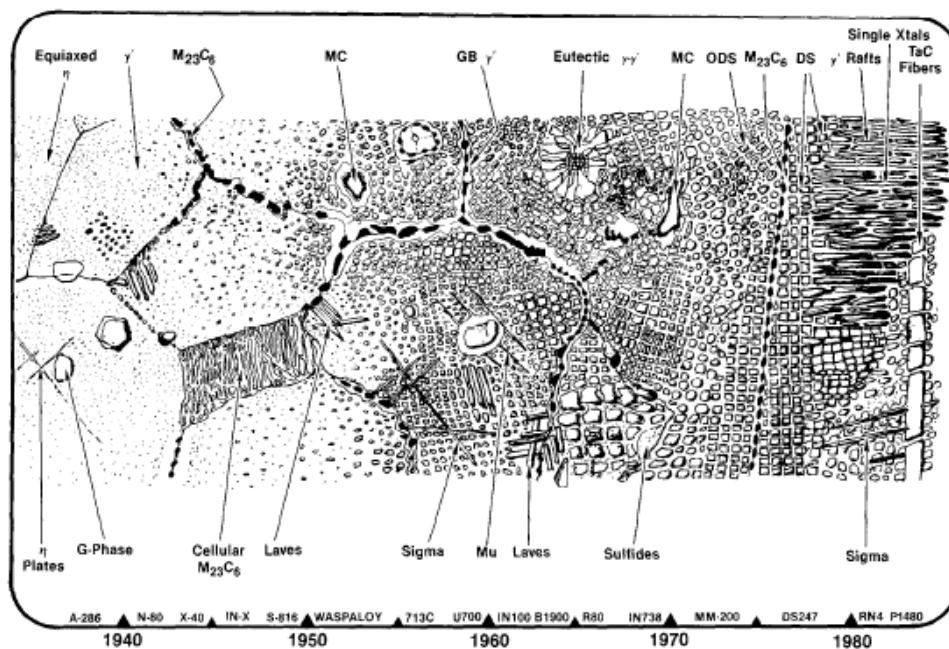


Figure 2.28: Main Ni-based superalloy phases throughout their years of discovery (Sims, 1984).

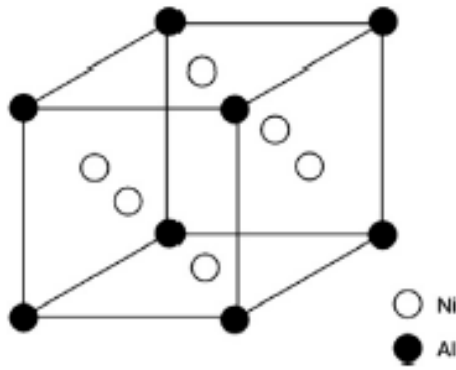


Figure 2.29: γ' - FCC Bravais lattice (Minet *et al.*, 2019).

(Superalloys strengthening mechanism and classification)

Generally, the remarkable Superalloys capability to withstand at high temperatures and hostile environments, preserving their mechanical properties is mainly due to two strengthening mechanisms (Minet *et al.*, 2019):

- Strengthening by solid solution of the γ matrix
- Hardening by precipitation of the γ' $\text{Ni}_3(\text{Al}, \text{Ti})$ and the γ'' $\text{Ni}_3(\text{Nb})$ phases (Minet *et al.*, 2019)

2.8.2 Strengthening by Solid Solution

As reported in Table 4, a great variety of alloying elements can be present in Ni-based superalloys. According to that, a substitutional solution can occur, leading some chemical elements to substitute the matrix atoms in their lattice position. As a result, around these lattice positions, because of the mismatch between the “hosts” atoms and the matrix atoms radii, a strain field interacting and making obstruction to that of the passing dislocations during plastic deformation, is generated. Furthermore, a further strengthening effect is also provided when the substitutional elements have a higher Young’s modulus respect to that of the matrix. This strengthening phenomenon generally concerns the γ matrix rather than the γ' phase because of its highly ordered microstructure (Goodfellow, 2018).

2.8.3 Hardening by Precipitation

Another strengthening mechanism is the γ' phase precipitation. While the dislocations displacement quite easily deforms the disordered γ matrix, higher energy is required to them in order to alter the ordered γ' precipitates lattice. Depending on the precipitated particles’ size, two different phenomena occur (Goodfellow, 2018).

In the case of small γ' particles, the same are traversed in two different moments by a couple of two different shearing dislocations: a “leading” and a “trailing” dislocation. As the first interacts with the γ' lattice, the Al atoms replace the Ni ones in their lattice positions, entailing to an energy increase as a result of a bridging zone between the two dislocations (termed as Anti-phase region), creation. After that, the first is passed, the trailing dislocation traverses the Anti-phase region restoring the initial lattice order. This phenomenon responds to the name of “Weak pair coupling” (Goodfellow, 2018). Otherwise, because of the higher Anti-phase

boundary energy (APBE) present in large particles subjected to shearing forces, the trailing dislocation interacts with the precipitates Anti-phase before that the leading one leaves. This latter phenomenon is defined as “Strong pair coupling” (Goodfellow, 2018). However, it is not unambiguous to determine which mechanism offers a higher strengthening effect. For instance, in the case of the supersolvus IN100 alloy, small precipitates entail to higher yield strength than that achievable with larger ones.

On the other hand, the trend is reversed in the instance of subsolvus IN100, where the presence of large γ' particles provides a strengthening effect superior to the supersolvus case. Finally, concerning overaged alloys, therefore characterised by very large particles (around 1 μm), an Orowan strengthening mechanism is also possible even though rarely present in Ni-based superalloys because of meager values of mismatch intercurrent between the precipitates and the matrix (Goodfellow, 2018). Finally, it is essential to specify that the two mechanisms just exposed are only the two considered as owning a most relevant impact on the superalloy properties. Several further mechanisms such as stacking faults, modulus and chemical strengthening, grain boundary strengthening and coherency strengthening provide their contributions to increase the yield strength. However, in the instance of Ni-based superalloys, the contribution of the stacking faults and the chemical-modulus strengthening can be considered negligible, whereas the coherency and grain boundary action are considered not as efficient as the two main mechanisms just reported (Goodfellow, 2018).

2.8.4 Alloying elements

The abundance of varied alloying elements promotes the complex superalloys' microstructure and the great variety of different phases. For each of them is here just below listed their effects and influence on the alloy.

Table 4: Alloying elements typically present in Ni-based superalloys

Alloying Element and its typical percentage concentration	Microstructural effect and influence on the superalloy's properties
<p>Co (2-15%)</p>	<ul style="list-style-type: none"> • increases the microstructure stability • reduces the γ' solvus temperature • reduces the stacking fault energy (γ_{SFE}) • partitions the dendrites core (Tapia, 2006)
<p>C (0.05%)</p>	<ul style="list-style-type: none"> • Increases the microstructure stability • Increases rupture strength at high temperatures • Increases the low angle grain boundaries tolerance • Induces refractory elements to the dendrites core partitioning it (Tapia, 2006)
<p>Rh (0-9%)</p>	<ul style="list-style-type: none"> • Solid solution strengthener • Increases the liquidus temperature • It partitions to the dendrites core (Tapia, 2006)
<p>Re (0,3,6%)</p>	<ul style="list-style-type: none"> • It retards γ' coarsening ((Minet <i>et al.</i>, 2019)) • Solid solution strengthener • Increases creep resistance, thermal capability and liquidus temperature although affecting the microstructural stability • Can lead to deleterious phases growth in the dendritic zone (Tapia, 2006)
<p>Cr (10-20%)</p>	<ul style="list-style-type: none"> • It forms M_7C_3 ((Minet <i>et al.</i>, 2019)) • improves hot corrosion and oxidation resistance (Cr_2O_3) • reduces the γ' solvus temperature and the antiphase boundary energy of the γ' phase (γ_{APB}) • must be remarkably reduced in 2nd and 3rd generation alloys in order to increase the microstructural stability (Tapia, 2006)

Al
(3-6%)

Ti
(0-5%)

Al/Ti

Ta
(4,12%)

W
(5-8%)

Ta/W

Mo
(0-3%)

Nb

Hf
(0-0.2%)

- primary γ' former
- improves material castability
- improves oxidation resistance (Al_2O_3)
- partitions to the inter-dendritic region (Tapia, 2006)
- can promote η -phase formation ((Sims, 1984))
- It forms MC ((Minet *et al.*, 2019))
- γ' former
- γ' strengthener
- Decreases the oxidation resistance
- Increases the hot corrosion resistance (Tapia, 2006)
- can promote η -phase formation ((Sims, 1984))
- High oxidation resistance whether the ratio increases
- High hot corrosion resistance whether the ratio decreases
- The vice versa are both valid (Tapia, 2006)
- It forms MC ((Minet *et al.*, 2019))
- γ' former
- Strong solid solution strengthener
- Increases the (γ APB)
- improves material castability (Tapia, 2006)
- It forms MC ((Minet *et al.*, 2019))
- γ solid solution strengthener in synergy with Re
- increase hot corrosion susceptibility
- decreases material castability
- decreases microstructural stability (Tapia, 2006)
- High castability whether the ratio increases
- The vice versa is valid (Tapia, 2006)
- It forms MC ((Minet *et al.*, 2019))
- γ' solid solution strengthener
- decreases microstructural stability
- it partitions to the dendrites core (Tapia, 2006)
-
- It forms hardening precipitates and or intermetallics ((Minet *et al.*, 2019))
- It forms MC and M_6C carbides (Tapia, 2006)
- It forms MC ((Minet *et al.*, 2019))
- Increases the adherence of the oxide to the metal substrate
- promotes contort grain growth (Tapia, 2006)

3. IN 718 and DED

As just reported in the previous section, the Ni-based superalloys present a complex and miscellaneous microstructure. Although several studies concerning the microstructure achievable in an IN718 part built by DED have been run so far, it is still a hard job to understand the complete microstructural framework and how the features are related to the process parameters. What seems to be clear, is that because of the high cooling rates, temperature gradients, and high temperatures involved during the deposition, the microstructure obtained is directly related to the part's thermal history, which is influenced by the process parameters as well as plenty of other factors. For instance, the component geometry and the thickness transitions, directly influence the heating storage (or dissipation as well) within the part (Shamsaei *et al.*, 2015). Therefore, depending on the parameters set and on the boundary conditions, various microstructural features are achievable with their consequent translation in specific mechanical properties. In fact, according to particular grain size, grain type, texture, and phases, the part's mechanical properties vary (Akram *et al.*, 2018).

3.1 "Melt Pool"

The primary feature to be considered in order to understand the AM microstructural morphology is the "Melt Pool," or else, the region melted by the laser source composed by molten substrate and supply material or by supply material and a layer previously deposited.

As the deposition starts, the laser source employed in the LBMD process is focalised thanks to a focusing optics system, in a narrow region on the substrate. The maximum energy density is then verifiable in correspondence to the minimum laser spot size, which resides in the focal plane. However, it exists an energy range sanctioned by the "Buried spot region" and the "Exposed spot region," within which the laser can melt the substrate and the fluxing particles so generating the Melt Pool (Figure 3.1). Whether the substrate distance deviates too far from the focal plane overcoming either the upper or lower limit, the energy density results to be not enough to create the Melt Pool (Gibson, Rosen and Stucker, 2014).

Typically, the focal plane is set around 1 mm below the substrate surface, so creating a hot zone partly composed by the melted substrate and partly by the melted powder particles. However, depending on the specific application, a higher or a lower amount of the substrate material is desired to be melted. For instance, when the supply material and the substrate are composed of two different material, and it is desired to minimize their mixing which could entail to deleterious intermetallic phases, it is possible to reduce the substrate melting, limiting its exposure by setting the focal plane out of the substrate surface (Gibson, Rosen and Stucker, 2014).

Therefore, once that the first requirement of appropriate energy density is respected, the Melt Pool is generated and then regulated in its main features and morphology accordingly to the process parameters set (described in section 2.6.2.2.1).

3.1.1 Chemical-Physical aspects

The Melt Pool can be moreover defined as a thermodynamically unstable zone because of the various physical phenomena that arise due to the high inner energy involved. More specifically, this high energy value is due to the heat transfer (convective) and the interactions between the liquid and the solid walls as well as the continuing entering powder particles (Thompson *et al.*, 2015). More in general, from a physical perspective, three main aspects must be considered: "the local solidification rate within the Melt Pool", "the ratio between the cooling rate and the thermal gradient R " and "the temperature gradient at the solidus-liquidus interface G " (Shamsaei *et al.*, 2015).

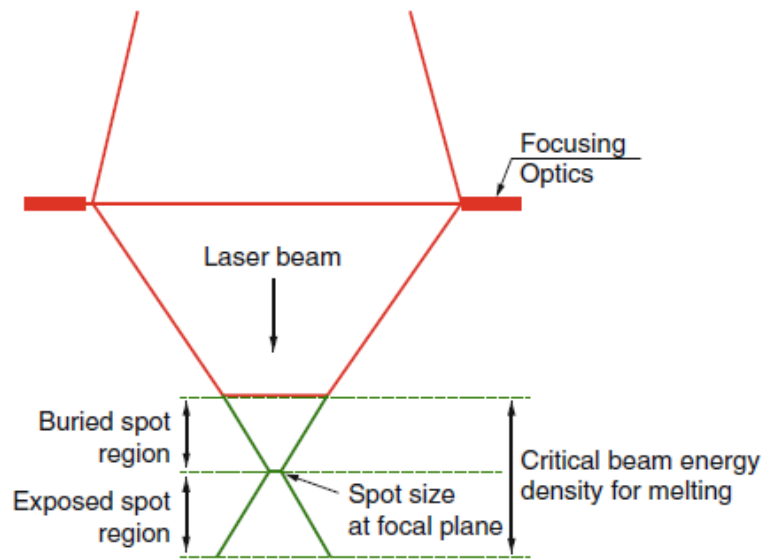


Figure 3.1: Melting energy density range in relation to the laser beam focalization (Gibson, Rosen and Stucker, 2014).

As a result of these aspects understanding, an insight of the microstructure morphology can be deduced. The ratio G/R influences the solidus-liquidus interface shape, whereas the cooling rate $G \times R$ the grain dimension. More in detail, an increase in the cooling rate $G \times R$ (generally 200-6000 K/s) leads to a finer microstructure while more modest values promote a microstructural coarsening. Otherwise, increasing the ratio G/R , the microstructural morphology tends to result in a columnar shape instead of an equiaxed one (Shamsaei *et al.*, 2015).

Because of the strict dependence of the microstructure to several boundary conditions, it would be too onerous in terms of time and set experimental tests to correlate the microscopical analysis with the process parameters iteratively. At this purpose, dynamic software simulations can be run, since their enough reliability predicting the grain growth, the texture and the morphology of the grains as well (Akram *et al.*, 2018).

3.1.2 Dynamic Melt Pool and grains morphology

The main features that characterise the melt pool geometry are width, length, fusion depth and fusion zone profile. While the deposition head is moving, hence depositing the supply material, the melt pool geometry results to be elliptically shaped in the X-Y plane, in response to the dynamic trailing effect. At the same time, in the Y-Z plane, the external surface results to be curved shaped because of the powder particles accumulation in the narrow region of the laser interaction (Figure 3.2). This latter feature is usually termed “Bead” (Wei *et al.*, 2019).

A crucial aspect that must be considered in order to understand the Melt Pool-Layer morphology is the heat transfer occurring during the cooling/solidification. The heat generated during the deposition is mainly dissipated accordingly conductive phenomena throughout the substrate (or the already solid material as well) and through the convective flow present within the molten metal. Because of the very high-speed flow generated within the Melt Pool (on the order of 300 mm/s), it can also be said that this latter mechanism is the primary factor governing the thermal exchange and the fusion zone profile hence, the geometry achieved after cooling.

As an example, a convective flow with a pronounced z-axis flow motion component entails a deep melt pool (Wei *et al.*, 2019).

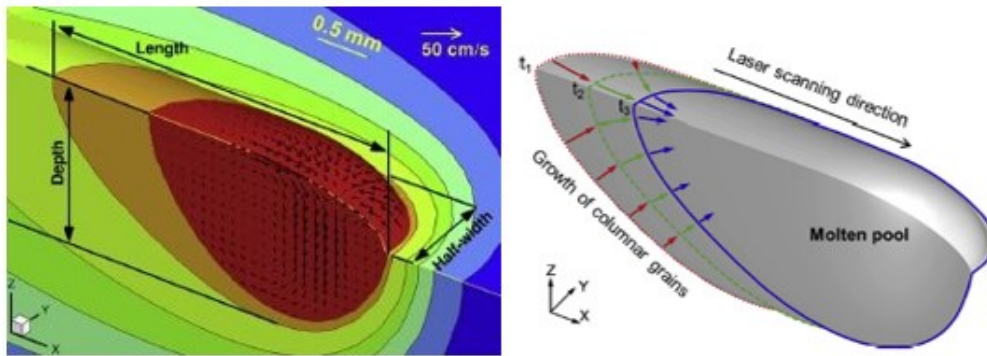


Figure 3.2: Dynamic Melt Pool (on the left) and dynamic columnar growth (on the right) (Wei *et al.*, 2019).

As the deposition starts, the Melt Pool dimensions are not precisely defined before a time-lapse of around a half-second. After this short time, the quasi-steady regime is reached, and fusion depth, melt-pool length and width, remain constant along with the deposition speed (Wei *et al.*, 2019). Also, since the “G” and “R” are locally constant, according to their values, it is, therefore, possible to locally predict whether the grain morphology is columnar or equiaxial. Furthermore, the software simulations highlight that the grain growth occurs according to the maximum heat flow direction thus defined by the respective G local values. More specifically, the grain growth detected within a DED melt-pool takes place starting from the partially melted overlaying grains, from which the new grains grow epitaxially. The direction of the new solidified grains is perpendicular to the melt-pool boundary and directed towards the melt-pool centre (Figure 3.2). Nevertheless, also the scanning direction directly affects the grain morphology since, according to the laser displacement, the grains bend their axis (Figure 3.4) (Wei *et al.*, 2019).

3.1.3 Melt-pool cross-section morphology

Analysing a melt pool cross-section (Y-Z plane), the results mentioned above find confirmation. Thanks to H.L. Wei *et al.* it is possible to observe an etched melt-pool analysis, where predicted and experimental results are juxtaposed and compared (Figure 3.3). According to what already stated, it is here possible to easily recognise in both the instances, a fine and columnar microstructure at the melt-pool boundary and coarse equiaxial grains in correspondence of the central zones. Furthermore, just below the Melt Pool top, the microstructure is generally composed of fine equiaxed grains. It is also meaningful, to consider that the grains developing from the boundary line, reside in the Y-Z plane whereas that located in the inner and upper zones, result to be sectioned along the Y-Z plane since bent towards the scanning direction; hence sticking out of the plane (Wei *et al.*, 2019).

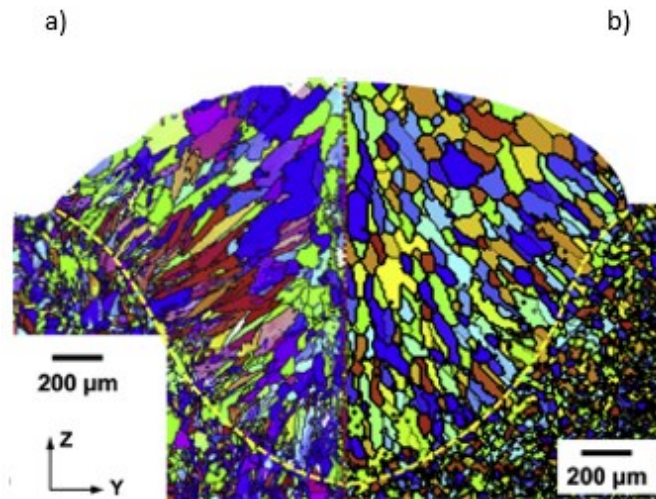


Figure 3.3: Melt Pool grains morphology – a) grains morphology simulation, b) grains morphology experimental results (Wei *et al.*, 2019)

3.2 Single Wall

Wanting to analyse a more complex feature as a single wall it is, further aspects must be considered to describe its microstructural morphology. Since the grain morphology is dependent on the thermal history, some remarkable grains modifications occur when the deposition process is iterated by overlapping new layers upon the previous ones. When the second layer is deposited on the first, part of the heat appointed to the deposition is transferred to the underlying layer so causing metallurgical alterations (Wei *et al.*, 2019).

3.2.1 Grains morphology

More specifically, the grains residing on the upper zone of the first layer, experience a coarsening as severe as the transferred heat amount is relevant. Furthermore, an out-and-out boundary is established between the grains of the first layer, acting as nuclei sites, and the grains growing within the second one hence, giving rise to epitaxial growth. Because of this microstructural jointing mechanism, during the wall building the curvature of the grain, (as described in the previous paragraph) is progressively transposed upwards. As a new layer is deposited, the part of the grain of the overlying layer is straightened to a certain residual tilt angle whereas, the grains of the new layer present the curvature in question (Figure 3.4). According to what just described, the resulting core grains exhibit a columnar growth which is bent according to the deposition direction (Figure 3.4) (Wei *et al.*, 2019).

Furthermore, due to the cyclic heating/cooling to whom the grains are progressively subjected, they experience the as named “solid-state growth”. In fact, according to the Gibbs Free Energy minimisation principle, the grains tend to enlarge/reduce their size depending on their surface energy in order to institute a new physical equilibrium. The results obtained by H.L. Wei *et al.* are reported in Figure 3.5.

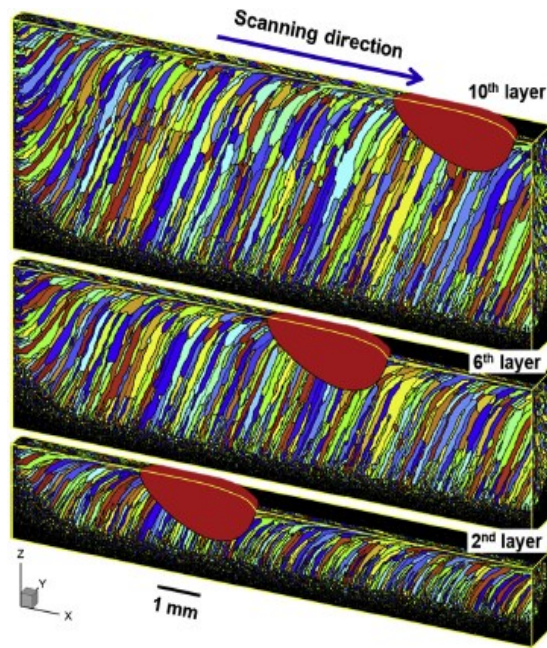


Figure 3.4: Single wall X-Z section depicting the grain morphology after 2,6,10 overlapped depositions (Wei et al., 2019).

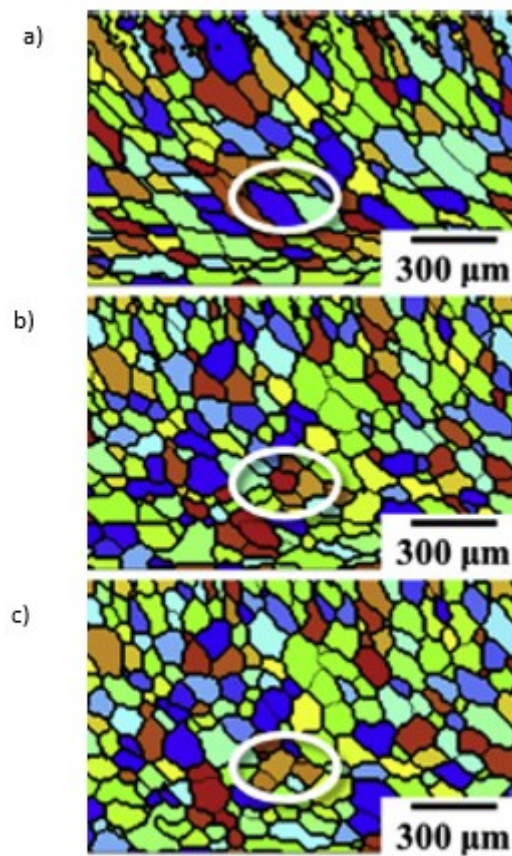


Figure 3.5: Punctual analysis in an XY cross-section, of the grain coarsening as a consequence of the thermal cycling induced by the deposition of successive layers – a) after deposition of the fourth layer, b) after deposition of the fifth layer, c) after deposition of the sixth layer (Wei et al., 2019).

3.2.2 Microstructure and phases

As already mentioned, about the grain morphology obtained by DED, the grains grow accordingly to either a columnar or equiaxed shape. About a compositional perspective, the γ phase is predominantly detectable in the dendritic structure and, more precisely, in the dendritic core. The explanation for that is verifiable in the cooling phenomenon (Kumara *et al.*, 2019).

As the deposited material cools down, some elements such as Nb, Mo and Ti segregate in the inter-dendritic zones because of their low solubility within the γ matrix. As the cooling process proceeds and the γ phase solidifies, these elements are progressively relegated to the liquid phase because of their chemical incompatibility with the γ -Fe phase. As a result, these elements promote the formation of deleterious phases such as Laves- and δ - phases, NbC and TiN at the grain boundaries. These, are potential cracks promoters (Kumara *et al.*, 2019).

From a thermodynamic perspective, is moreover relevant the effect induced by the Nb, Mo and Ti, appointed to alter the TTT and the CCT curves of the γ' and γ'' phases in the inter-dendritic zones. In fact, as the content of alloying elements increases, the TTT and CCT curves result to be displaced towards lower precipitation time at the parity of applied temperature respect to that associated to the dendritic core zones (Figure 3.8,3.9). Therefore, this effect entails to the confirmation of the remarkable increase of the γ' and γ'' density in the inter-dendritic zones, as opposed to the dendritic core mainly rich in γ phase after the cooling (Kumara *et al.*, 2019).

Another critical aspect of being considered, as already done for the grains' morphology, is the effect of the thermal cycling on the phases. At this purpose, C.Kumara et al. performed a thermal simulation addressing the possibility that in the first deposited layer the γ' and γ'' phases could change because of the thermal cycling effect induced by the progressively further layers deposition.

However, in the case studied presented in Figure 3.6, even though the first layer can experience temperatures moving throughout the γ' / γ'' precipitation window manifold times, the time in charge of these transitions seems to be too meagre to promote a relevant γ' / γ'' phases coarsening. These considerations are indeed indirectly found, by performing hardness tests which substantially reveals very close hardness values to that of a single layer cooled. Therefore, this result is per a not preponderantly austenitic phase increase. Finally, referring to the results reported in Figure 3.6, also the Laves phases do not show any form of alteration in consequence of the repeated heating. The second cycle does not provide enough thermal energy to overcome the 1000°C; the temperature at which diffusion and Laves dissolution can occur (Kumara *et al.*, 2019).

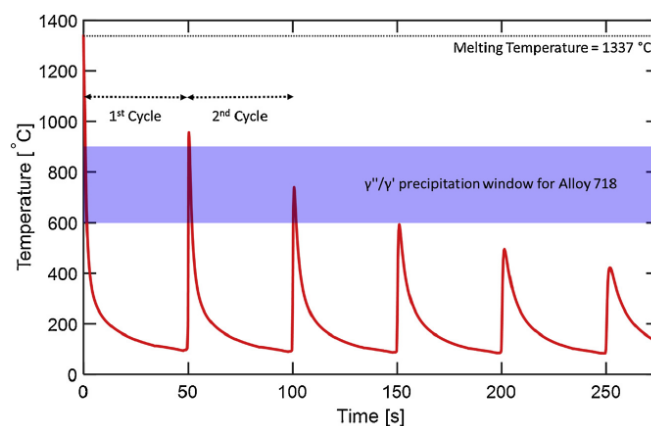


Figure 3.6: Thermal cycling effect of the first layers deposited (Kumara *et al.*, 2019).

However, more, in general, it is assumed that the layers interested by metallurgical alteration because of their re-heating, are the first 5-6 deposited (Figure 3.7)(Sames *et al.*, 2016). These experience a temperature major than around 900/1000 °C with consequent precipitation of hardening phases.

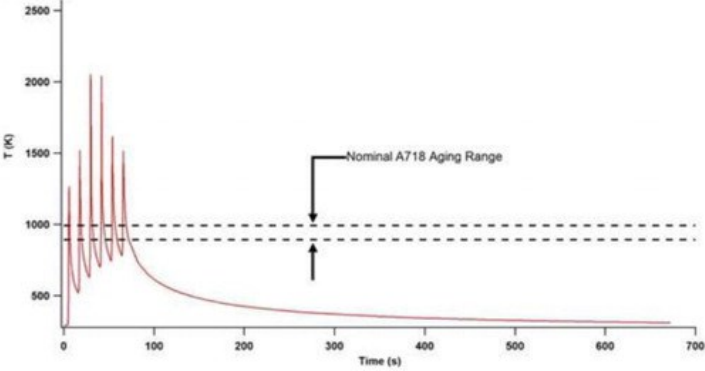


Figure 3.7: Thermal history of a single point in a depositing part built by DED (powder feeding) (Sames et al., 2016).

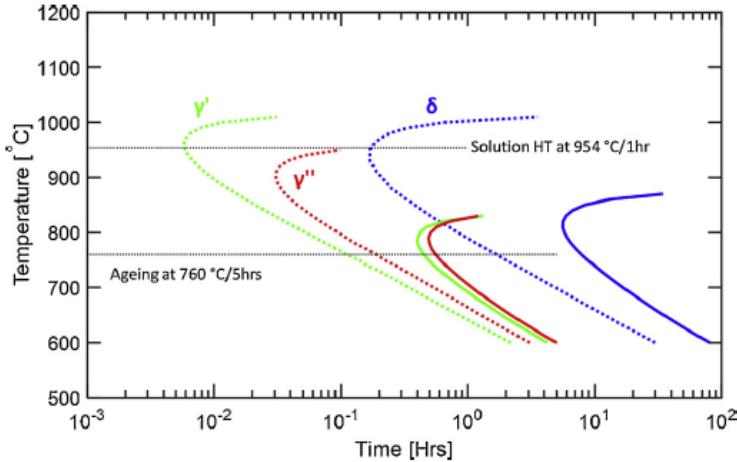


Figure 3.8: γ' , γ'' and δ phases TTT curves respectively related to the inter-dendritic zones (dashed lines) and the core zones (continuous line)

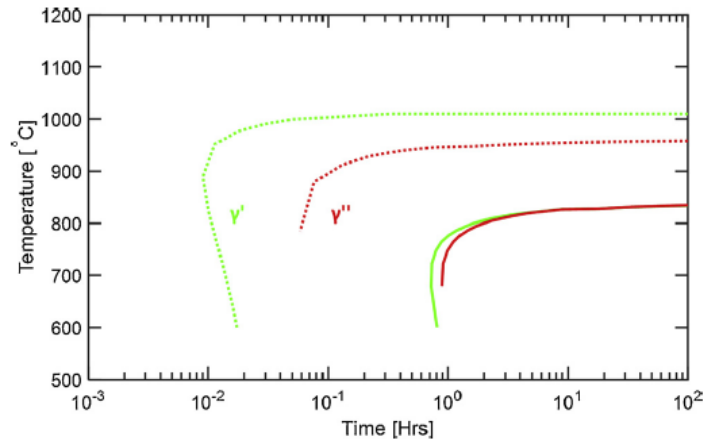


Figure 3.9: γ' and γ'' phases CCT curves respectively related to the inter-dendritic zones (dashed lines) and the core zones (continuous line)

3.3 SEM / EBSD Analysis in “as-deposited conditions.”

The microstructural results just exposed and supported by software simulations analysis, find confirmation also in the experimental tests. The more accurate and reliable method to analyse the effects exerted by the process parameters on the microstructure is still the experimental characterisation which generally confirms and better specifies the simulations results.

3.3.1 SEM / EBSD: Morphology & Texture in “as-deposited conditions”

At this purpose, some results achieved in different studies, are reported as representative of some notable cases. It is possible to directly validate the microstructural morphology as well as the presence of eventual defectology, employing a microscopic SEM analysis. Nevertheless, this characterisation method can be easily coupled with EDS and EBSD analysis. The former considers the compositional aspects of tracking and measuring the percentage of the chemical elements present; the latter otherwise is times to provide structural data such as grains morphology/orientation and related matters (BRUKER, 2019).

Zhang Qun-li et al. reports his study about a parameter optimisation run on an IN 718 “Layer” deposited on an IN718 substrate by LMD. The exposure parameters used are reported as follows: Laser Power 650W, Scan speed 6.7 mm/s, Spot size 1 mm and specific energy of 6.45 g/min (Zhang, Yao and Mazumder, 2011).

Referring to a specific case study are here presented some micrographs highlighting the most remarkable features in terms of microstructure and grains morphology. In figure 3.10 is reported a micrograph acquired by SEM, depicting the matching zone between the as-deposited layer and the substrate. The as-deposited material microstructure evolves epitaxially accordingly a directional solidification, promoted by the high-temperature gradient intercurrent between the upper and the lower zones. As a result, the grain morphology results to be dendritic and columnar shaped. Besides, considering the alloy composition considered and to the process parameters set, no HAZ has been detected in the substrate region nearby at the bonding zone (Zhang, Yao and Mazumder, 2011).

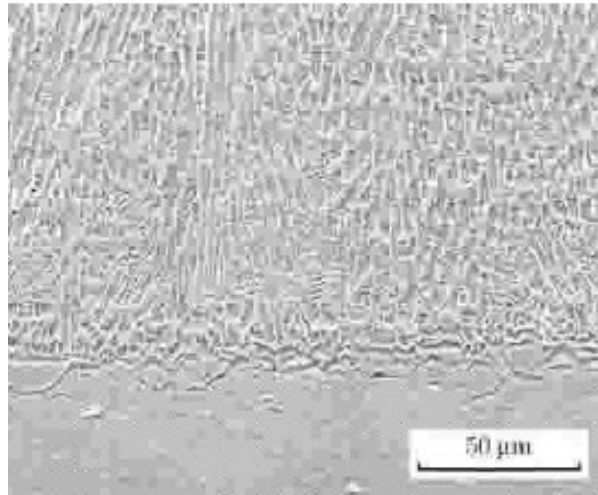


Figure 4.10: SEM analysis of an IN718 layer deposited on an IN718 substrate: bonding zone (Zhang, Yao and Mazumder, 2011)

Moving upwards in the same micrograph, the G/R ratio decreases. Therefore, the equilibrium sponsoring the directional solidification and then the columnar grain growth fails. Fine and equiaxed austenitic single-phase grains (constituting the major part of the feature itself) are generated and localised in the central zone of the feature because of the high cooling rate (Figure 3.11). Moreover, for what concerns the strengthening phases γ' and γ'' , they cannot precipitate forming separate phases due to such limited cooling time-lapse which denies the possibility to form newly organised phases. As a result, these strengthening phases dissolve within the γ matrix and the dendrites trunk. As evidence, the Mo, Nb and Ti relatively low segregation ratio [respectively: (0,689 – 0.520 – 0.688)(mass%)] entailing so to modest mechanical properties in terms of hardness and obviously of strength (Zhang, Yao and Mazumder, 2011).

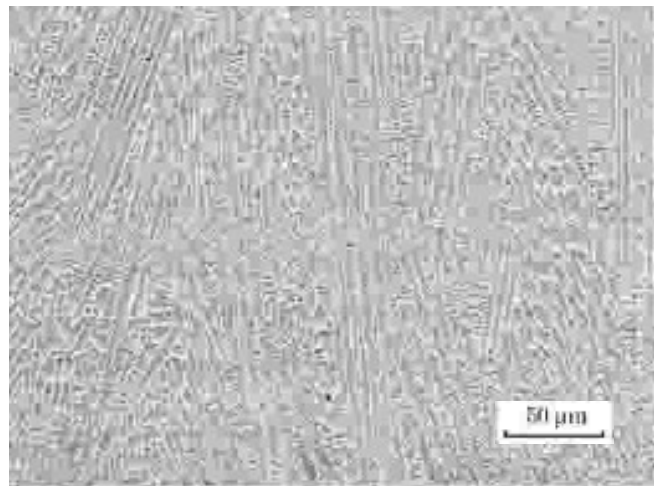


Figure 3.11: IN 718 columnar transition zone to equiaxed shaped grains (Zhang, Yao and Mazumder, 2011)

On the other hand, Lakshmi L. Parimi et al. analysed the microstructural issue somewhat differently from the authors aforementioned. In this study, they have been indeed considered two regimes of Laser Power employed (Low and High) and their combined effects with the adoption of three different scanning strategies: B1 Unidirectional (It *, Lp*), B2 Bidirectional (no It *,Lp*), and B3 Bidirectional (no It *,Hp*) (Parimi *et al.*, 2013).

According to that what just mentioned, is therefore here directly addressed the thermal history issue, as not only dependent on the specific component geometry or the features thickness transitions, but rather primary related to the scan strategy (and to the exposure parameters as well).

In B1 and B2, the grains result to grow inclined accordingly to the scanning direction of a draft angle, respectively of $50\text{-}60^\circ$ and $75\text{-}85^\circ$ (Figure 3.12 a,b). However, because of the different choice of scan strategy, the results remarkably defer in terms of grains orientation. The bidirectional deposition in B2 entails to grains growth towards opposite directions and intersecting each other at 90° - 100° when two different layers are overlapped. On the other hand, in B1, the grains tend to grow slightly bent towards the deposition direction, although it is not recognisable a continuous growth of grains belonging to different layers. Also, another essential feature to be highlighted is the interposition of a “fine grain band” between two successive deposited layers with the B1 approach. This particular feature is due to the low laser power adopted then not sufficiently effective to re-melt the overlaying grains and joint them to that depositing (Figure 3.12d). Otherwise, an epitaxial grain growth, coherent throughout the layers, is detectable in the samples B3 where columnar grains 2-3 mm long develop at 50° - 60° (Figure 3.12c) (Parimi *et al.*, 2013).

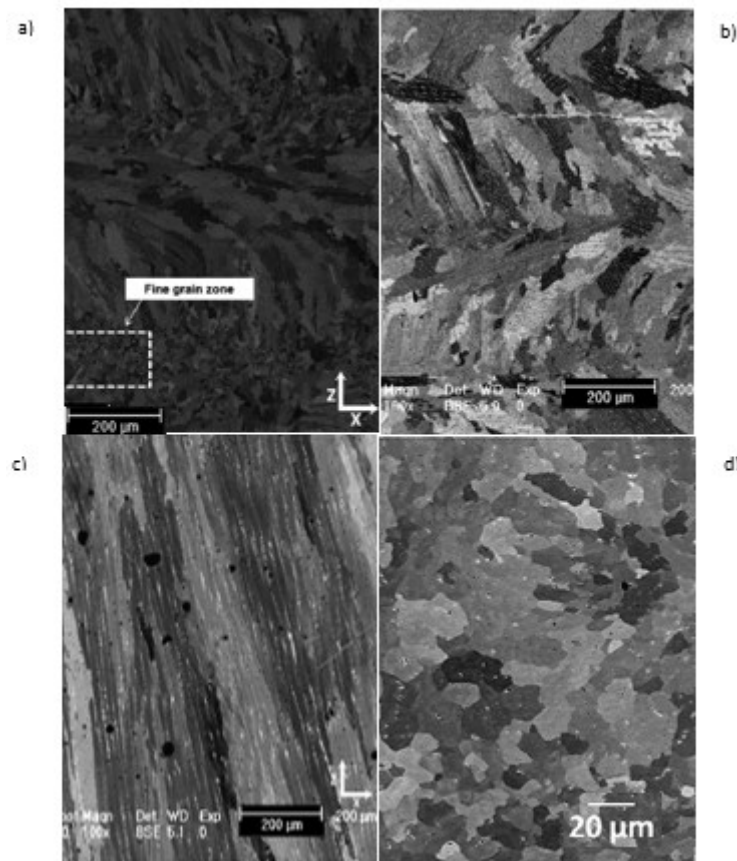


Figure 3.12: SEM micrographs of multiple layers deposition accordingly to different scan strategy and exposure parameters values: a) B1 Unidirectional deposition with L_p^* , b) B2 Bidirectional deposition with L_p^* , c) B3 Bidirectional deposition with H_p^* and d) Detail of the Fine-grain zone present in a (Parimi *et al.*, 2013).

*It **: Idle time of around 6s deriving from the laser source switch off as the current track is deposited and the time required to displace the deposition head at the track start. During the deposition head motion, the powder stream is kept fluxing so that to force more the previous track cooling.

L_p: (Low Laser Power) 390W of laser power employed in conjunction with a laser scan speed of 200 mm/min and a powder flow rate of 18 g/min.

H_p: (High Laser power) 910W of laser power employed in conjunction with a laser scan speed of 200 mm/min and a powder flow rate of 18 g/min.

Thanks to an EBSD analysis, Lakshmi L. Parimi et al. deeply investigated the three builds texture. Taking into consideration a more substantial zone of study is possible to address the microstructural continuity issue directly. As aforementioned, in B1, a fine-grains band generated interposing between two successive layers is evident. More explanations related to this feature are provided in Figure 3.13a, where, in the B1 EBSD micrograph are recognisable alternating bands constituted by fine-grains structure randomly distributed. Furthermore, moving towards the build top, the band thickness considerably decreases because of the higher heat storage as a consequence of a lower and lower substrate chilling effect. Although the B2 sample is characterised by higher temperatures involved during the deposition as previously detailed, the same band is present between the alternating oriented layers, albeit with a more modest thickness and smaller grains size (Figure 3.13b). The fine-grain band is indeed caused by the high thermal conductivity of the IN718. Otherwise, in B3, no parting bands are detectable. In fact, the fine equiaxed grains generated at each layer Melt Pool top, are re-melted and they take part of the epitaxially growing grains leading to a continuous columnar structure parallel to (001) direction (as FCC), interrupted only when the last layer is deposited in short and independent columnar grains because of the high cooling rate promoted by the deposition atmosphere and by the meagre heat storage in the just below surface zone (Figure 3.13c) (Parimi *et al.*, 2013).

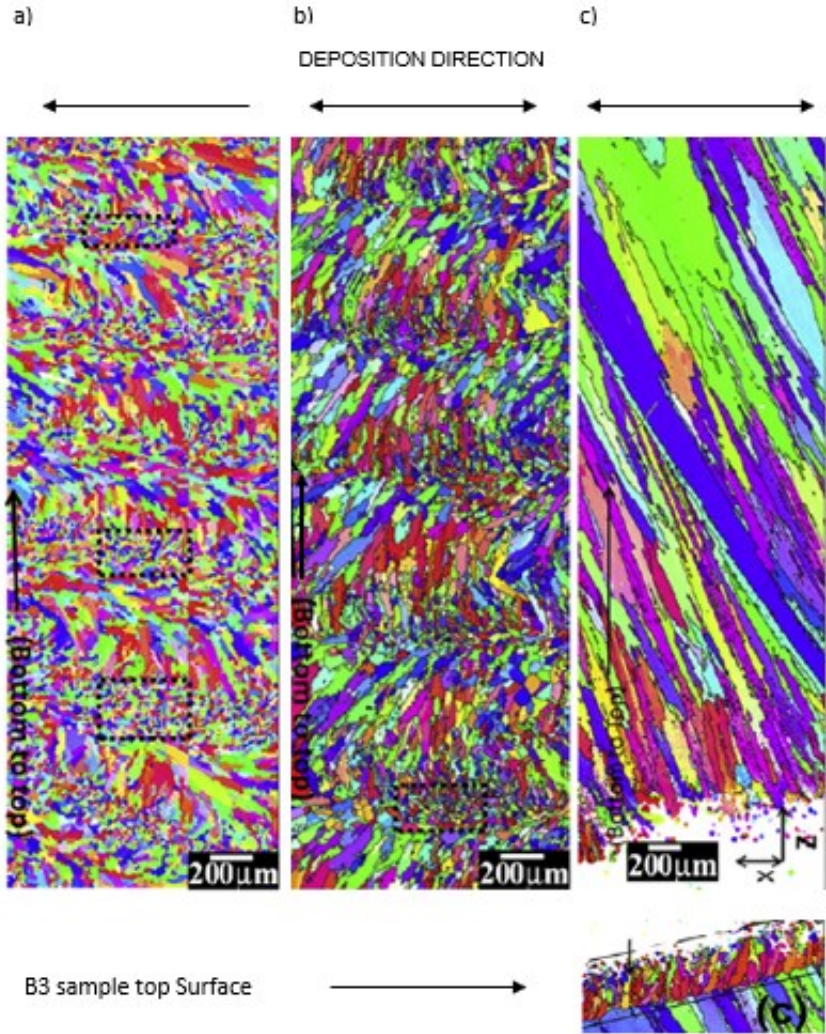


Figure 3.13: EBDS micrograph and texture a) B1, b) B2, c) B3 (Parimi *et al.*, 2013).

3.3.2 SEM / EBSD: Phases and chemical composition in “as-deposited conditions.”

The SEM analysis of the specimens, B1 and B2 reveals a heterogeneous microstructure in terms of phases present. In the inter-dendritic zones, irregular, circular and squared features are detected. These, thanks to an EDS analysis coupling, are then found as Laves phases and Carbides.

The formers are typically rich in Nb, Mo and Ti and mainly formed because of the Nb segregation leading to a composite interaction with other elements such as Ni, Cr and Fe. More precisely, the laves phase composition and stoichiometry are $(\text{Ni, Fe, Cr})_2(\text{Mo, Nb, Ti})$ instead of that of γ'' which is (Ni_3Nb) . Because of the Laves' detrimental effect on the mechanical properties, is generally performed a solution heat treatment to dissolve them within the matrix. Furthermore, it has been found a sort of correlation between the laser power employed and the laves particles size. According to that, more massive particles in size range of 20-30 μm and around 100 μm long, are found at high laser power (as for B3) hence, entailing a higher part cracking risk when in operation (Parimi *et al.*, 2013).

For what concerns the precipitates found ranging in size between 200-300nm and rich in Mo and Nb, it is reasonable to assume that are carbides. Nevertheless, as reported in Figure 3.14, finer carbides can be included within laves phases, whereas the coarser ones can be dispersed in the γ matrix (Parimi *et al.*, 2013).

Furthermore, observing Figure 3.15, it results clear how manifold phases generated from the elements mentioned above segregation, coexist in the same area. At high Laser Power employed as for B3, is not unusual to detect nearby laves phases (besides carbides), δ -phases needles shaped. Even though usually the δ -phases are generated by high temperatures applied for a relevant time-lapse (100h at 750-1000 ° C), they can anyhow rise in such fast and dynamic process, because of the large amount of heat stored during the deposition between the layers. Nevertheless, the δ -phase precipitation is sponsored by the stacking-faults sites that lower the minimum temperature necessary to make them nucleate. The reason why these phases are so monitored and undesired is due to their relevant brittleness that in conjunction with their acicular shape act as optimal crack initiators candidates.

On the other hand, it is also somewhat relevant to mention their strengthening effect at the grain boundary when the material in operation is subjected to creep conditions. However, the reader is reminded to consider that, as for the Laves and the γ' / γ'' phases, the thermal cycling induced by the successive deposition, generally does not cause relevant further coarsening of δ -phases as well. Assuming the thermal layer history previously reported in Figures 3.6 and 3.7, and considering that the δ -phase precipitation lapse it ranges between 750-1000 ° C with a maximum at 900 ° C, the temperatures in play and the time lapses dedicated to the precipitation, seem to be inefficient (Parimi *et al.*, 2013).

Also, it could be noteworthy, to analyse the same issue from an opposite perspective according to which, wanting to minimise the percentage of detrimental phases as the just listed are, an effective measure to adopt is to increase the cooling rate by appropriate process parameters set. To conclude, it can be said that at the parity of scan speed and feed rate as well, higher Laser Power entails to a remarkably homogeneous and columnar microstructure. This microstructure is moreover deemed stronger than that achievable at lower L_p , even though detrimental phases such as Laves and δ -phases or carbides as well, are present. Commonly δ -phases are not included in samples built at modest L_p ; however, they exhibit a heterogeneous microstructure indeed composed by columnar grains mixed to equiaxed ones, that in the overall show lower mechanical properties respect to that exhibited by samples B3 like (Parimi *et al.*, 2013).

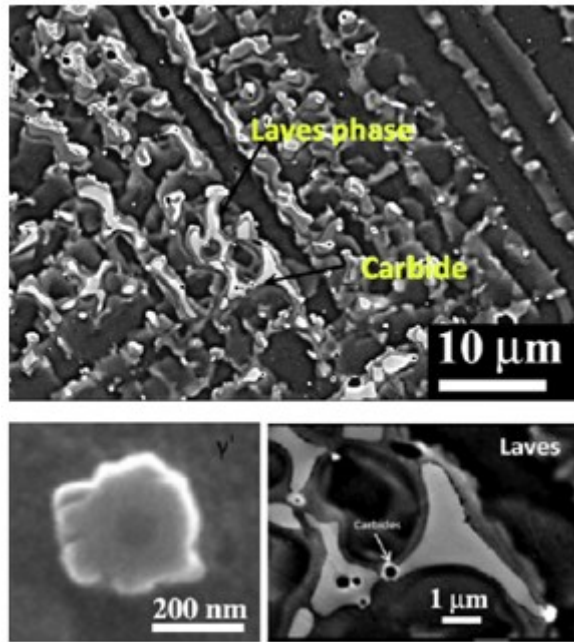


Figure 3.14: SEM micrographs reporting the Laves, Carbides and γ' phases in a B2 sample like (Parimi et al., 2013)

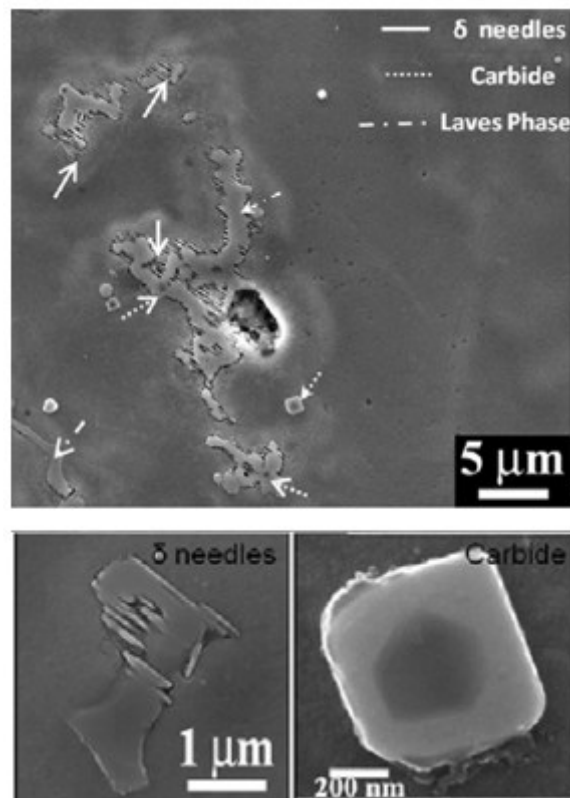


Figure 3.15: SEM micrographs reporting the Laves, Carbides and δ -phases in a B3 sample like (Parimi et al., 2013).

Finally, in Table 7 are reported the EDS scan results in terms of different chemical elements percentage which has been detected in different areas of the B2 sample. These have been then pertinently indexed concerning the specific phase that they may represent (Parimi *et al.*, 2013). At this purpose, to index the features depending on their chemical composition detected by EDS, it results of primary importance to analyse the Nb content. This parameter can be indeed assumed as threshold factor on which distinguishing the different phases. Table 5 provides some Nb content ranges to be intended as a general benchmark, whereas Table 6 details the alloying elements present about the different carbides types detectable in Ni superalloys.

Table 5: Typical Nb content of the phases present in the Ni superalloys

Phase	Nb content range (%)
γ Matrix	~ 4*
Carbides	~10 (also rich in Ti)
Laves	>17
δ phase	~5-8

*Note: During the EDS detection it can happen to record Nb values sensitively lower than the 4%. In this case, one of the most probable explanation is a depletion of Nb from the matrix, times to create Laves, carbides or δ -phases as well, in the neighbouring areas.

Table 6: Typical Ni superalloy carbides types and their alloying elements markers (Minet *et al.*, 2019).

Carbide type	Typical alloying elements
MC	W, Ta, Ti, Mo, Nb, Hf
M ₇ C ₃	Cr
M ₂₃ C ₆	Cr, Mo, W
M ₆ C	Mo, W, Nb

Table 7: EDS compositional results provided by Lakshmi L. Parimi et al., indexed with the phases they represent (Parimi et al., 2013)

Phase/Wt%	Al	Si	Ti	Cr	Fe	Ni	Nb	Mo
<i>Powder</i>	0,29	0,14	0,9	18,2	18,9	53,34	5,1	3,1
<i>Matrix</i>	0,34	0,14	0,8	19,44	18,68	53,7	3,73	3,18
<i>Segregation</i>	0,28	0,24	1,23	17,52	16,07	51,84	9,22	3,59
<i>Carbide</i>	1,33	0,11	9,19	16,8	14,97	43,35	11,45	2,8
<i>Laves</i>	0,27	0,47	1,3	14,82	13,46	47	18,37	4,31

4. Materials and Methods

In this experimental campaign, have been analysed three different types of features: 40 “Single Scan Tracks” (SSTs), 24 “Single Layers” (SLs) and 3 “Cubes”. Indeed, the laser-related parameters like laser power (P) and laser scan speed (SS) were selected according to the SSTs analysis, whereas the optimum hatching distance (Hd) was estimated according to the SLs. Nevertheless, the Cubes (realised with the optimal parameters chosen P 600W, F 750 mm/min and Hd 0.3 mm) have been analysed in their microstructural morphology, defectology presence and phases.

In this section are briefly detailed the operative procedures adopted in order to prepare the specimens for the different characterisation tests.

Furthermore, the equipment employed will be briefly introduced in conjunction with the tools and the expandable materials used such as polishing cards and pads, chemical etchant and lubricants.

4.1 Feedstock particles

The feedstock used to realise the features characterised in this campaign is constituted by gas atomised particles sphere-shaped with a coarse average size ranging between 44 and 106 μm .

Table 7, thanks to the courtesy of 4DHybrid group, reports the particles chemical composition investigated by EDS. The same result to be rich in Ni, Cr, Fe and Nb aside from with a not negligible Ti and Al presence.

Further specifications about the feedstock particles morphology and hallmarks will be moreover detailed in paragraph 4.3.1.3 pertinently to their influence on the deposition performances.

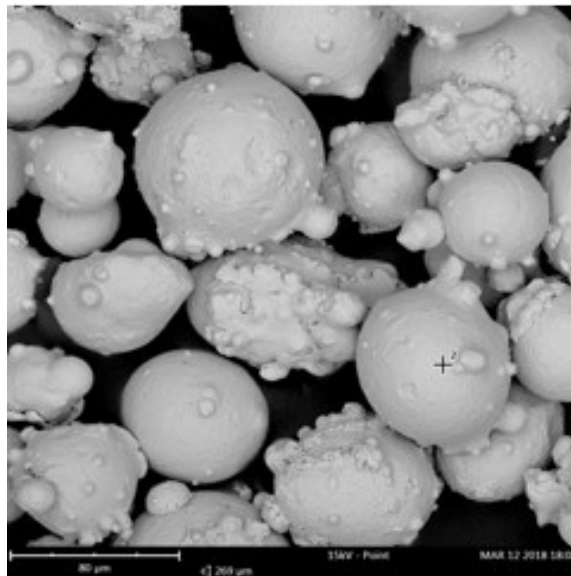


Figure 4.1: SEM Powder particles analysis

Table 7: Powder particles' feedstock chemical composition

Element	Atomic concentration	Weight concentration
Nickel	52.67±0.53	55.79±1.91
Chromium	18.76±0.77	17.67±0.20
Iron	19.04±1.59	16.15±0.29
Niobium	3.42±0.86	6.67±0.22
Molybdenum	2.09±0.05	3.88±0.11
Titanium	1.05±0.24	1.10±0.10
Aluminum	1.28±0.16	0.64±0.13

4.2 DED Machine

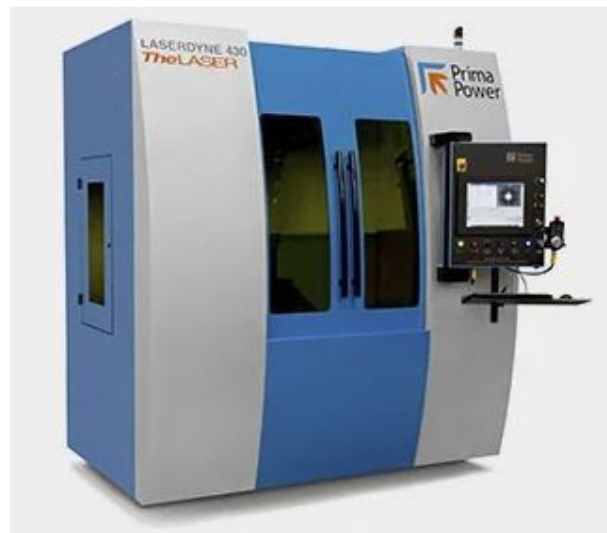


Figure 4.2: Laserdyne 430 - DED Machine (Laserdyne 430 | Primapower, no date).

Machine specifications (Laserdyne 430 | Primapower, no date)

- Work area
 - 3-4 axes:
X 585 mm, Y 400 mm, Z 500 mm, Rotary 360° (optional)
 - 5-6 axes:
X 585 mm, Y 400 mm, Z 500 mm, C 900°, D 300°, Rotary 360° (optional)
- Axis speed
 - 3-4 axes:
X, Y, Z: 15 m/min; Rotary: various options
 - 5-6 axes:
X, Y, Z: 15 m/min; C, D: 90 rpm; Rotary: various options
- Accuracy
 - 3-4 axes:
X,Y,Z: 12.5 µm; Rotary: various options
 - 5-6 axes
X,Y,Z: 12.5 µm; C, D: +/- 6 arc-sec; Rotary: various options
- Laser source: CW, QCW, pulsed fibre laser

4.3 Stereomicroscope

The “On top” characterisation dedicated to observing the external surface of the features in question, it has been run employing a LEICA EZ4W Stereomicroscope.

More specifically, thanks to this equipment it has been possible observing the SSTs from the top, at the two magnification of 10X and 12,5X, to evaluate their regularity and homogeneity of deposition.



Figure 4.3: LEICA EZ4W Stereomicroscope

4.4 Cutting

The IN718 Substrates have been cut with a Remet TR 100s cutting machine, employing a SiC CERMET blade driven by a semi-automatic mode.

The Substrates splitting, led so to the formation of several portions of substrate embedding a certain amount of features each as reported in the “Sampling” 3.2.1 paragraph.

Successively the sampled Substrates have been cut along their features cross-section so obtaining:

- 12 SSTs specimens
- 4 Layers specimens (Substrate 1)
- 6 Layers specimens (Substrate 2)
- 3 Bulks specimens



Figure 4.4: Remet TR 100s

4.4.1 Sampling

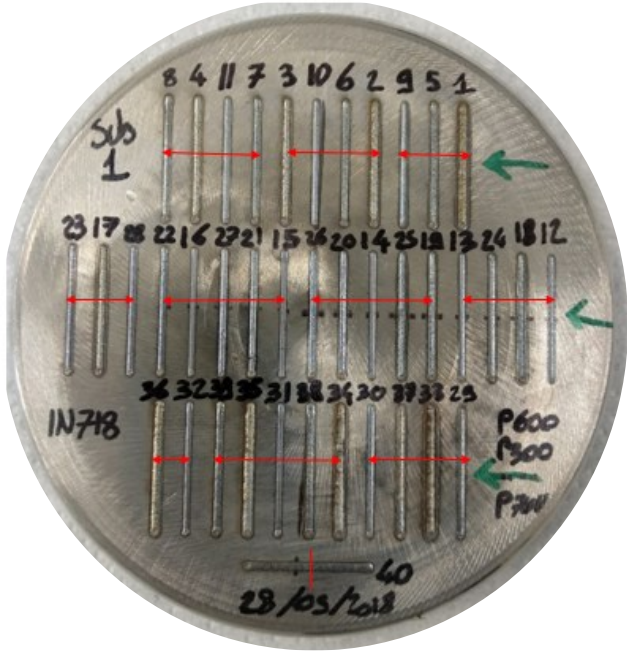


Figure 4.5: SSTs Substrate 1 - Sampling

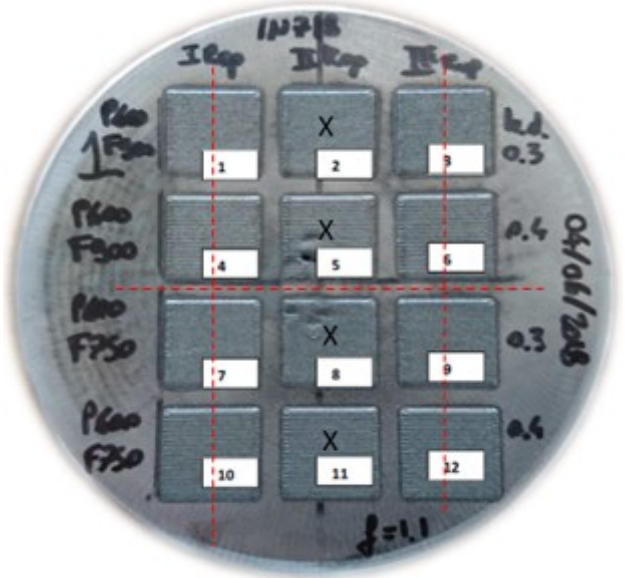


Figure 4.6: Layers Substrate 1 - Sampling

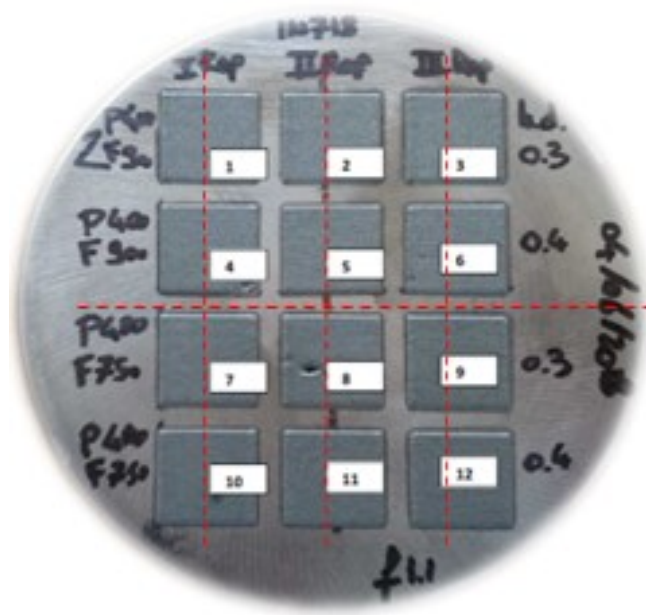


Figure 4.7: Layers Substrate 2 – Sampling

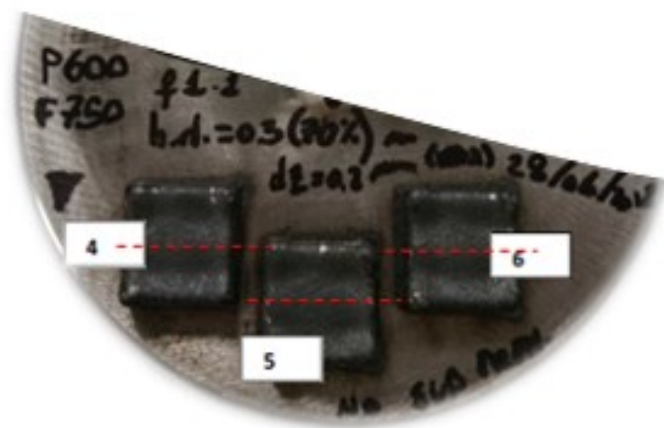


Figure 4.8: Bulks 4, 5 and 6 - Sampling

4.5 Mounting

After the cutting operations, the twelve SSTs samples have been then embedded in epoxydic resin made curing within plastic moulds for around 30 minutes Figure 65. This procedure resulted indeed necessary in order to make more accessible and more accurate the further polishing procedures so enabling to keep the cross-section surface parallel to the rotating card/pad. Thanks to a larger area in contact with the abrasive unit, it has been possible to ensure a more robust and reliable coupling between the two corps constituting the tribosystem limiting the samples oscillation and their good grabbing from the operator.



Figure 4.9: Plastic mould containing a curing epoxydic resin embedding the SSTs specimens

Otherwise from the SSTs, the Layers and the Bulks samples have been not “mounted” as just discussed above, since owing to enough adjunctive areas surrounding the feature’s cross-section, ensuring a compliant handleability of the sample in polishing.

4.6 Polishing

The polishing operations have been run employing a Presi Mecatech 234 polishing machine reaching a final Ra value of around 1 μm .

More in detail, this target roughness has been reached employing a set of abrasive cards respectively of #FEPA:

- 300
- 600
- 800
- 1200
- 2000
- 2400

Moreover, two pads bearing a mixture of diamond particles of 3 and 1 μm in an average size and a lubricant solution alcohol-based.



Figure 4.10: Presi Mecatech 234

More precisely, the samples have been polished changing their orientation at $\pm 90^\circ$ (respect to the polishing tangential direction) each time a different abrasive power polishing card has been changed. This shrewdness allowed indeed to attach the samples's superficial peaks more effectively.

Otherwise, the samples have been rotated from the same angle range aforementioned while they have been polished with the pads at 3 and 1 μm in order to achieve a more isotropic and homogeneous surface.

Finally, between each polishing step, the surface of the sample has been cleaned with soap and water with the intent to remove eventual debris or residual diamond particles as well, still leaning on the surface.

Moreover, as adjunctive cleaning step, the samples have been drowned in a beaker containing ethanol absolute and placed in an ultrasonic bath for around 3-5 minutes.

In Figure 67 are reported the SSTs cross-sections as polished at 1 μm observed with a LEICA DMI 5000 optical microscope at 50X.

IN 718 – Optical microscope – DED 50x – Scale Bar 100 μm

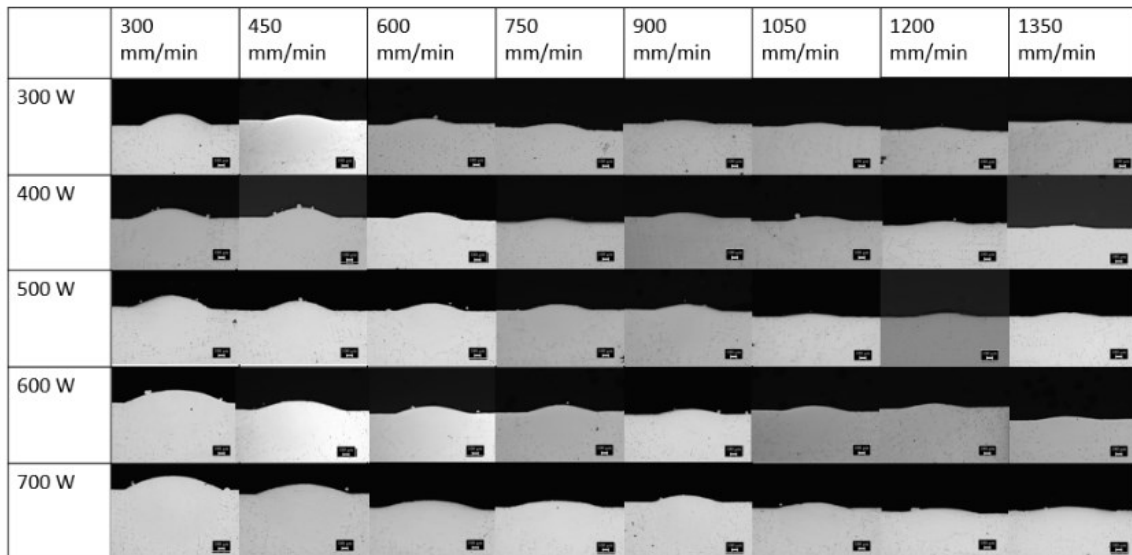


Figure 4.11: SSTs cross-section polished at 1 μm - Optical microscope

4.7 Chemical etching

After the samples surface check regarding the absence of superficial scratches due to the eventual non-compliant polishing, the same has been chemically etched with the metallographic etchant Kalling's No.2 whose composition is reported as it follows:

- CuCl_2 10 gr
- Hydrochloric acid 200 ml
- Ethanol absolute 200 ml

More specifically the samples have been drowned for around 15-17 seconds in the Kalling's No.2 solution and quenched in distilled water before being cleaned with soap and water and then dried with compressed airflow.

Furthermore, in order to remove eventual undesired halos as a consequence of a not optimal etching, the samples have been successfully cleaned with ethanol absolute before their observation at the Optical microscope.

4.8 Optical Microscope

Employing a LEICA DMI 5000 the SSTs, the Layers and the Cubes' cross-sections, have been analysed respectively in their etched and as polished surfaces at 50X and 100X.



Figure 4.12: LEICA DMI 5000 Optical Microscope.

4.9 SEM

Thanks to the SEM equipment "Phenom XL" endowed of an RX detector, it has been possible analysing the Cubes cross-sections observing the microstructure as well as detecting the phases present through a surface compositional analysis.



Figure 4.13: SEM equipment "Phenom XL."

5. Results and Discussion

5.1 Purposes

The intent of this experimental campaign is to identify the optimal process parameters dedicated to perform manufacturing and remanufacturing operations of IN718 components by DED.

Pursuing this goal, some basic features have been at first deposited on IN718 substrates which can also be intended as the bulk material of the component to be repaired. The features in object (detailed as follows), have been realized by “SUPSI” on respectively three different IN718 alloy, using not preheated substrates.

Features analyzed in “as-deposited” conditions:

- 40 IN718 Single Scan Tracks (SSTs) with no repetition.
- 20 Single Layers (SLs) with no repetition in their deposition parameters.
- Three Cubes (Blks or Cbs) built with the best process parameters.

Successively, the samples (as reported in Chapter 3) have been prepared for the characterization process, on which the several features have been analyzed from different perspectives aiming to verify their coherence with the substrate and their compliancy with functional applications.

5.1.1 Features specifications and themes of analysis

The SSTs have been realized employing:

- 8 Feed rate levels, F [mm/min]: 300, 450, 600, 750, 900, 1050, 1200, 1350
- 5 Laser Power levels, P [W]: 300, 400, 500, 600, 700

and characterized in:

- Tracks morphology and regularity
- Heat Affected Zone (HAZ) width
- Melt Pool morphology and regularity after etching
- Coherence with the substrate

Having collected and critically assessed the results obtained, some specific sets of process parameters have been recognized as appointed to generally provide an optimal deposition*. Successively, having identified the best process areas, the deposition compliancy issue has been then reported to a larger scale analyzing different depositions of Layers and Cubes.

**At this purpose, it must be noted that the results successively reported have not the intention to validate a depositional compliancy relatively to all the applicative cases. In fact, as mentioned in Chapter 2, the part thermal history it is not only related to the process parameters set but rather, to a vaster number of variables as for instance the part's shape, the powder chemical composition and the process environment.*

The SLs of Substrate 1 have been realized employing:

- A unique Laser Power level, P [W]: 600
- 2 Feed rate levels, F [mm/min]: 750, 900
- 2 Hatching distance, H [mm]: 0,3, 0,4

and that of the Substrate 2 adopting:

- A unique Laser Power level, P [W]: 400

- 2 Feed rate levels, F [mm/min]: 750, 900
- 2 Hatching distance, H [mm]: 0,3, 0,4.

Furthermore, the SLs of both substrates have been characterized in:

- Regularity
- Porosity/Oxides percentage area
- Etched morphology

The 3D Bulks analyzed have been realized employing:

- A unique Laser Power level, P [W]: 750
- A unique Feed rate level, F [mm/min]: 900
- A unique Hatching distance H [mm]: 0,3
- Layer thickness dz [mm]: 0,2
- Hatching Raster strategy: 0° /90° /45° /135° /60° /120°

and characterized in:

- Porosity/Oxides percentage area
- Microstructure
- Laves phases percentage area

Finally, an overview of the results obtained has been reported pertinently to some summary maps and a process software simulation of a simple feature has been attempt.

5.2 Single Scan Tracks characterization



Figure 5.1: SSTs-Substrate 1

Table 8: Exposure parameters and SSTs indexing.

LASER POWER [W]	FEED RATE [mm/min]							
	300	450	600	750	900	1050	1200	1350
300	9	10	11	12	13	14	15	16
400	25	26	27	28	29	30	31	32
500	17	18	19	20	21	22	23	24
600	1	2	3	4	5	6	7	8
700	33	34	35	36	37	38	39	40

5.2.1 Single Scan Tracks morphology

To analyze the as-deposited SSTs morphology, an “On Top” inspection at a magnification of 10X has been performed by a LEICA EZ4W stereomicroscope.

Focusing the SSTs at 10X, it has been possible to consider enough large shot of the features considered, which enclosed all the relevant hallmarks and the eventual deposition defects on which base the further morphology compliance evaluations.

Each featured image has been then collected in Figure 5.2 pertinently to the process parameters employed with which they have been realized and classified accordingly a stable or not stable deposition. This first distinction had the intent to distinguish eventual uncompliant tracks which presented unacceptable defectology of deposition, such as lacks of deposition, therefore considered as evidence of not reliable process parameters set.

	Laser Power				
	300 W	400 W	500 W	600 W	700 W
300 (mm/min)					
450 (mm/min)					
600 (mm/min)					
750 (mm/min)					
900 (mm/min)					
1050 (mm/min)					
1200 (mm/min)					
1350 (mm/min)					

Figure 5.2 SSTs “On top” analysis: red outline whether homogeneous deposition, red outline whether inhomogeneous deposition and blue outline labelling process instabilities

More in detail, all the SSTs depositions have been deemed stable except for the SSTs 21 (P 500W and F 900 mm/min) and 25 (P 400W and F 300 mm/min) as highlighted in Figure 5.2 (blue outline).

However, it is necessary to specify that no evaluations about the depositions repeatability can be provided pertinently to this campaign since the same have been uniquely realized. Therefore, the possibility to obtain compliant results at the same process parameters, cannot be neglected in further evaluations.

The defectology detected in SST 21 (Figure 5.3) could be likely caused by an equipment instability (like a sudden deposition head acceleration) or by a shutter time in which the deposition head has been not properly fed. However, to properly validate this theory, it would be suggestable to repeat the deposition for a larger number of times properly setting the equipment, so verifying whether the defectology occurs again or not.

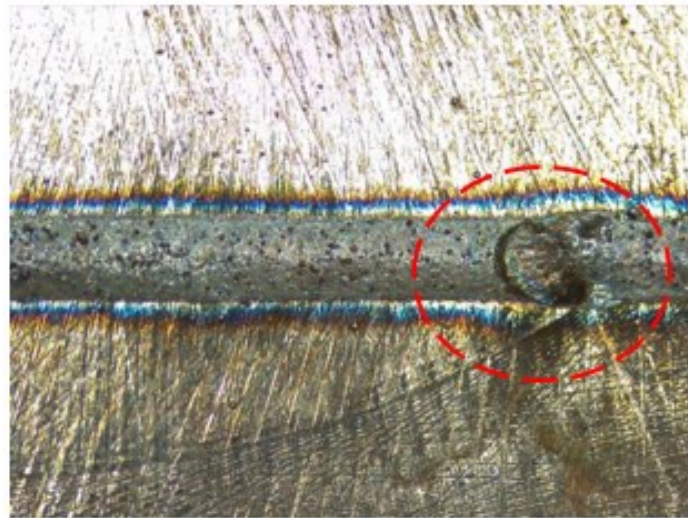


Figure 5.3: Process instability - SST n° 21.

Another defectology representative of an unstable deposition has also been detected in SST 25 (Figure 5.4). Likely due to the modest transverse speed and the low laser power level employed, it can be assumed that in this instance the resulting specific energy was not high enough to accomplish a right material melting (see section 1.1.5.2.1.2). As a result, the deposition obtained exhibits an evident discontinuity in its middle with an apparent lack of material. Since the energy source used resulted to be insufficient to homogeneously melt the mass of the particle fluxed, the track's profile moreover consistently deviates from a straight path, thus suggesting a not uniform/stable dynamic melt pool generation during the deposition.

Finally, it can be added that the rounded protuberances observable on the SST's profiles, could be likely due to a weak wettability of the melt pools which cannot properly joint together creating smooth edges because of the values of the parameters set.

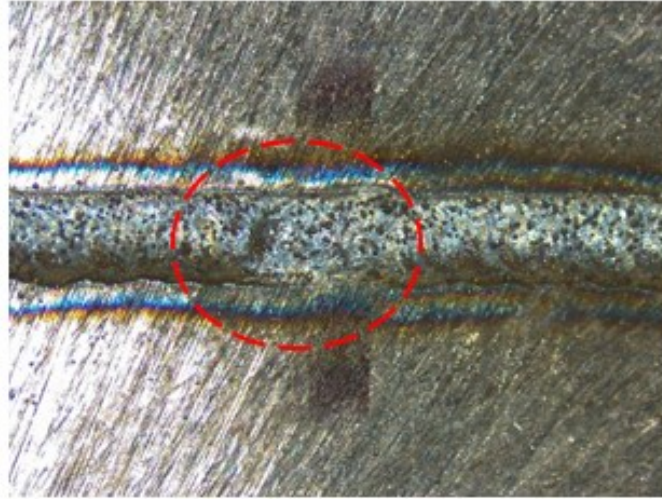


Figure 5.4: Process instability - SST 25.

Furthermore, the present analysis has been deepened (excluding the two just analyzed tracks) evaluating the SSTs deposition profile regularity or irregularity, considering the eventual linearity deviation of the edges.

According to that, each SST has been assessed in its morphology appearance and labelled with either a green or a red outline, whether the deposition was considered compliant or not-compliant according to an obvious criterion of homogeneity Figure 5.2.

The outcomes obtained, revealed that setting the equipment at low scan speed F and medium-high laser power P , the interaction between the deposited material and the substrate is remarkably severe. Therefore, this phenomenon entails an inhomogeneous deposition besides a pronounced HAZ. This latter feature will be successively analyzed separately.

Specifically, three SSTs (four considering also the not stable 25th deposition) out of five deposited at scan speed of 300 mm/min and at laser power of 500W, 600W and 700W respectively, resulted to be not-regular. In addition, also the SSTs 2 (450mm/min, 600W), 3 (600mm/min, 600W), 34 (450mm/min, 700W) and 35 (600mm/min, 700W) resulted not compliant Figure 5.2. As a result, a not compliancy process zone has been detected, therefore the coupling of the respective process parameters creating it have been deemed as not optimal to perform reliable repairing features.

5.2.2 SSTs and Heat Affected Zone (HAZ) regularity

The first analysis run wanting to deepen the interaction between the as-deposited material and the substrate; took into consideration the Heat Affected Zone as appeared on the substrate surface. Because of its importance in terms of supply material adhesion and coherency with the substrate, this parameter has been so considered as a key feature on which furtherly assess the tracks compliancy. Therefore, so that were possible to measure the HAZ width, further images of the SSTs, considering have been acquired at a magnification of 12,5X. More in detail, considering a precautionary approach, for each feature have been considered the images which included the larger number of defects and irregularities. The HAZ width has been then sampled and measured, by means of the software “ImageJ”, five times at the two magnification of 10X and 12,5X for a total amount of ten measurements for each SST. With the data obtained (reported in table 9), they have been calculated the *Arithmetic Mean* “A” and the *Standard*

Deviation “SD”, then plotted in their trends pertinently to the laser power and Feed rate levels from which they derived (Figure 5.5).

Table 9: HAZ “A” and “SD” values at different Laser Power and Feed Rate levels.

Laser Power vs Feed Rate	Laser Power P [W]									
	300		400		500		600		700	
Feed Rate F [mm/min]	A [μm]	SD	A [μm]	SD	A [μm]	SD	A [μm]	SD	A [μm]	SD
300	216	16.9	303.5	40	433.1	39	353.5	33.8	628.4	104
450	218.5	43.9	221.8	57.9	341	80	279.8	19.4	459.5	55.7
600	200	21.2	236.6	39.1	253.3	50	326.6	32.5	246.2	50.2
750	138.6	17.3	163.3	27.3	180	41.9	308.2	25.6	310.2	40.3
900	117.8	28.5	218.2	56.2	194.2	62.9	244	40.8	335.7	67.8
1050	98.8	28.9	192.7	36.5	141.3	28.2	210.9	27.8	251.2	28.4
1200	76.4	8.6	95.4	23.8	144	30.4	197.2	33.4	201.5	28.8
1350	56.4	16.4	76.4	25.4	149.8	42.3	199.5	28.2	169.5	36.2

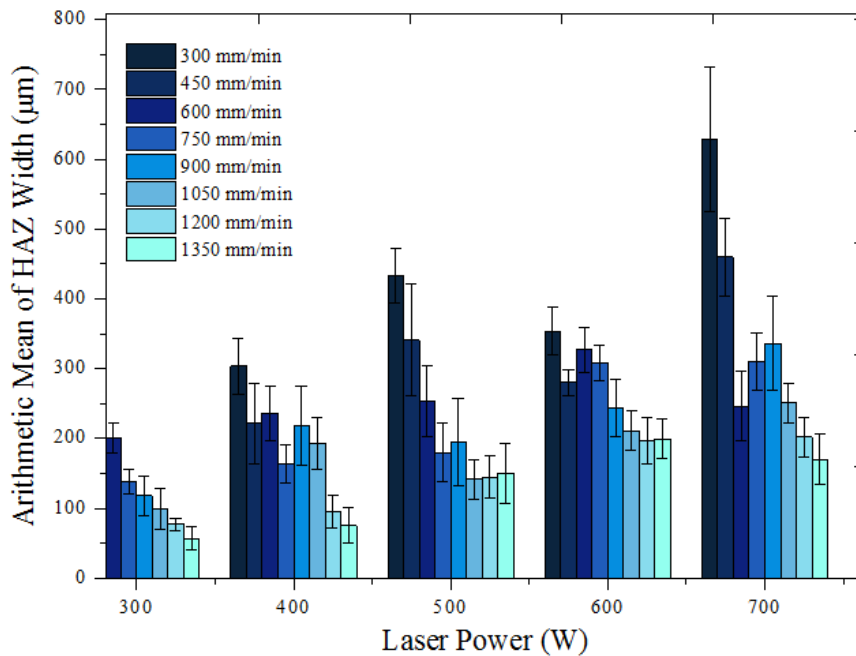


Figure 5.5- Figure 63 (shadowed): HAZ Arithmetic Mean “A” and Standard deviation “SD” as a function of Laser Power and Feed rate levels – representative SST in which the HAZ Width has been displayed.

In the overall, the HAZ Arithmetic Mean width decreases at parity of laser power level as the feed rate and the scan speed increase. This phenomenon finds moreover confirmation in the literature, according to which increasing the scan velocity at parity of laser power value, the specific energy provided to the substrate on unit of area, decreases (see section 2.6.2.2.2, Equation 2.1). Therefore, in the case in point the interaction with the substrate is less severe and then the interface thickness in which the two phases institute an equilibrium boundary.

However, in Figure 5.3 can be noticed some incongruences with this theory. In particular the SSTs “28” (P 400 W, F 750 mm/min), “20” (P 500 W, F 750 mm/min), “2” (P 600 W, F 450 mm/min) and “35” (P 700 W, F 600 mm/min) shown HAZ widths respectively higher than that of the SSTs deposited at the same P level but at a lower F value. Furthermore, each “A” value bar, has been coupled with an error bar representing the respective SST’s Standard deviation. Unlikely from the Arithmetic Mean, it has been not possible to highlight a common trend for the SD values. In fact, the SD floatability seems to be unpredictable since, is moreover directly susceptible to defectology (lack of fusions, balling and so on) which locally alter the HAZ width, aside from a great variety of process parameters and eventual setbacks of equipment instability. According to the results just reported, the HAZ Standard deviation has been considered an essential parameter on which base the HAZ and hence the deposition regularity assessment.

However, was not possible to establish a threshold value on which base a compliancy assessment by exclusion. Therefore, from the data collected was only possible to recognize the general dependency of the HAZ’s width values with the laser power and the feed rate levels. More precisely, it was possible to find that a direct relationship between the laser power increase and the HAZ’s width rising exists. Furthermore, it was possible to state that the HAZ’s width decreases with the scan speed and the feed rates increment.

5.2.3 SSTs etched Melt Pools HAZ

Referring to the HAZ width discussion just started in the previous paragraph, it can be said that in order to assess to which extent the HAZ width can affect the SSTs deposition compliancy a cross sectional analysis results to be fundamental.

In fact, it was not possible to find in literature a specific values range which indicated a threshold distinguishing compliant or not deposition. Rather, the HAZ evaluations as in accordance with LI,Y et al., are generally made in relation to the liquid cracking phenomenon and to the hardness variation since the substrate, throughout the HAZ, to the deposition itself (Li, Chen and Tamura, 2018). Therefore, in order to verify the eventual liquid cracking occurring, the single SSTs have been etched and observed in their cross sections by means of an optical microscope at a magnification of 100X. From the analysis run, no presence of cracks within the Melt Pools has been detected, also in correspondence of the SSTs which exhibited the most pronounced HAZ. However, even though no liquid cracking phenomena have been detected (also at the most pronounced HAZs), it has been recognized that a too large interaction with the substrate in this sense, must be avoided. In fact, large HAZ widths values mean high areas overlaying the depositing layer metallurgically altered. As a consequence, bringing these considerations to a macroscale perspective, because of the layering approach, parts built with process parameters responsible of a pronounced HAZ show a remarkable microstructural inhomogeneity because of the repeated layers annealing. Moreover, the homogeneity and continuity issues take fundamental importance dealing with repairing operations where the substrate cannot be considered as expendable material since it is part of the functional

component. According to these considerations, an effective way with which quantify the HAZ width effect could be run hardness tests in order to verify the hardness variation between the substrate, the HAZ and the part. However, this last topic of analysis was not considered in this assignment.

5.2.4 SSTs etched Melt Pools Morphology

Similarly to the criterion employed in the morphologic Top view analysis, assessing the Melt Pools morphology, has been adopted a symmetry criterion.

This geometrical aspect, in its simplicity at first defines the effectiveness of the process parameters employed and whether deposition results uniformly coherent with the substrate along its dimensions. Otherwise, a lack of Melt Pool symmetry can prejudice the coherence leading to interposed porosities and lack of fusion between the further overlapped (and juxtaposed) tracks.

Therefore, according to the assumptions just made, a remarkable morphologic incompliance has been detected at the low Laser Power levels 300W and 400W. Respectively, the SSTs “10”, “11”, “12”, “13” and “26”, “27”, “28”, “29”, “30”, “31”, “32” exhibited an irregular Melt Pool profile due to the low Specific Energy used which resulted inefficient to properly melt the substrate in the unit of time dictated by the transverse speed.

The aforementioned SSTs have been so deemed non-compliant and outlined in red as reported in Table 10.

Table 20: SSTs etched Melt Pools - 50X optical microscope

	Laser power				
	300 W	400 W	500 W	600 W	700 W
300 mm/min					
450 mm/min					
600 mm/min					
750 mm/min					
900 mm/min					
1050 mm/min					
1200 mm/min					
1350 mm/min					

5.2.5 SSTs etched Melt Pools coherence with the substrate

Thanks to the different substrate and deposited material corrosion rates, it has been possible to accurately recognize the Melt Pool's main features: "Bead Height", "Melt Pool Width" and "Fusion Depth" (Figure 5.6). Therefore, the etched Melt Pools images (reported in table 11), have been acquired at a magnitude of 50X and the features measured by the software ImageJ. From the data collected (Table 12), it is possible to state that the "Bead Height's" steadily decreases as the feed rate value increases at fixed P (Figure 5.10). In addition, a remarkable "Melt Pool's Width" and "Fusion Depth's" growth has been recorded when the Laser Power is incremented at constant Feed rate (Figure 5.5 and 5.10). These three general trends, respectively as a consequence of an upgraded transverse speed at parity of specific energy and, for both the latter, of an increased energy supply at constant feed rate, find moreover confirmation in literature as reported in section 2.6.2.2.1 However, so that were possible to better understand the relationship between the three main parameters in the case in point, they have been furtherly discussed and cross-referenced as follows.

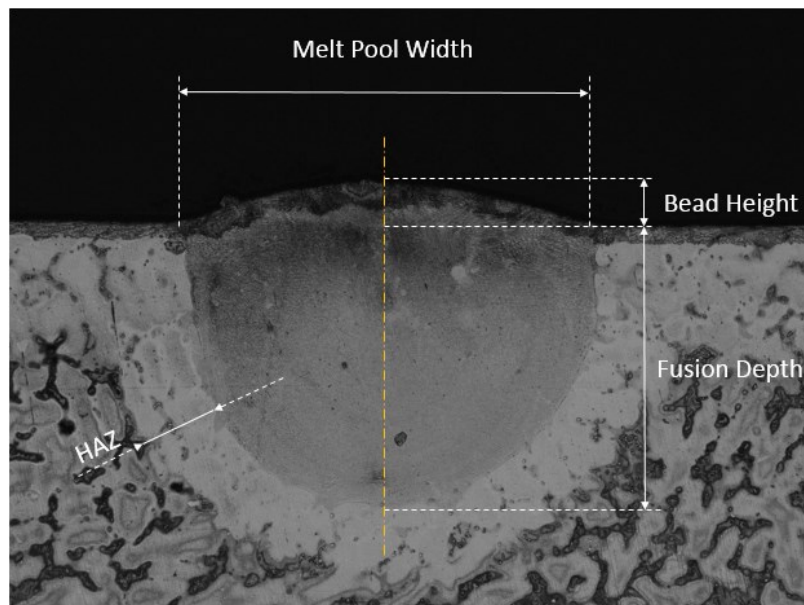


Figure 5.6: SST "37" and its main features: Melt Pool Width, Bead Height, Fusion Depth and HAZ

5.2.5.1 Melt Pool's Width, Fusion depth and Bead height

Generally, the melt pool's width increases with the laser power rising (Figure 5.7), however some deviations from this general trend have been found at the SSTs: SSTs "33" (300mm/min, 700W), "37" (900mm/min, 700W), "8" (1350mm/min, 600W) and "23" (1200mm/min, 500W). These show a melt pool's width respectively lower than that of the melt pools obtained adopting the same feed rate and a lower laser power. At this purpose, in order to investigate the reason of the just described discrepancies, the 33rd and the 1st (300mm/min, 600W) tracks have been selected as representative example seeing their evident non-compliance with this general theory. The two SSTs reported in Figure 5.7, have been obtained employing the same feed rate (300mm/min) value but different laser power respectively of 700W and 600W, respectively for the SST 33 (on the left) and for the SST 1 (on the right). As the quotes report, the latter own a higher melt pool's width than the former of around 80 μ m (even though created with a more

modest P). On the other hand, the SST 33 exhibits a more pronounced Fusion Depth zone, deeper than that of the counterpart for more than 200 μm due to a higher P adopted as expected from the general trend reported in Figure 5.10. Nevertheless, the same melt pool's morphologic traits of the example presented of an unexpected low melt pool's width in favor of a remarkably high Fusion depth, have been also recognized in the SSTs 33, 37 and 23. This counterintuitive observation find explanation from a thermodynamic perspective, in the heat transfer modes rising within the Dynamic Melt Pool during the deposition. As reported in section 3.1.2, the heat generated within the molten material is transferred to the substrate and towards the outside world, by a conductive and a convective manner. Comparing the two phenomena relevancy, it can be said that seeing the remarkably high molten material speed flow, the convective heat transfer mode is definitely the prominent one. Therefore, since the heat flow states the solidification direction hence, the 3D melt pool's shape (section 3.1.2, 3.1.3, 3.2), it is possible to assume that in the SST 33, the convective flow had a predominant z-axis component because of the high P level and the modest feed rate. As a consequence of the "directional" high specific energy used, the melt pool so resulted with a deep Fusion depth (surrounded by an evident HAZ as mark of a too severe depositional interaction with the substrate) rose more respect to the melt pool's width. Nevertheless, this trend is confirmed by the experimental data reported in Figure 5.11 according to which at parity of feed rate levels the ratio between melt pool's width and fusion depth decreases for increased laser power values. Furthermore, the ratio just mentioned it represents the first key parameter on which base the melt pool's geometric homogeneity. More in detail, at the ideal ratio "Width/Fusion depth" value of "1", the melt pool's geometry results to be rounded shape with a good melt pool's penetration within the substrate. From the data collected it appears also clear that this benchmark valued can be pursued increasing the laser power (Figure 5.11). However, the experimental data reported, show a not sufficient decreasing of the aforementioned ratio (pertinently to the laser power raising) to achieve the ideal melt pools' shape. At this purpose, it was recognized that the balance between the feed rate and the laser power levels employed was not optimized. As a matter of fact, the low feed rate used entailed to a too severe laser interaction with the substrate that created deep and acicular melt pools. More specifically, it can be said that the specific energy supplied by the equipment, was so mainly appointed to melt the substrate, rather than the supplied material.

Otherwise, in SST 1 have been found more proportionate features dimensions respect to the previous case. However, also in this instance a not optimized set of process parameters has been found because of the still existing eccentricity of the melt pool. This issue is likely imputable to a laser power slightly meagre and not able to provide the right balance between fusion depth and melt pool's width. To conclude, as a result of the comparisons made and from the data displayed in Table 10, it is reasonable to think that wanting to keep the same melt pool's width in SST 33 pursuing a compliant and uniform deposition, it would be suggestable to increase the feed rate value so lowering the severe laser interaction with the substrate. On the other hand, in order to optimize the "1st" deposition at parity of F, it would be recommendable to slightly increase the laser power up to an intermediate value between 600W and 700W.

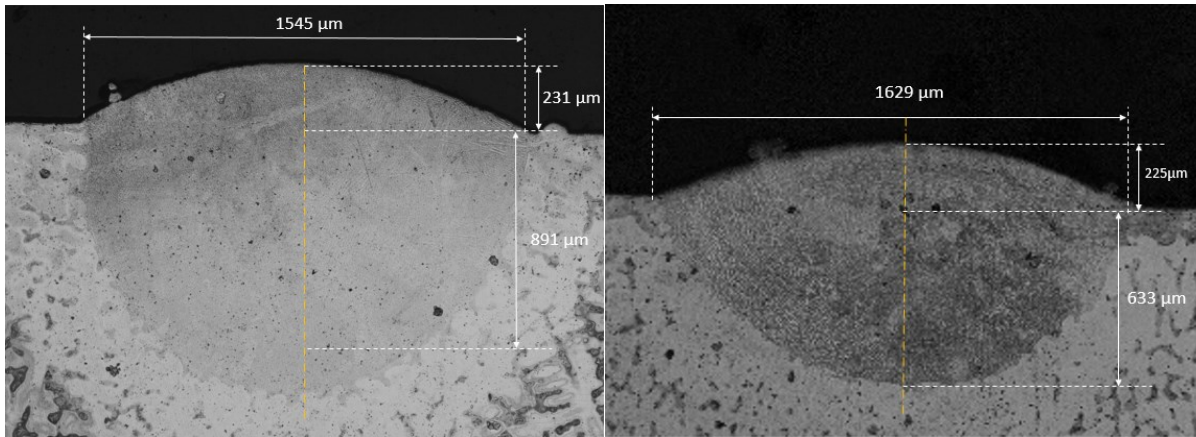


Figure 5.7: Etched melt pools of the SSTs 33 (on the left) and 1 (on the right) respectively indexed in their main feature dimensions.

About the Fusion Depth analysis, a further unexpected result has been recorded. The SST 21 (900mm/min, 500W) shows at parity of feed rate a fusion depth sensitively higher than that obtained for the 5th SST (900mm/min, 600W) even though at the same time this latter has a larger melt pool's width. Therefore, in this case the second trend just previously discussed seems to be reversed suggesting a width growth at first, instead of the fusion depth, as a consequence of the P increased. However, this particular deposition it has been intended as not reliable at first, since the "On top" analysis revealed a remarkable defectology besides a high HAZ SD, so witnesses of a not stable deposition.

For the avoidance of doubt, the specimens sampling has been double checked and also the SST second half has been polished and then etched (Figure 5.8). The result has been still unvaried.

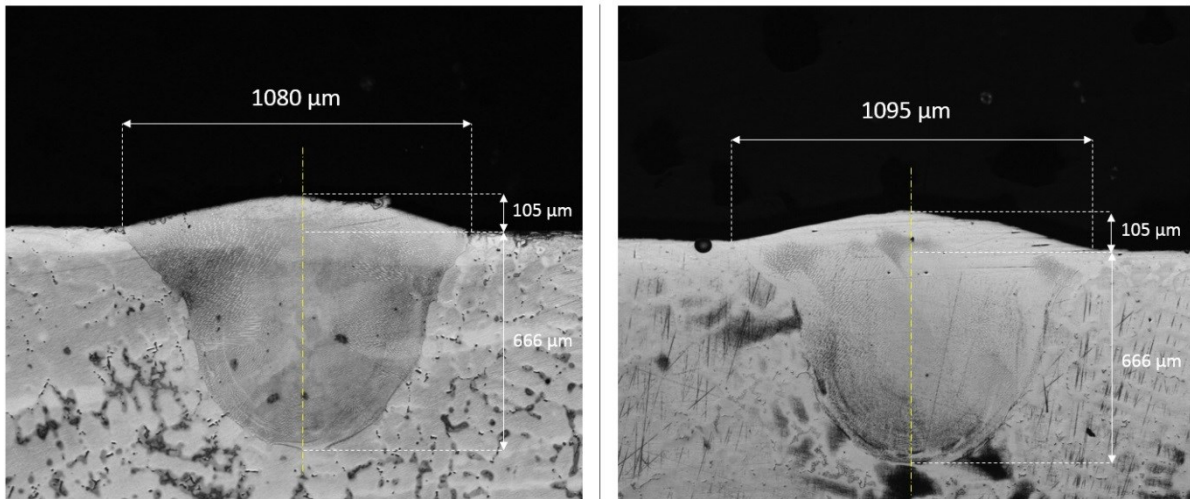


Figure 5.8: 21th SST etched Melt Pool and its not compliant Fusion Depth

About the Bead height, the measurements performed show a general increase of this feature when the laser power rises at a constant feeding rate (Figure 5.10). Furthermore, the whether the feed rate increases at parity of laser power the Bead height decreases. As reported in Equation 2.2 of section 2.6.2.2.2, the Powder density is defined as the ratio between the flow rate G (intended as mass of particles fluxed in the unit of time [g/min]) and the spot size (d)

times the transverse speed v . Furthermore, as reported in the experimental equation 2.4 of section 2.6.2.2.2, the powder density directly affects the layer thickness (t) which increases or decreases according to the powder density trend. Therefore, it can be said that in general the layer thickness decreases according to the scan speed growth.

In Figure 5.12 is reported the “Width/Bead Height” ratio in dependence on the laser power and the feed rate levels. More in detail, when this ratio tends to “one” the bead height results to be perfectly balanced with the melt pool’s width exhibiting compliancy geometrical properties appointed to obtain a good side and transversal overlapping between the tracks. However, from the data collected in this experimental campaign it is noticeable that also at the lower scan speed considered, the bead height shows very modest values, hence, low layer thickness. As reported in Figure 5.12 also at the lowest scan speed value (300 mm/min), the bead height/width ratio is about “5”, so suggesting a remarkable deviancy from the ideal value. Therefore, it was noticed that probably the fixed feed rate value employed to supply the deposition head was to modest for the laser power levels employed so entailing to a not compliant layer thickness and melt pools geometry.

Finally, it can also be stated that according to the experimental data acquired in this campaign, all the three main melt pool’s features diminish in their dimensions increasing the transverse speed at a constant laser power.

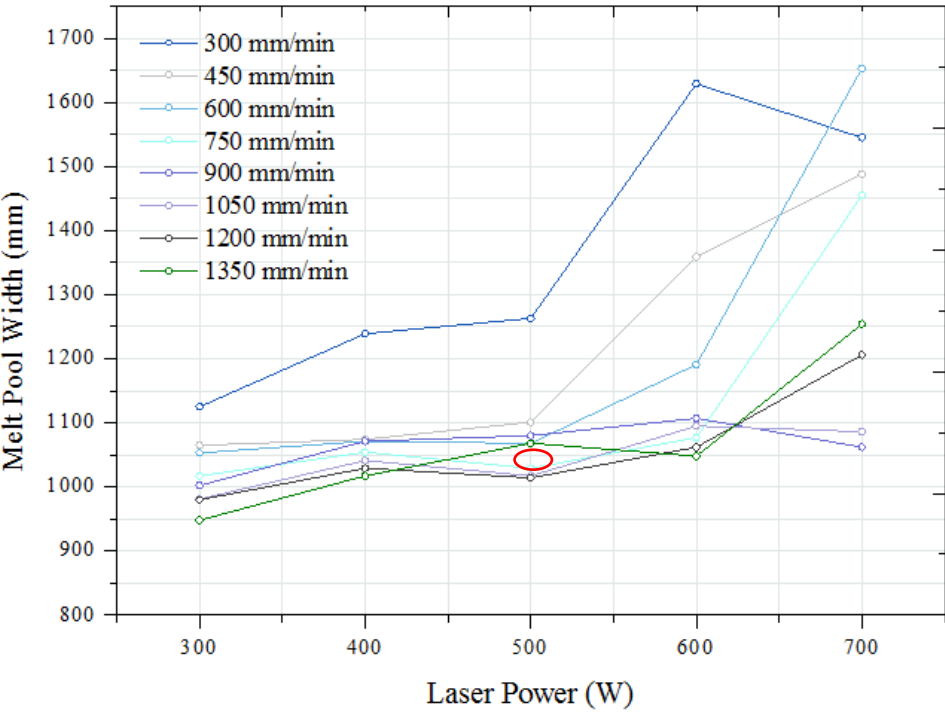


Figure 5.9: SSTs Melt Pool width as a function of the Laser Power – red outline (process instability)

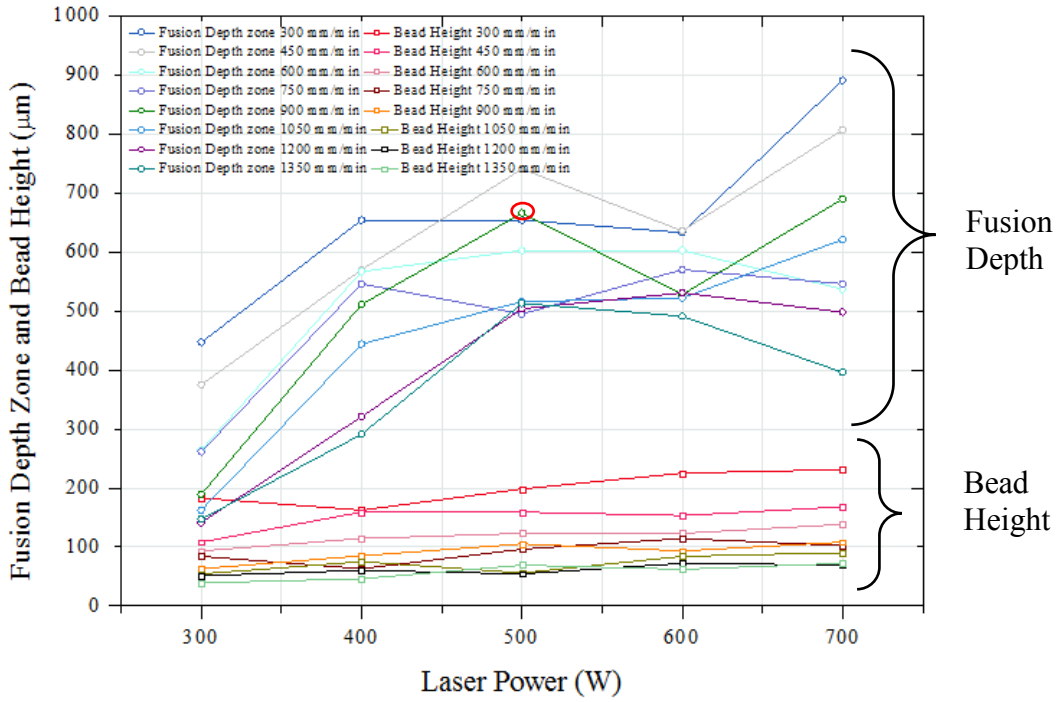


Figure 5.10: SSTs Fusion Depth and Bead Height as a function of the Laser Power – red outline (process instability)

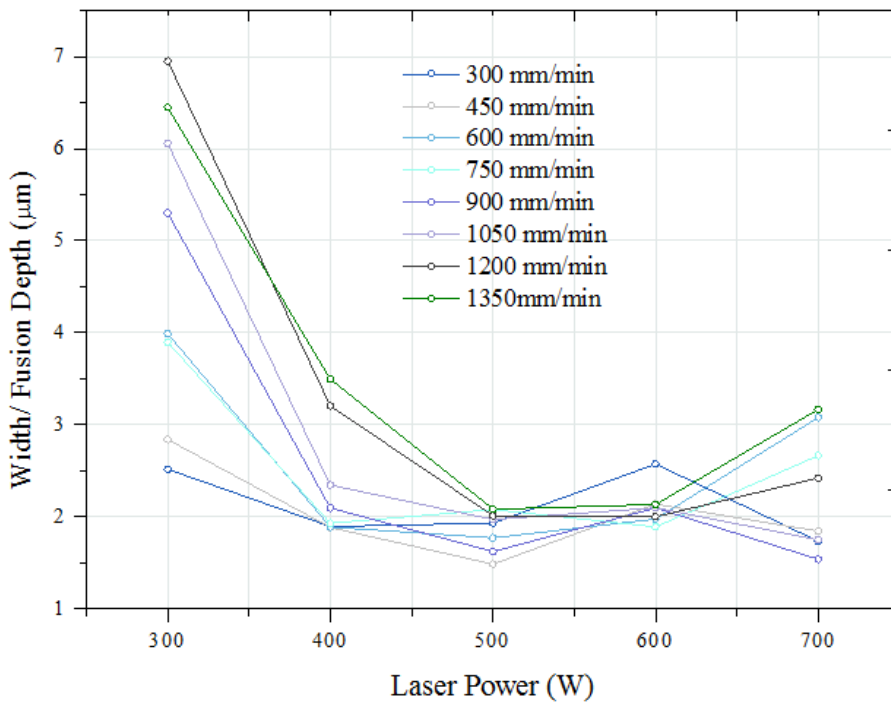


Figure 5.11: SSTs Melt Pool width and Fusion Depth ratio as a function of the Laser Power

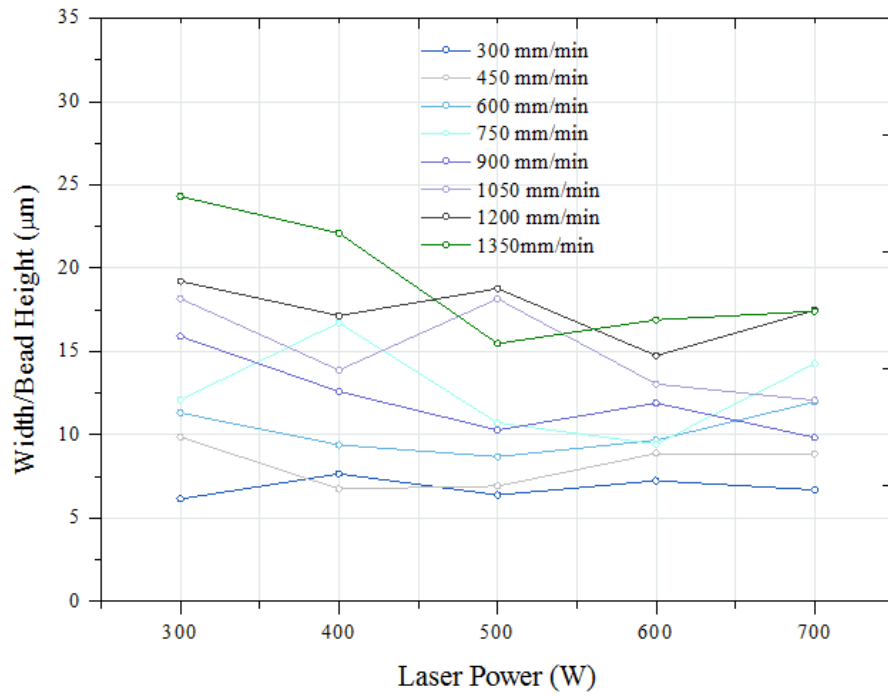


Figure 5.12: SSTs Melt Pool width and Bead Height ratio as a function of the Laser Power.

Table 11: Melt Pool Width, Fusion Depth and Bead Height measurements at different Laser Power and Feed Rate values

Laser Power [W]	Feed Rate [mm/min]	Melt pool width [μm]	Fusion Depth [μm]	Bead Height [μm]
300	300	1125	447	183
	450	1065	375	108
	600	1053	264	93
	750	1017	261	84
	900	1002	189	63
	1050	981	162	54
	1200	980	141	51
	1350	948	147	39
400	300	1239	654	162
	450	1074	570	159
	600	1071	567	114
	750	1054	546	63
	900	1070	511	85
	1050	1041	444	75
	1200	1029	321	60
	1350	1017	291	46
500	300	1263	656	198
	450	1101	741	159
	600	1068	603	123
	750	1029	495	96
	900	1080	666	105
	1050	1017	516	56
	1200	1014	504	54
	1350	1068	513	69
600	300	1629	633	225
	450	1359	636	153
	600	1191	603	123
	750	1077	570	114
	900	1107	528	93
	1050	1095	522	84
	1200	1062	531	72
	1350	1048	491	62
700	300	1545	891	231
	450	1488	807	168
	600	1653	537	138
	750	1455	546	102
	900	1062	690	108
	1050	1086	621	90
	1200	1206	498	69
	1350	1254	396	72

5.2.6 SST n° 37 - etched Melt Pool's SEM/EDS analysis

Figure 5.13 is reported an SEM image of the 37th SST acquired at 310x, representing the field of analysis on which an EDS analysis has been run with the intent to identify the phases present in the aforementioned feature.

For this purpose, in the next paragraphs the main phases detected will be listed and briefly detailed pertinently to the results provided by the EDS analysis run, in terms of chemical composition and XRD peaks recorded.

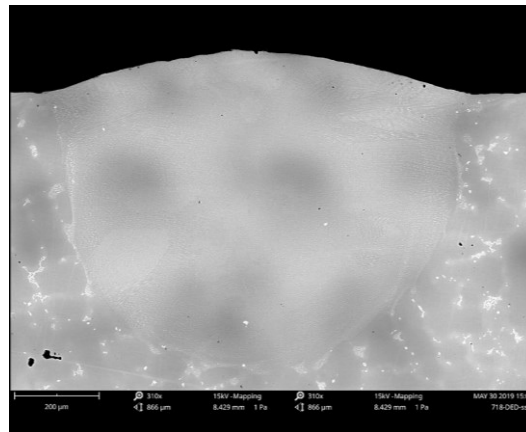


Figure 5.13: SST's 37 Melt Pool image acquired at 310x by SEM

(Nb/Cr based Carbide)

In Figure 5.14 is reported a Nb/Cr carbide-based, dispersed within the γ matrix, analyzed in its chemical composition found by an EDS analysis as reported in Table 12.

However, referring to the alloying elements mentioned in paragraph 2.8.4 and to the carbide types reported in Table 6, it is reasonable to think that seeing the relevant presence of Nb and Cr, the carbide in object can be respectively related to either a MC / M_6C , or to the $M_7C_3 / M_{23}C_6$ species depending on whether the Nb or Cr local content is prominent.

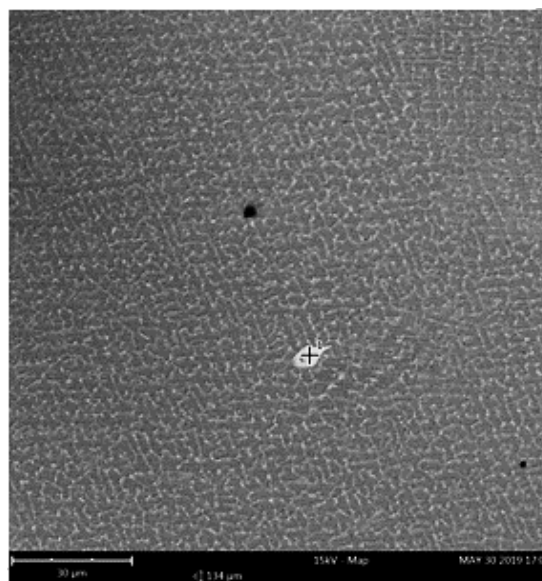


Figure 5.14: Nb/Cr based carbide detected within the 37th SST Melt Pool

Table 12: Nb/Cr based carbide chemical composition

Element	Atomic concentration	Weight concentration
Nickel	46.13	43.96
Chromium	17.60	14.86
Iron	16.22	14.71
Niobium	13.44	20.28
Molybdenum	2.31	3.60
Titanium	2.03	1.58
Aluminum	1.32	0.58
Silicon	0.95	0.43

(Nb/Ti based Carbide)

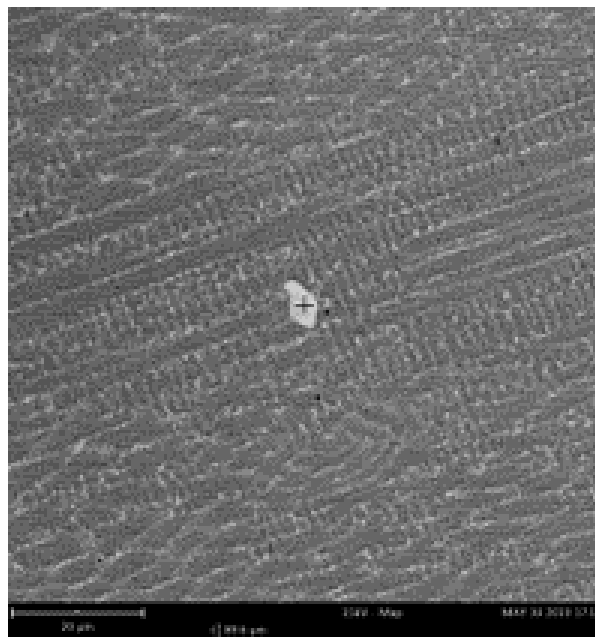


Figure 5.15: Nb/Ti based carbide detected within the 37th SST Melt Pool

Element	Atomic concentration	Weight concentration
Niobium	75.06	84.38
Titanium	14.92	8.64
Nickel	3.85	2.73
Molybdenum	1.77	2.06
Silicon	1.65	0.56
Chromium	1.41	0.89
Iron	0.86	0.58
Aluminum	0.47	0.15

5.3 Layers characterization



Figure 5.16: a) Layer Substrate 1 and b) Substrate 2 (on the right)

Table 13: Exposure parameters and Layers indexing.

Laser Power P (W)	Feed rate F (mm/min)											
	750						900					
	Hatching distance Hd (mm)											
	0,3			0,4			0,3			0,4		
Sub 1 600	7	8	9	10	11	12	1	2	3	4	5	6
Sub 2 400	7	8	9	10	11	12	1	2	3	4	5	6

5.3.1 Substrate 2 – Inclusions

The Layers features embedded in Substrate 2 have been realised employing the same process parameters used to deposit the SSTs 28 and 29. More in detail, the Layers 1-6 have been built with the same P and F levels with which the SST 28 has been deposited. Also, the Layers 7-12 have been built with the same process parameters used to realise the SST 29.

Analysing the results provided in the sections 5.2.2, 5.2.3 and 5.2.4, are pertinent to the two features just mentioned, several aspects of depositional non-compliance can be highlighted.

The SST no. 28 (750mm/min, 400W) even though presents a regular deposition, seeing its HAZ's standard deviation lower than the 30% and its HAZ width inferior to 200 μ m, it reports a remarkable melt pool asymmetry (Figures 5.17).

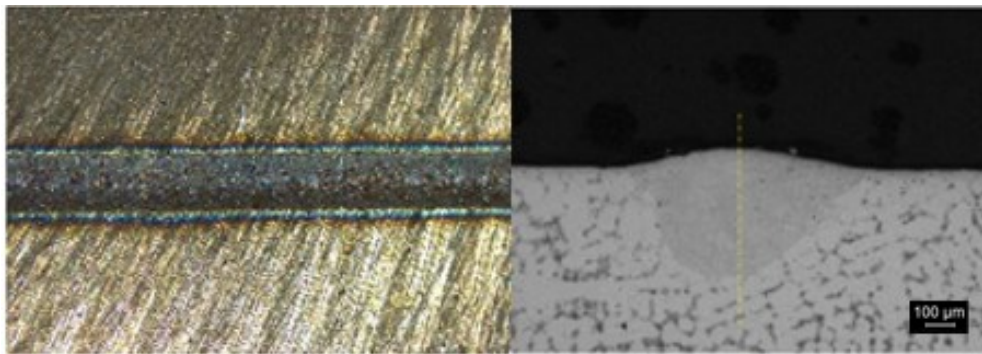


Figure 5.17: SST 28: regular deposition on the left and not symmetric Melt Pool on the right

Furthermore, a Melt Pool asymmetry has been detected also in the SST no. 29 (900mm/min,400W): deposition considered as non-optimal because of its HAZ width value, and its HAZ standard deviation (Figure 5.18).

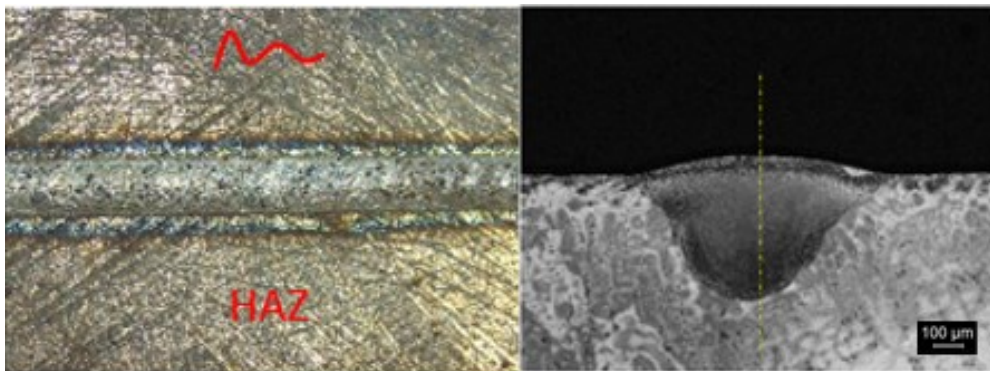


Figure 5.18: SST 29: irregular deposition on the left and not symmetric Melt Pool on the right.

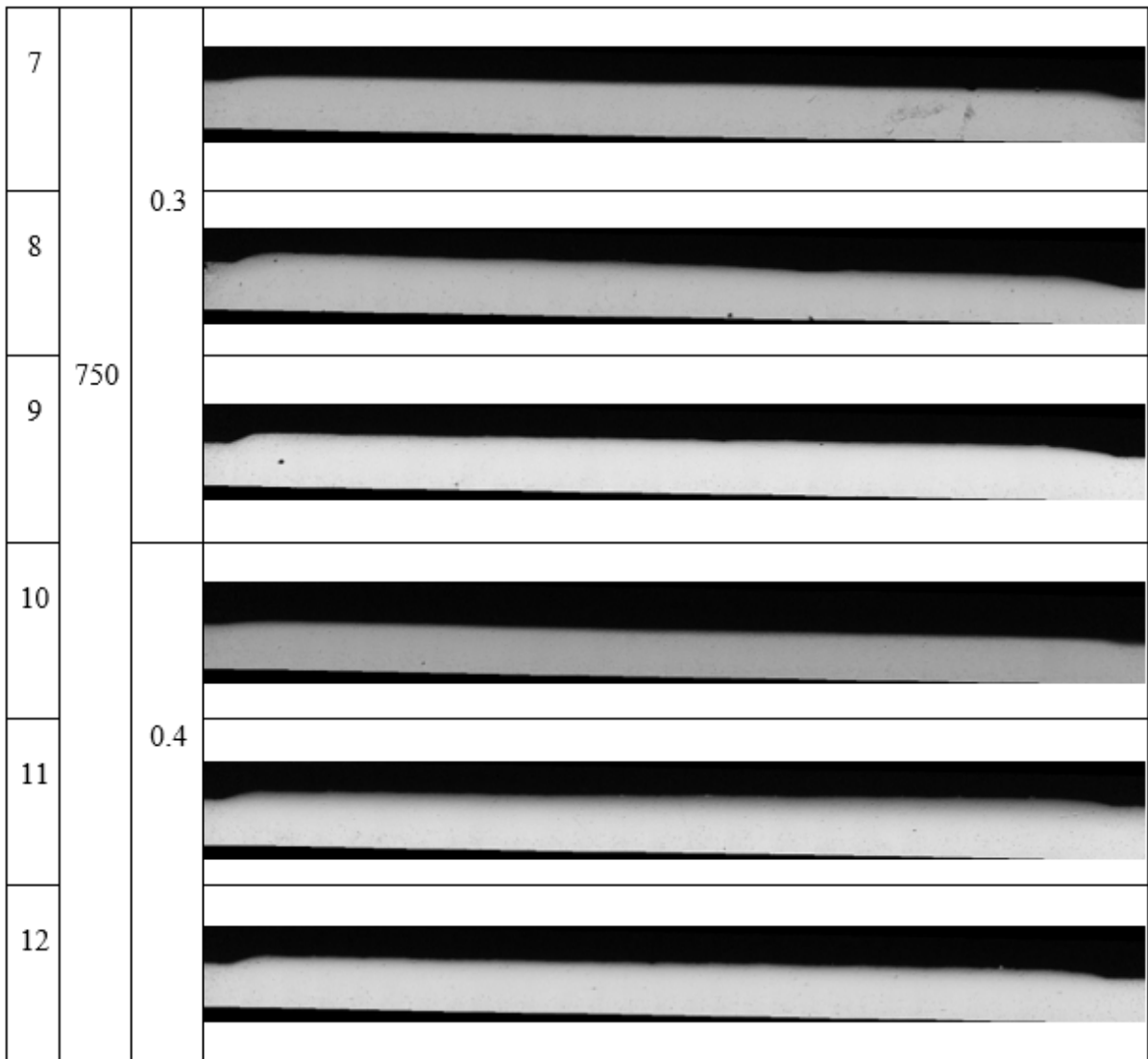
However, it has been recognised in the adoption of the “modest” laser power 400W an advantage in terms of energy consumption. Therefore, the Substrate's two layers have been analysed in order to verify whether a proper side overlapping of the SSTs could be obtained despite the melt pools' geometrical irregularity.

Therefore, with the intent to verify whether a tradeoff between the melt pools asymmetry and an appropriate hatching distance selection would have led to a compliant deposition, it has been run an optical analysis to assess the morphology and regularity of the etched layers as detailed in the section 5.3.2.

Furthermore, in order to verify the feasibility of the repairing operations in relation to the process parameters in object, the specimens obtained at two different hatching distances (of 0,3 and 0,4mm), have been optically observed in their cross-sections and analyzed pertinently to the eventual presence of defects or inclusions as well (Table 17). Further specifications at this purpose are provided in section 5.3.1.1 and 5.3.1.2.

Table 14: Substrate 2 Layers as polished at 1μm and photographed at 50X utilizing an Optical microscope.

L (n °)	F (mm/m in)	h.d. (m m)	
1	900	0.3	
2			
3			
4		0.4	
5			
6			



In general, two types of defects can be revealed the cross-section of IN718 alloy; porosity and oxides. However, these two different types of defects can be not quantitatively distinguished one from each other, but instead, they can be counted as a unique feature in consequence of optical analysis. However, it should be noticed that according to the literature, the presence of their defects together is very detrimental for the final performance of the alloy.

Ultimately, a qualitative analysis of the oxides has been carried out in the SSTs and Cubes EDS sections, in conjunction with their compositional specification.

5.3.1.1 Inclusions Percentage area

Each layer has been photographed around 24 times along its length and their most critical areas in terms of residual defects, have been analysed employing the “ImageJ” software thresholding the defects from the background considering a minimum detection size of 2 μm and a minimum circularity of 0,5.

According to the experimental data obtained, the most relevant defect content has been detected at the lower feed rate value of 750mm/min where the defect appears more than doubled respect

to that characterising the 1-6 layers. More, in particular, the higher percentage area of inclusions/pores has been recorded for the hatching distance value of 0,3mm at F=750mm/min, the 0,4 instead (Figure 5.19).

On the other hand, referring to the F level of 900 mm/min, this latter trend results to be reversed since the highest area percentage has been recorded at Hd of 0,4 mm, 0,3 mm instead. The highest A% at Hd 0,3 (repetition 1) does not overcome the lowest A% value at Hd 0,4 found in repetition number 5 (Figure 5.19).

5.3.1.2 Inclusions Average size

For what concerns the defect’s average size, the differences observed relative to the measurements performed on the Layers 1-6 and 7-12 cross-sections, are not substantial. However, at F 900mm/min, it is possible to recognise a slightly higher average size respect to that recordable in layers 7-12.

Besides, the data displayed suggest a progressive decrease in defects’ dimensions towards successive repetitions at a constant feed rate, and the most important, towards higher hatching distances (Figure 5.20).

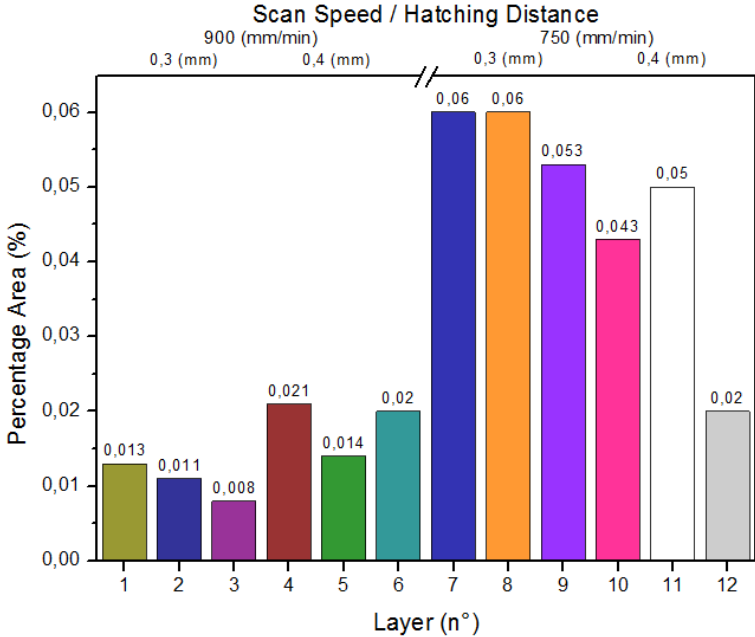


Figure 5.19: Defects Percentage area as a function of the Hatching distance and Feed rate

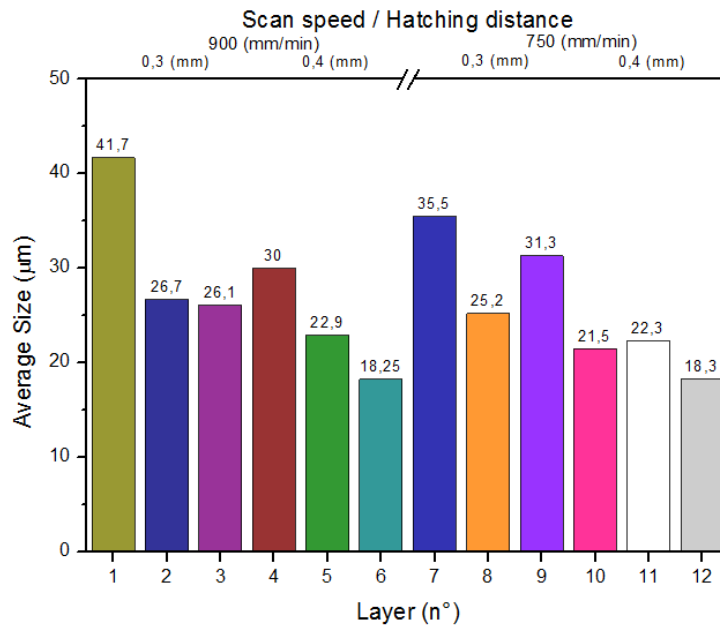


Figure 5.20: Inclusions Average size as a function of the Hatching distance and the Feed rate

5.3.1.3 Inclusions discussion

According to T. DebRoy et al., three main phenomena can lead to porosity formation (Zhang et al., 2017):

- Keyhole
- Gas induced porosity
- Process induced porosity

However, from the optical analysis run at 50X and 100X, no Keyhole formation has been detected. Probably due to the relatively low laser energy density levels adopted in this campaign, none formation of irregular porosities as a consequence of the material evaporation has been noticed.

Furthermore, analysing the single etched layers as reported in Table 16, at the boundary zone between the melt pool and the substrate, no lack of fusions or voids have been observed as well. On the other hand, as reported in Figure 5.17, some small circular voids spread out the layers cross-sections can probably represent pores generated to the carrier gas entrapment.

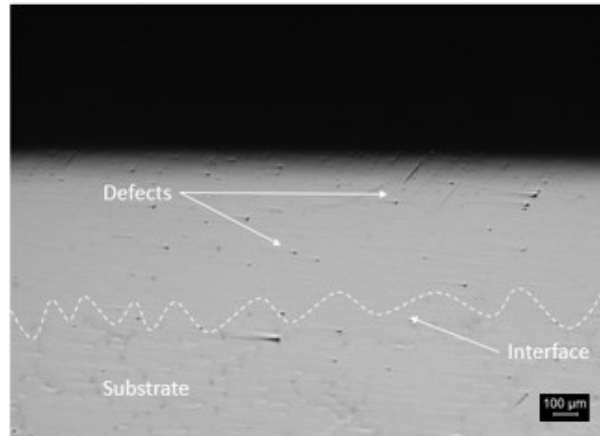


Figure 5.21: Layer 7 (750mm/min, 400W, Hd of 0,3mm) cross-section – defects detected at 50X through an optical microscope.

Also, it can be noticed that the presence of porosity found within the sample could be due to the already existent porosity present in the feedstock powder particles. A possible pores genesis within the part built can find the explanation in the transferred free volume from the melting particles to the melt pool.

Therefore, this theory finds a solid base in the SEM analysis of the feedstock particles run by 4DHybrid, which reports evidence of (not yet quantified) porosity inside the gas atomised particles (Figure 5.22).

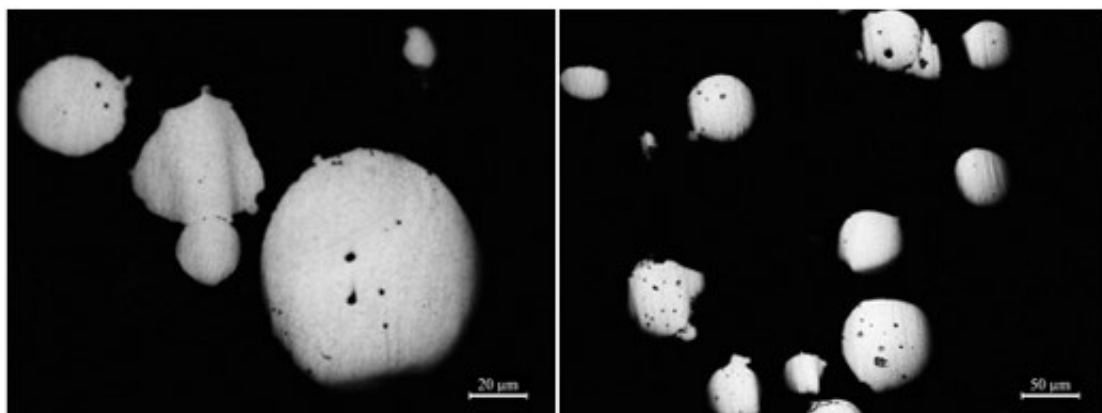


Figure 5.22: the cross-section of the starting powder used in this work.

However, as already stated, it is not possible to quantify the porosity content with respect to that of the oxides since the two species promiscuity and the optical inspection nature.

At this purpose, indeed, an EDS analysis would be more effective in order to precisely identify the oxides and their composition even though the quantification uncertainty would persist.

Furthermore, it has to be also recognised that even though it was possible to quantify the porosity percentage area, this last datum would be not so meaningful in terms of reliability. Seeing the local nature of the cross-sectional analysis run would be not possible to verify the results reliability relatively all the deposition dimensions.

At this purpose, would be more effective run a 3D pores distribution analysis with a tomographic approach (analysis method not adopted in this experimental work).

As already introduced, the presence of oxides has been detected. Investigating the causes that led to the formation of the oxide and embedding within the part, it has to be at first considered the non-adoption of shielding gas during the material deposition. In fact, due to this process choice, the environmental conditions have likely induced the formation of the oxide because of the interaction between the oxygen present in the deposition environment and the overheated depositing material.

Nevertheless, in the oxides' genesis, the impurities and the oxides pre-existing within the feedstock particles played an important role. In fact, according to the 4DHybrid EDS analysis the particles exhibit, in conjunction with satellites and partially melted particles on their surface (Figure 5.23), partially oxidised particles Al and O rich that can be embedded in the melt pools during the deposition (Figure 5.24).

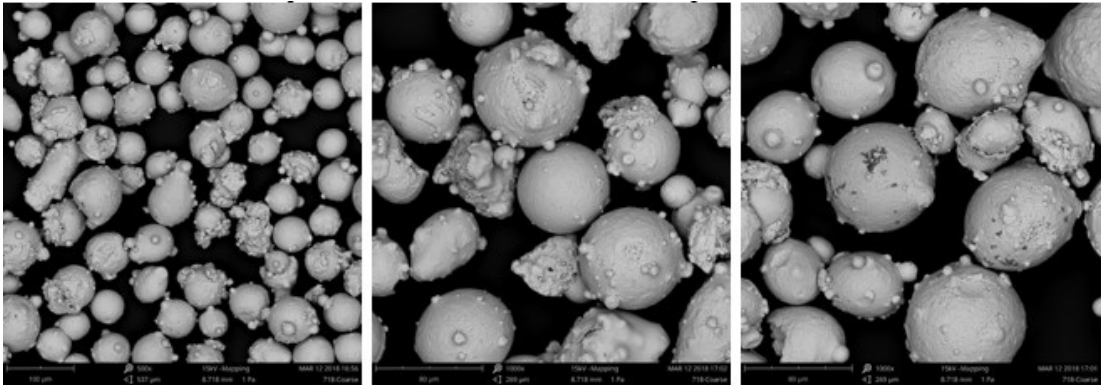


Figure 5.23: IN718 feedstock particles bearing satellites, partially melted particles and oxides on their surfaces – Coarse size distribution ranging between 44 and 106 µm.

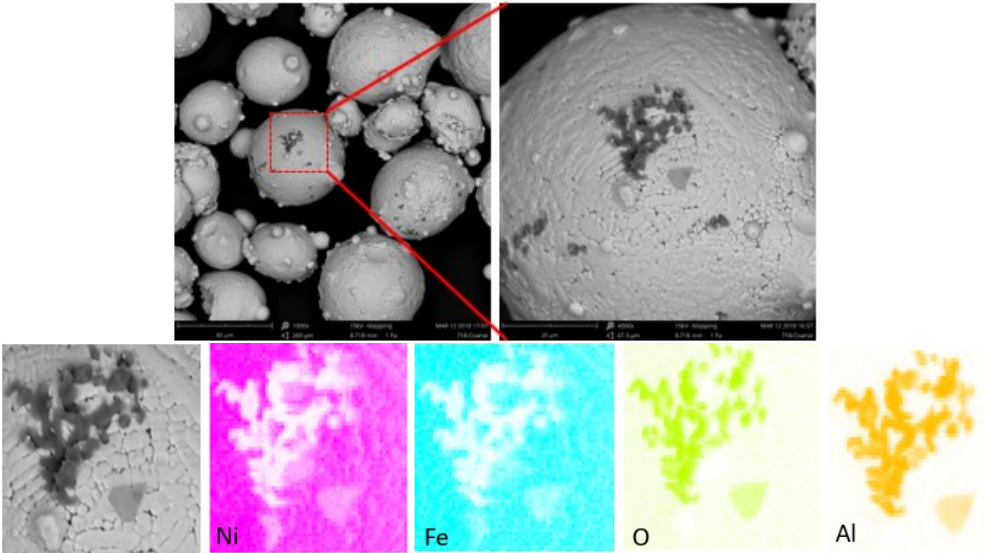


Figure 5.24: IN718 feedstock EDS analysis and chemical elements mapping

To conclude, the layers defects analysis revealed a miscellaneous presence of pores and oxides not directly distinguishable in terms of relative quantity.

Also, referring to these two types of defect the most probable causes have been recognised as deriving from equipment setbacks as carrier gas entrapment leading to circular pores or oxides generation because of the non-adoption of shielding gas flow rate.

For both of these defects, it has been moreover detected a direct influence of the feedstock particles composition and morphology seeing the spheres including of pores and oxides generated during their atomization process. Furthermore, the EDS analysis of the feedstock, suggests the presence of aluminium oxides even though further compositional details are left to the next Cubes' EDS analysis. The residual defects analysis showed that the level of this defect at 750 mm/min is higher than that recorded at 900 mm/min for the modest value of 0,06% whereas the maximum average size recorded in the first layer repetition is of 41,7 μm . Therefore, it can be concluded that independently from the relative quantity, the defect quantity and average size can be assessed as generally low.

5.3.2 Substrates 1 and 2 – etched layers morphology 98

Wanting to establish what set of process parameters entailed to the most homogeneous (and compliant for repairing) deposition, the layers of the substrates 1 and 2 were compared in their morphology.

At this purpose, the etched cross-sections (Tables 17 and 18) were optically analyzed at a magnification of 50X and 10X, noticing at what results of coherence with the substrate and depositional homogeneity led the respective melt pools features analyzed in section 5.2.5 (Table 15 and 16) and their morphological aspects (section 5.2.4), as a consequence of their overlapping.

Table 15: Melt Pool's main features dimensions obtained at P 400W and respectively F of 750 and 900 mm/min.

Laser Power P (W)	Feed rate F (mm/min)	Melt Pool's width (μm)	Fusion depth (μm)	Bead Height (μm)
400	750	1054	546	63
	900	1070	511	85

Table 16: Melt Pool's main features dimensions obtained at P 600W and respectively F of 750 and 900 mm/min.

Laser Power P (W)	Feed rate F (mm/min)	Melt Pool's width (μm)	Fusion depth (μm)	Bead Height (μm)
600	750	1077	570	114
	900	1107	528	93

Analysing the best layers repetitions obtained at 400W in comparison to that obtained at 600W at a constant feed rate and hatching distance, a substantial difference of coherence and homogeneity has been noticed in the overall. In fact, the depositions performed at 600W, show a better inter SSTs overlapping besides a higher fusion depth and coherence with the substrate. In order to demonstrate the superior compliancy of the Substrate's 1 depositions compared to that of the Substrate 2, it has been considered as representative example the comparison between the layers 9 (Sub. 2) and 6 (Sub. 1).

As reported in Table 14, the layer 9 of the Substrate 2 has been deposited with the lower values of Feed rate and hatching distance considered in the layers campaign. On the other hand, the layer 6 has been built adopting the higher scan speed and hatching distance with a 600W laser power level.

Therefore, since an increase in feed rate generally entails a lowering of the melt pool size, it can be said that the worst-case in terms of SSTs lateral overlapping it has been chosen referring to Substrate 1. On the other hand, the best condition to maximise the SSTs overlapping, hence low F and Hd, have been considered selecting the layer of comparison in Substrate 2.

As shown in Figure 5.25, even adopting a low scan speed and hatching distance, the melt pools overlapping result to be unstable and inhomogeneous along the layer's width. Even though the Melt Pools seem to be acceptably overlapped side to side, their relative fusion depth varies remarkably showing a not homogeneous coherence between the layer and the substrate.

Moreover, the micrograph revealed for the layer 6 of the substrate 1 shows a more stable and homogeneous deposition compared to that of its counterpart considered. Regardless of a significant hatching distance and scan speed adopted, the 6th deposition at 600W shows a very good SSTs overlapping besides a constant fusion depth.

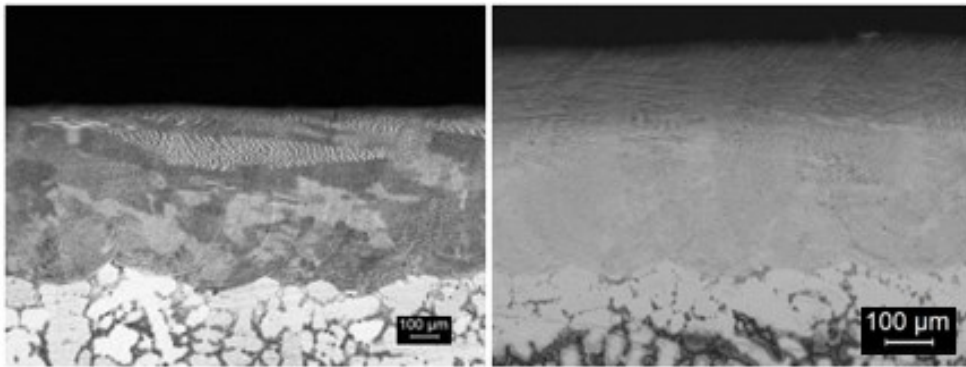


Figure 5.25: Micrograph of the etched layers a) 9 of the Substrate 2 and b) 6 of the Substrate 1 respectively acquired at 50X and 100X.

Therefore, according to the assumptions just made and seeing the results discussed in section 4.2.4 relatively to the SSTs morphologic compliancy, the 600W laser power level has been recognised to be as the optimal choice. Besides, the layers bead heights are in this case, sensitively higher than that achieved at 400W. Therefore, adopting the 600W as the laser power level is possible to increase the repairing rate at the expenses of lower dimensional accuracy.

Furthermore, in order to guarantee a higher deposition coherence and process stability, the hatching distance of 0,3 and the Feed rate of 750 mm/min has been selected as preferred. Although these latter choices entail a slight loss of process productivity, the advantages just mentioned have been considered prominent: mostly considering the assumed purposes to which the process is dedicated.

Table 17: Micrographs of the Substrate's 2 layers etched cross sections acquired at 50X (optical microscope)

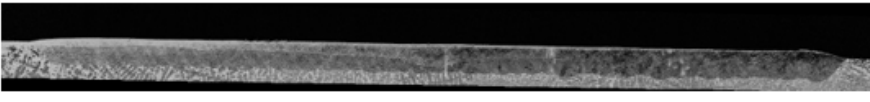
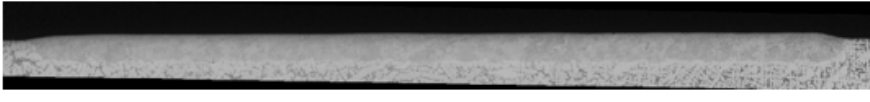
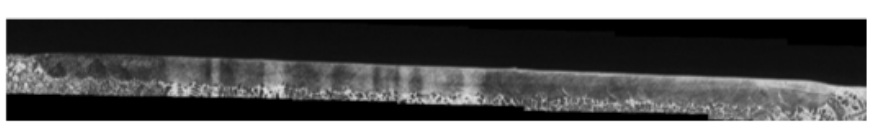
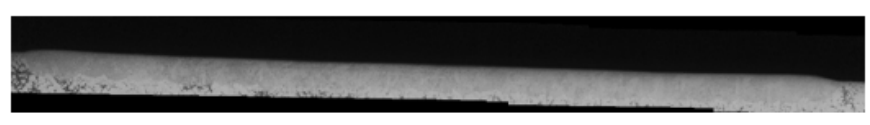
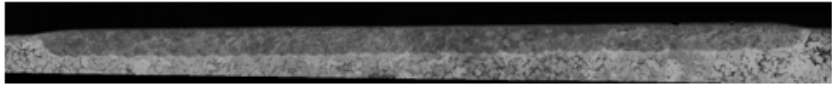
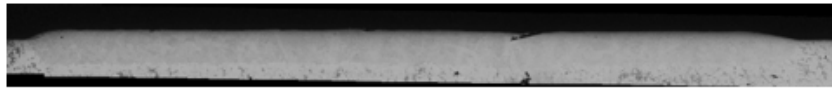
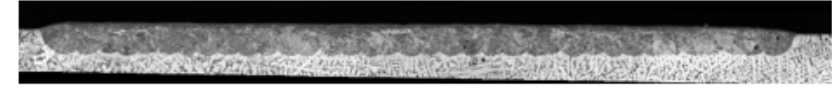
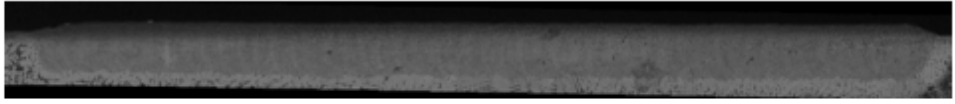
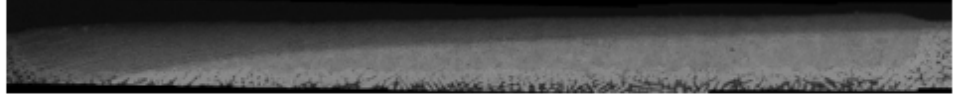
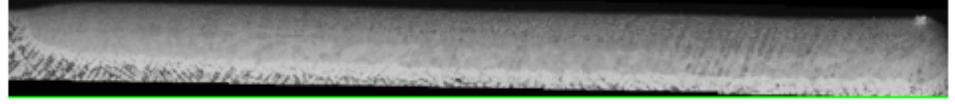
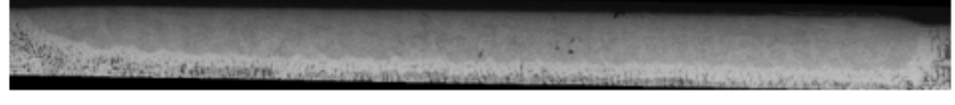
1	900	0.3	
2			
3			
4		0.4	
5			
6			
7	750	0.3	
8			
9			
10		0.4	
11			
12			

Table 18: Micrographs of the Substrate's 1 layers etched cross sections acquired at 100X (optical microscope)

L (n°)	F (mm/min)	h.d. (mm)		
1	900	0,3		
3				
4		0,4		
6				
7		750	0,3	
9				
10	750	0,4		
12				

5.4 Bulks/Cubes Characterization

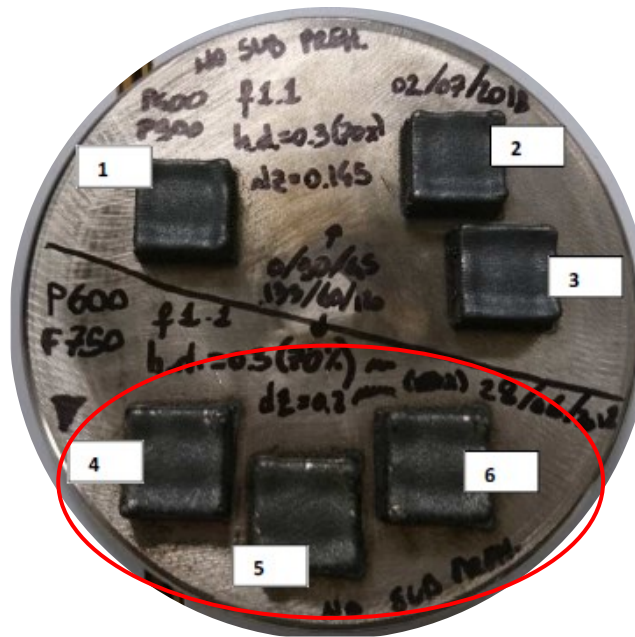


Figure 5.26: Unique Substrate – Bulks characterized: 4, 5 and 6

Table 19: Exposure parameters and Cubes indexing.

Laser Power P (W)	Feed rate F (mm/min)		
	750		
	Hatching distance Hd (mm)		
600	0,3		
	4	5	6

5.4.1 Defects analysis of the Cubes

Similar to the residual defect analysis in the SLs, an optical inspection concerning the Cubes have been run at 50X of magnification.

In fact, following the assumptions made at the end of section 5.3.1.3, it has been deemed noteworthy deepening the analysis of more large parts realised at the laser power level 600W and feed rate level 750 mm/min.

Although the limited potentialities of this inspection method were already evident, it has been anyway choosing to pursue this way in order to verify whether inclusions were present and to what extent generally. Furthermore, the feature's dimensions have also allowed verifying the eventual presence of defects, such as lack of fusion and keyholes, on a vaster scale than that granted from layers.

As reported in Figure 5.27 and 5.28, the maximum inclusions content and the average size detected was respectively of around 0,04% and 14,8 μ m. These latter are noticeably lower than that detected in the Substrate's 2 layers 7,8 and 9 obtained at a constant feed rate and Hatching distance but with a P of 400W. The reader is reminded of sections 5.3.1.1 and 5.3.1.2.

Although, it is prior stating that because of the respective different areas inspected the two results have not the same grade of accuracy and reliability, the mismatch in values induces to

think that the higher Laser Power level has contributed to lower the porosity percentage and size thanks to an enhanced Melt Pool wettability. However, in the analysis in point, this assumption has to be intended as indicative since the porosity morphology is not distinguishable from that of oxides.

Furthermore, also in this instance, no keyhole or lack of fusion phenomena were detected throughout the whole Bulks' cross-section.

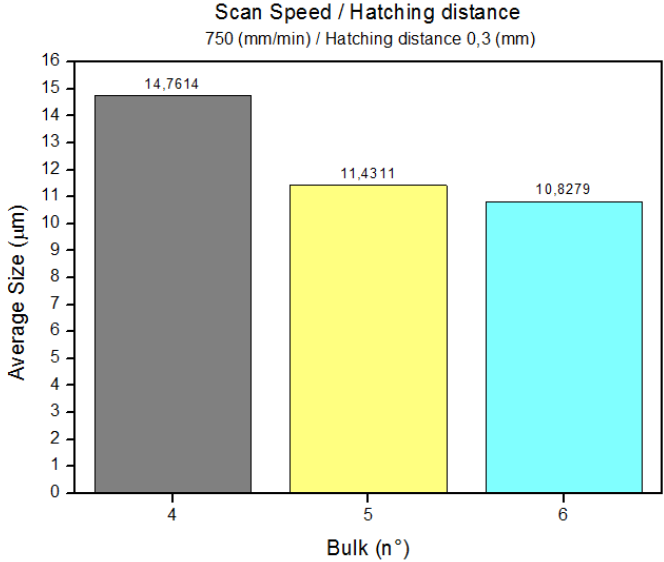


Figure 5.27: Inclusions average size analysis performed at 50X by means of an optical microscope

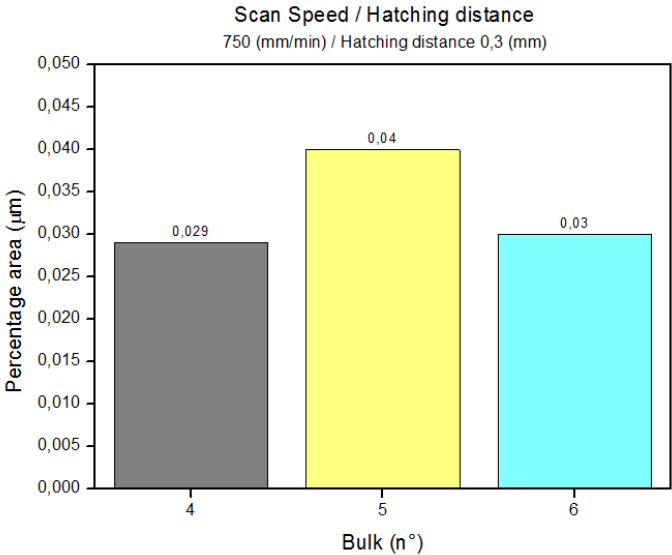


Figure 5.28: Inclusions percentage area analysis performed at 50X by means of an optical microscope

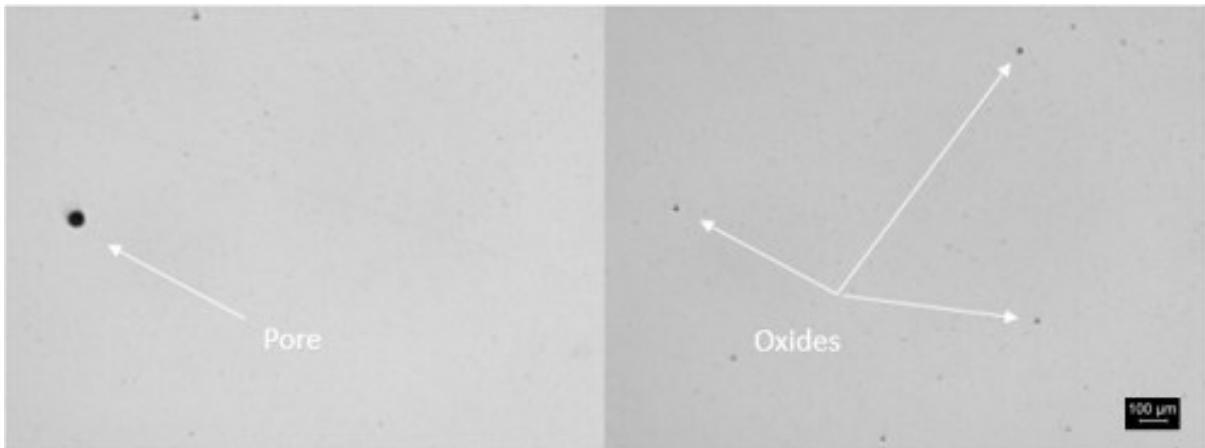


Figure 5.29: Pores and oxides inspected in the middle of Bulk 4 – Micrograph acquired at 50X

5.4.2 Optical analysis of the etched Cubes

After the defects evaluations, in order to study the microstructure of the cubes, the Kalling no.2 solution was used to chemically etched the cubes.

The following optical analysis has the intent to inspect the microstructure's morphology and recognise the main grains growth phenomena ascribable to the DED process.

Furthermore, with this method of inspection, it was possible to observe the microstructural transitions and anisotropy correlating them to particular areas of the three built (Figures 30, 31 and 32) such as the interface of substrate/deposited material, the build top/edges and core.

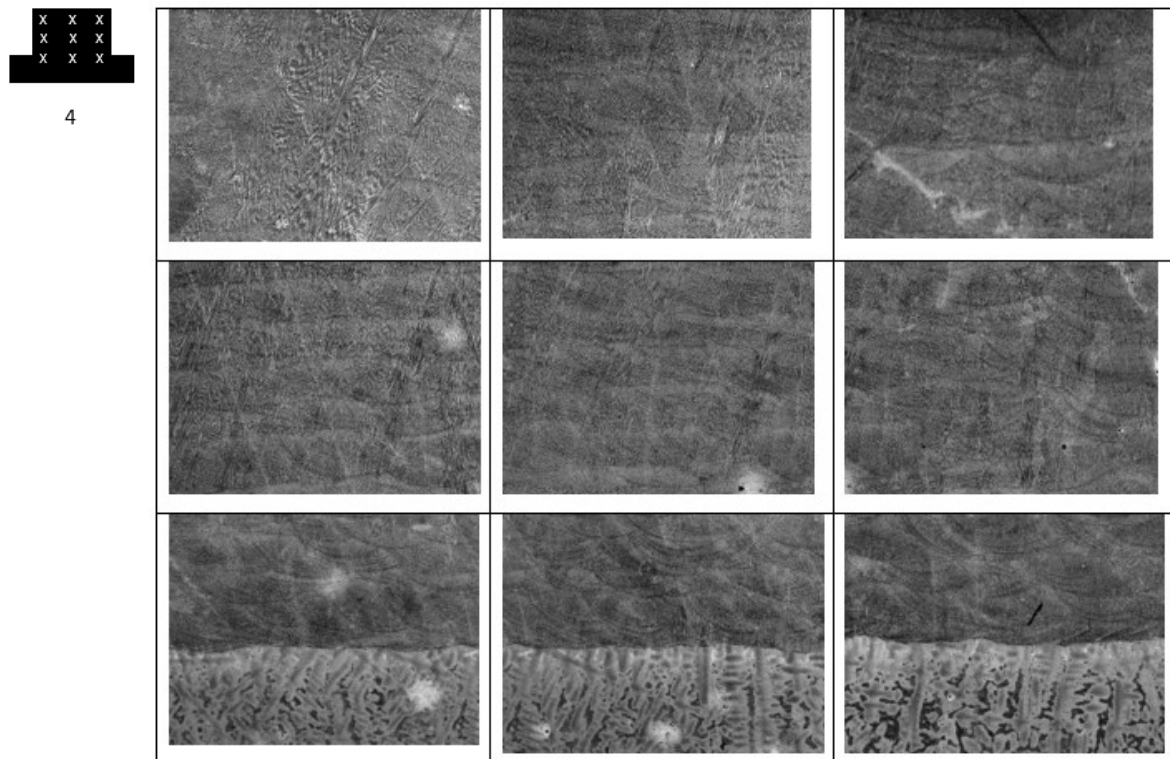


Figure 5.30: Etched Bulk 4 - Optical analysis performed at 50X

x x x
x x x
x x x

5

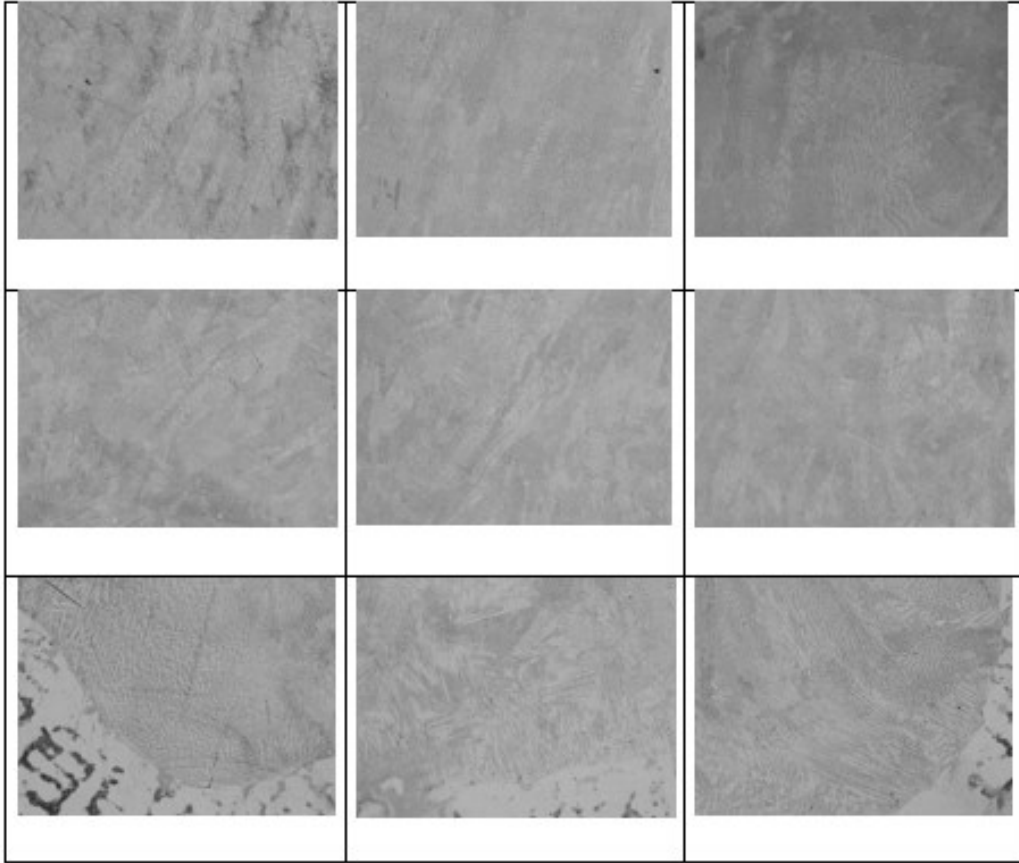


Figure 5.31: Etched Bulk 5 - Optical analysis performed at 50X

x x x
x x x
x x x

6

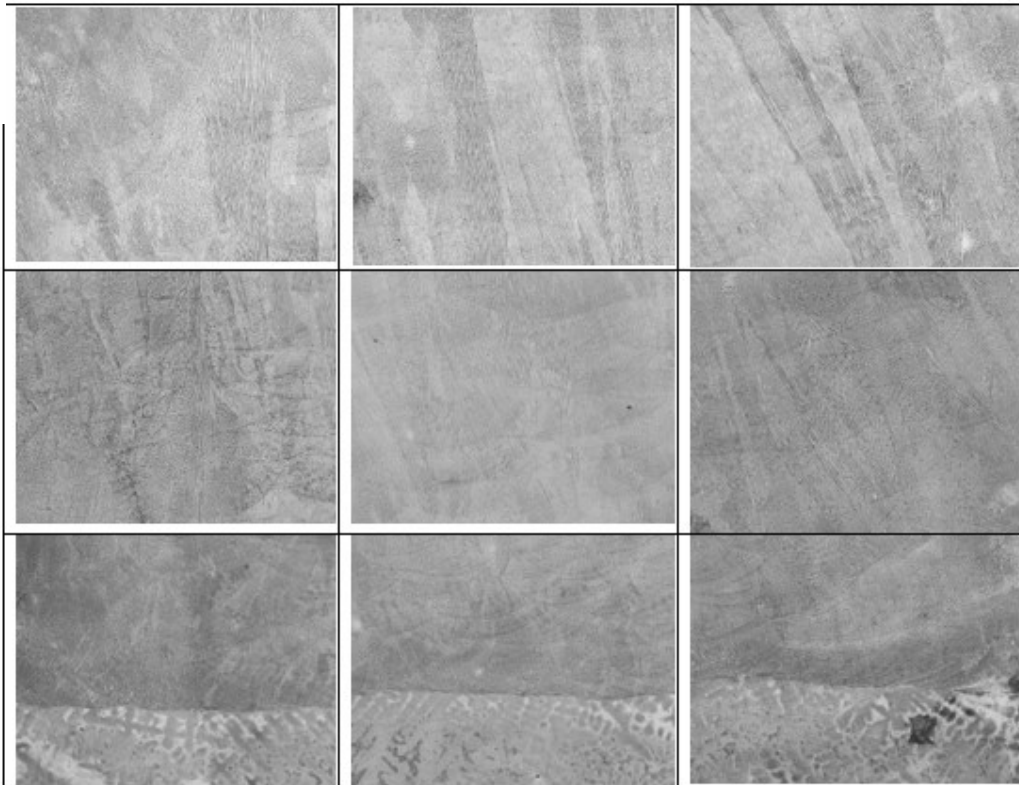


Figure 5.32: Etched Bulk 6 - Optical analysis performed at 50X

5.4.2.1 Top of the Cubes

Analysing the Cube 6 in its middle top, it is possible to notice a remarkable microstructural transition from the core to the top. As can be seen in Figure 5.33, a large columnar grain growth towards the top side is evident, and this grain growth stopped just some hundreds of microns before the part's surface where the microstructure turns equiaxed. The explanation of this microstructural transition finds its roots in the thermodynamic of solidification which, as reported in section 3.1.1, is governed by two main factors: the ratio “G/R” and cooling rate “GxR” where R is the solidification rate and G the temperature gradient. These two parameters respectively define the shape and size of the microstructural feature within the solidifying part according to the G and R local values. More in detail, when the ratio G/R increases, the solidifying dendrites tend to be more and more directional so promoting an epitaxial grain growth. On the contrary, as a consequence of a thermal gradient diminishing, the microstructure equiaxially solidifies. Therefore, since in the part the temperature diminishes from the bottom (where during the deposition much more heat is stored) to the top, the respective local thermal gradient values decrease together with the G/R ratio upwards. As a result, when the G value decreases under a specific threshold band, the microstructure starts changing its solidification morphology creating a transition zone where columnar and equiaxed cells are partially distinguishable at first, and then the microstructure becomes a homogeneous band of equiaxed grains (Figure 5.34). Finally, because of the very high cooling rate peculiar of the DED processes, ranging between 200-6000 K/s, the overall microstructure results to be very fine.

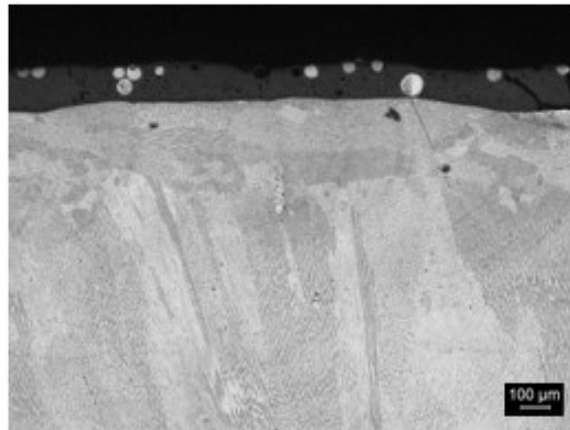


Figure 5.33: Micrograph of the etched Cube 6 top acquired at 50X (optical microscope)

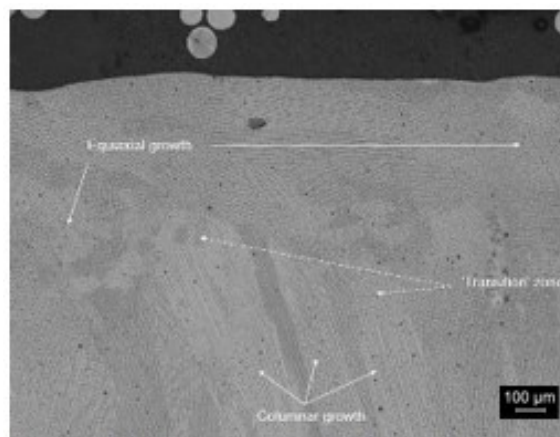


Figure 5.34: Micrograph of the etched Cube 6 top acquired at 100X (optical microscope) - transition from columnar to equiaxed microstructure.

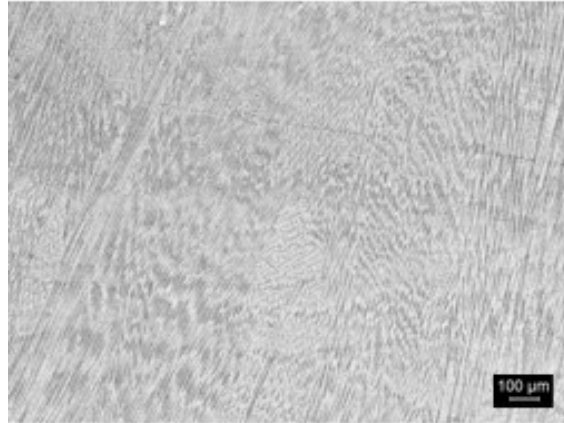


Figure 5.35: Cube's 4 micrograph acquired at 100X (Optical microscope) - Columnar grains just under the Top zone



Figure 5.36: Cube's 6 micrograph acquired at 100X (Optical microscope) - Columnar grains just under the Top zone

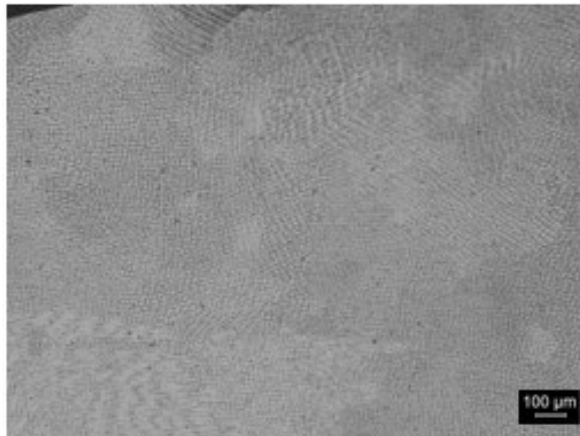


Figure 5.37: Cube's 5 micrograph acquired at 100X (Optical microscope) - Equiaxial grains at the right corner edge just under the Top zone.

5.4.2.2 Core of the Cubes

As can be seen from the following images, the cores' microstructural analysis revealed a prominent columnar microstructural morphology instead of equiaxial one. In fact, due to the high heat stored from the part in these zones and because of the high thermal gradient value, it is possible to state that the local G/R ratio was remarkably high during the solidification. Moreover, the dendrites solidification directionality it has been not lost during the same's growing through the successive layers.

However, what it seems fundamental to be reported, is the remarkably high microstructural anisotropy spread out all over the Cubes' cross-section.

First, among all, the adoption of a "Raster" scanning strategy (0/90/45/135/60/120°) led to sudden local variations of the microstructure's directionality within the part. As a matter of fact, following the EBSD assumptions made by Lakshmi L. Parimi et al. (3.3), a visible and repeated "staircase" effect as a result of the scanning direction variations, was detected in the Cube's 5 core (Figure 5.39). However, it is necessary to specify that it was possible to detect this phenomenon in specific areas only. In fact, because of the numerous scanning variations peculiar of the Raster strategy, the here reported micrographic results are different from that obtained by the authors mentioned above.

More in detail, Lakshmi L. Parimi et al. addressed this issue referring to a unidirectional and a bi-directional scanning strategy, then demonstrating the successive dendritic cells changing in orientation detectable in the sectioning plane parallel to the deposition direction.

Otherwise, in the case in point, it is not possible to locate a plane where the "staircase" effect is homogeneously present throughout a different cross-section, due to its 3D-1 distribution manner.

In addition, the composition of the epitaxial growth phenomena because of the heat stored within the part, the grain coarsening as a consequence of the induced thermal cycling, the grains' trend to grow according to the maximum heat's flux direction and the formation of interdendritic phases altering the lattice locally, led to an unpredictable morphology.

The reader is reminded of the sections of 3.1, 3.1.2 and 3.1.3 for further descriptions about the phenomena just mentioned.

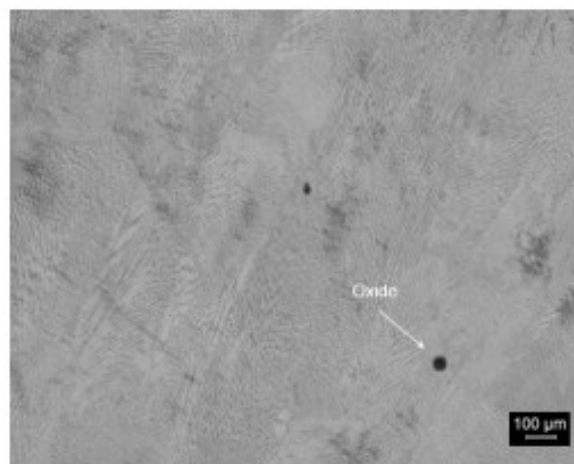


Figure 5.38: Micrograph acquired at 50X of Cube 5 (optical microscope) – Oxide

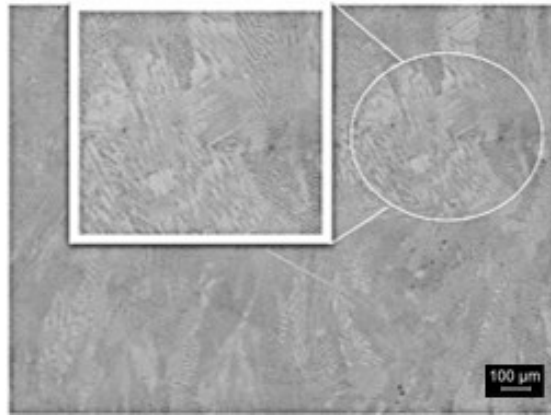


Figure 5.39: Micrograph acquired at 50X of Cube 5 (optical microscope) – Staircase effect



Figure 5.40: Micrograph acquired at 50X of Cube 6 (optical microscope) – Layering



Figure 5.41: Columnar inter-Melt Pool grain growth in Cube 6 – Micrograph acquired at 100x

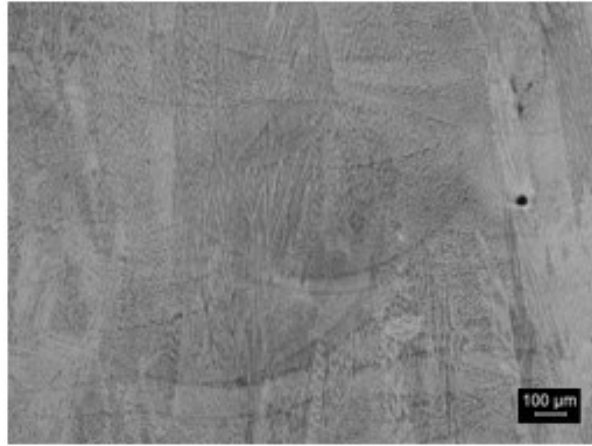


Figure 5.42: Columnar inter-Melt Pool grain growth in Cube 6 – Micrograph acquired at 100x

5.4.2.3 Bottom of the Cubes

Taking into account that one of the purposes of this thesis is to evaluate the capability of the DED process to be used as a method to repair the high-value metallic parts and thus, for this reason in this section, the interface of “as-deposited” material and the substrate are analysed. Interestingly, it is found that no liquid cracking phenomena or lack of fusion, were detected, whereas sometimes a noticeable (even though very thin) melt pools’ penetrations of the substrate can be easily recognised as shown in Figure 5.48. Also, considering the excellent melt pools’ coherence with the substrate and between themselves, and a substantial lack of porosity at the boundary zone, it can be said that from a morphological perspective a functional coherence between the substrate and deposited material was achieved. The grains size detected in the regions near the interface of deposited part/substrate is very fine because of the chilling effect exerted by the base plate which contributes to institute a very high local temperature gradient hence resulting in a high “GxR” cooling rate during solidification. Wanting to deal with the morphology of the grains, an overall epitaxial and columnar growth were found in the first layer as a result of the high “G/R” values. However, from few microns over the substrate, the microstructure starts changing in its morphology because of the G/R value local decrease which leads to an equiaxed grains growth sharing a transition zone with the columnar one. Therefore, in order to better understanding these topological changes of microstructural features within the part independence of their location, what it seems to be priory fundamental is to consider the growth of the grains as a consequence of the scanning strategy in conjunction with the dynamic melt pools’ characteristics.

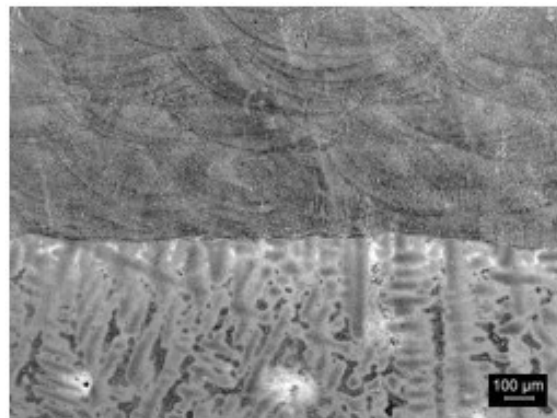


Figure 5.43: Substrate and deposition boundary zone in Cube 4 – Micrograph acquired at 50x.

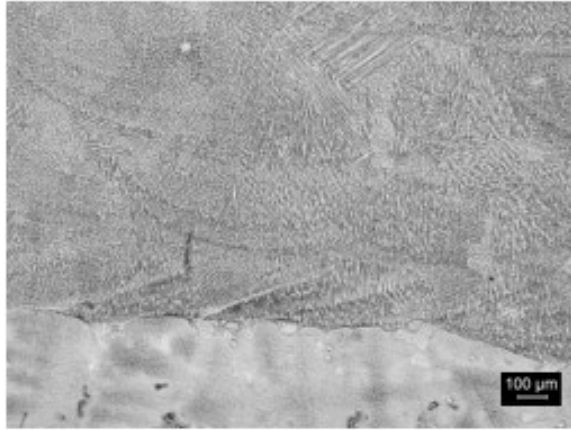


Figure 5.44: Substrate and deposition boundary zone and “staircase” effect in Cube 4 – Micrograph acquired at 100x.

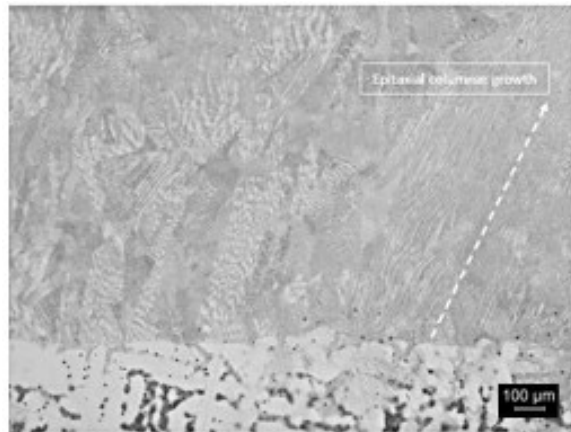


Figure 5.45: Substrate - deposition boundary zone and epitaxial columnar growth in Cube 5 – Micrograph acquired at 50x.

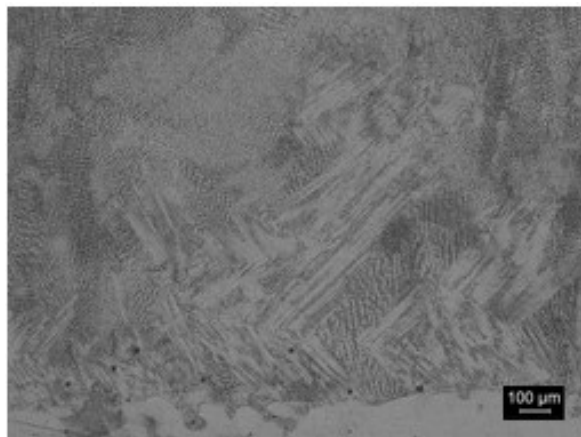


Figure 5.46: Substrate - deposition boundary zone in Cube 5 – Micrograph acquired at 100x.

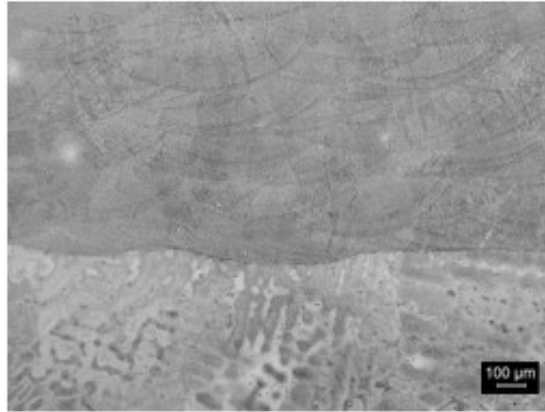


Figure 5.47: Substrate - deposition boundary zone in Cube 6 – Micrograph acquired at 50x.

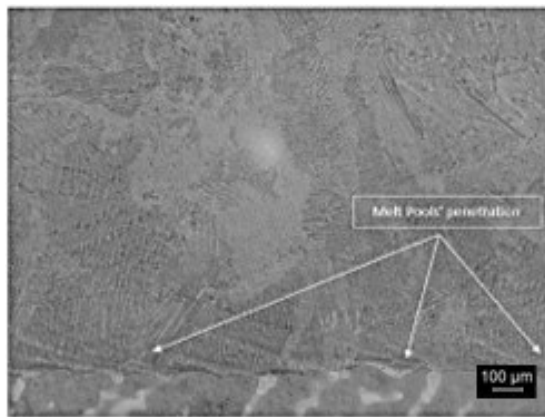


Figure 5.48: Substrate - deposition boundary zone in Cube 6 and Melt Pools' base plate penetration – Micrograph acquired at 100x.

5.5 SEM/EDS Cubes' analysis

As a consequence of the morphologic analysis, a more in-depth inspection of Cube 5 was performed aiming to analyse the deposition in its microstructural phases and inclusions presence.

At this purpose, new maps reporting images acquired at magnifications of 1000x, 2000x and 3000x respectively, have been reported in Figures 5.50, 5.51, 5.52 with the intent to report the overall framework of the microstructural features. In fact, because of the limitations in the magnification, the optical images were not suitable to be employed for analysing the microstructure in detail. Furthermore, the EDS analysis allowed to finally validate the nature of the detected phases and inclusions, and also be recognised by their chemical composition. More, in particular, these latter will be separately discussed in the following paragraphs also in conjunction with showing how the EDS tool has been exploited. Finally, an SEM analysis of the substrates has been performed.

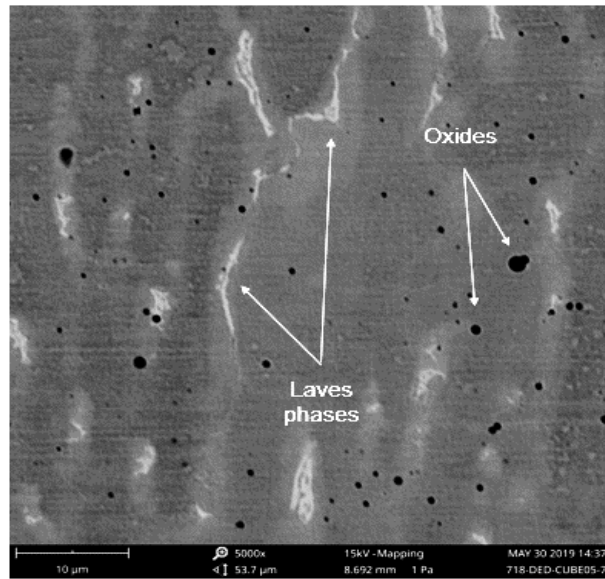


Figure 5.49: Cube's 5 SEM analysis at 5000x – Laves-phases and oxides

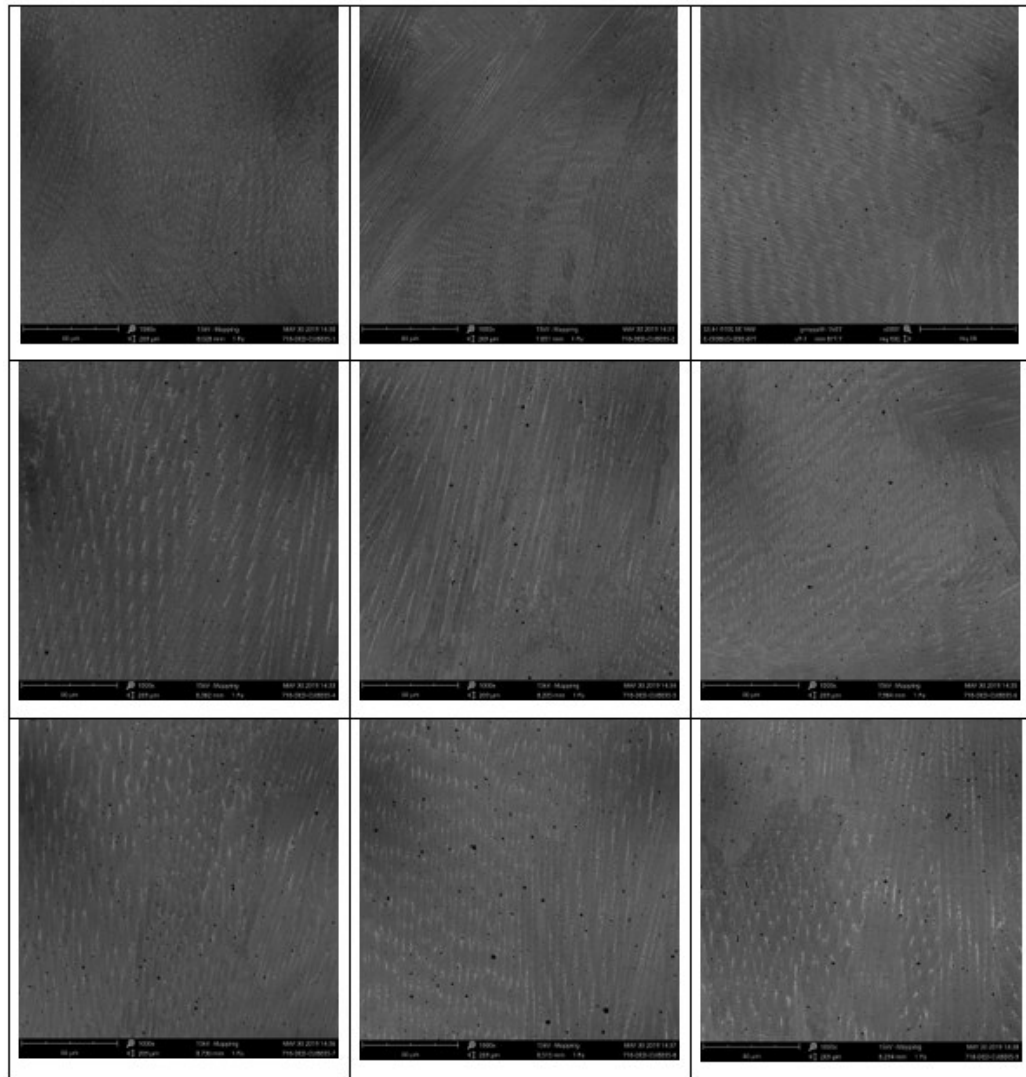


Figure 5.50: SEM mapping of Cube 5 at 1000x.

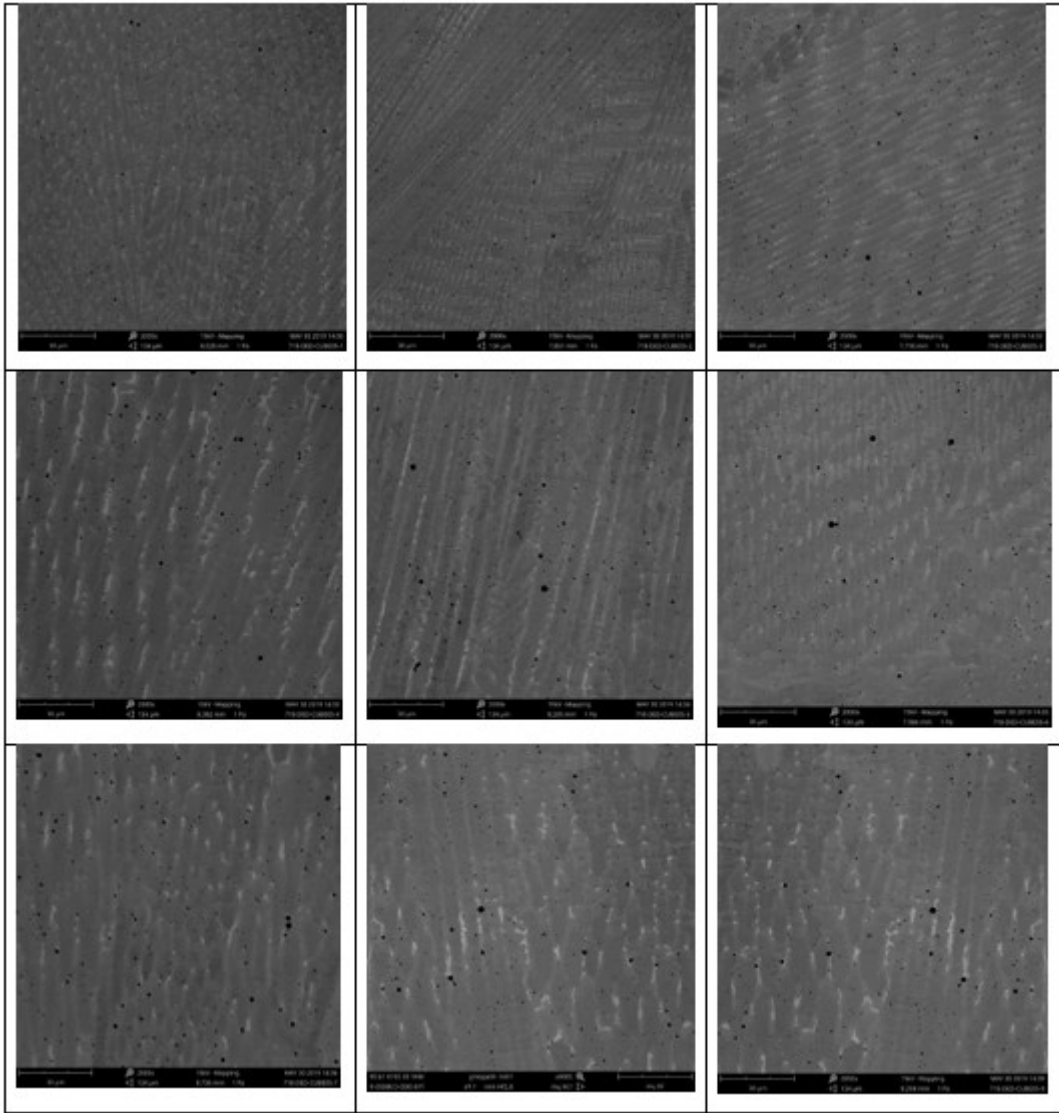


Figure 5.51: SEM mapping of Cube 5 at 2000x.

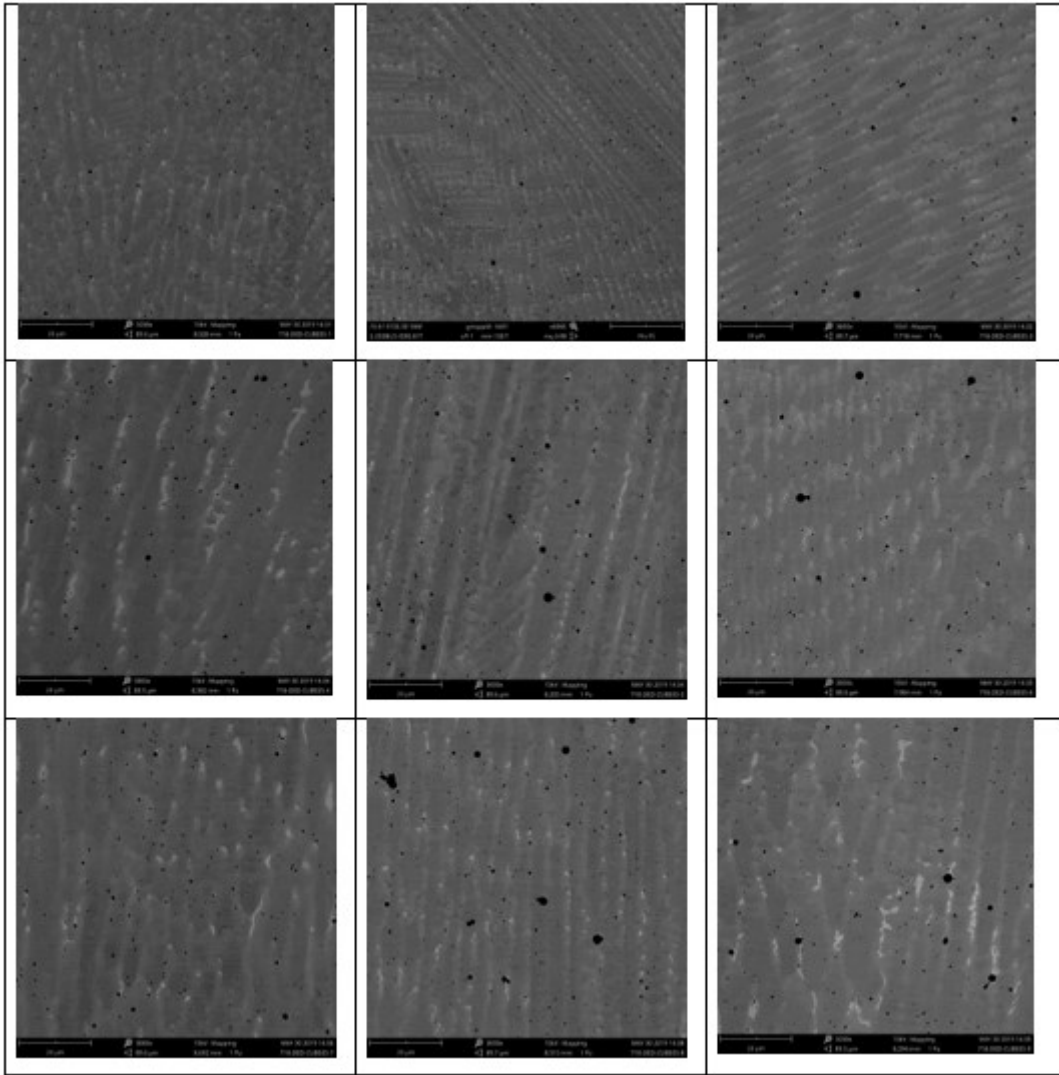


Figure 5.52: SEM mapping of Cube 5 at 3000x.

5.5.1 Laves phases – EDS analysis

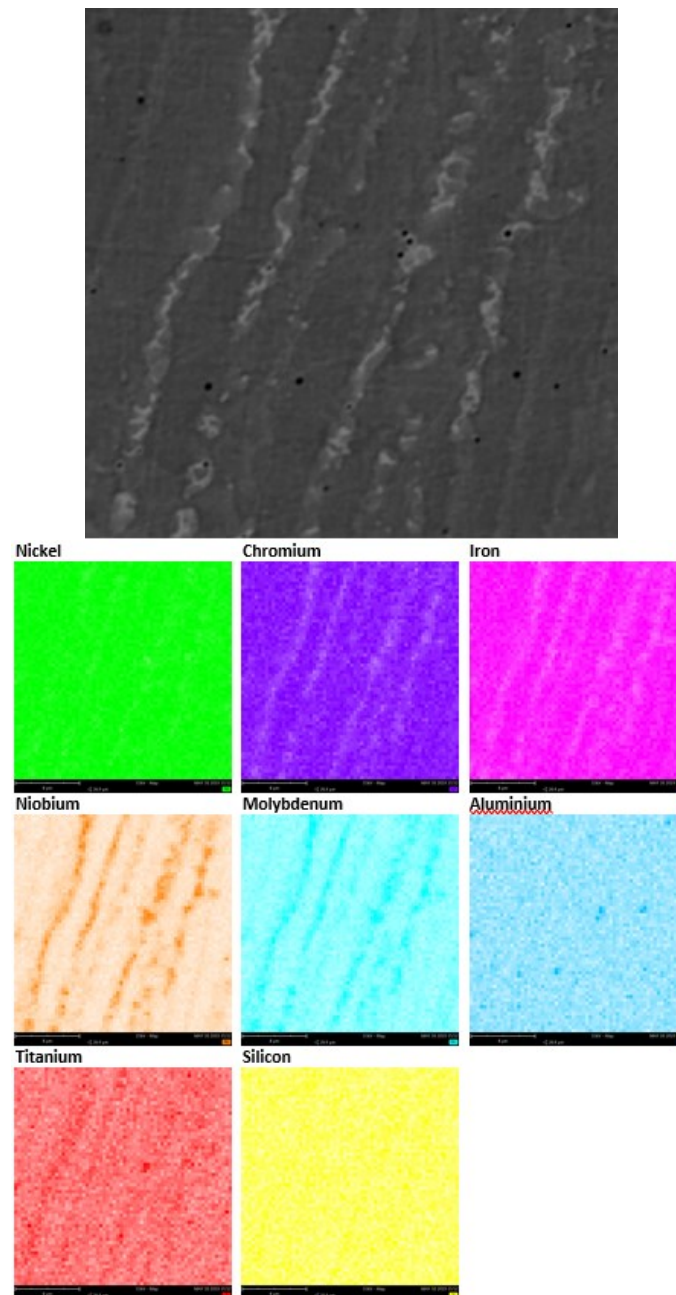


Figure 5.53: Laves phases EDS mapping and their chemical elements

A careful analysis of the phases mapped in their chemical composition, as reported in Figure 5.53, has been run positioning the analysis pointer in the region of interest..

Thanks to the X-Ray characteristic peaks emitted by the sample when stimulated by the electron source, it has been so possible to analyze the chemical elements present in the datum region quantitatively. As a result, the data displayed in Figure 5.49 provide an “Nb” content of 19,86% in weight, representing the typical major of 17% Nb concentration which is peculiar of Laves phases. Nevertheless, the Nb matrix depletion has been detected in the Laves phases neighbouring areas, at confirmation of the Nb segregation in the inter-dendritic areas at the matrix expenses..

5.5.2 δ -phases – EDS analysis

Since the δ -phases are usually generated in the Laves neighbouring areas, and because of their needle shape, the Laves phases have been inspected along their edges with the intent to reveal the presence of acicular phases. Even though the DED process generally does not allow to such phases being generated because of the low temperature involved within the part and the high cooling rates, it has been anyway possible to recognise the same (Paragraph 3.3.1).

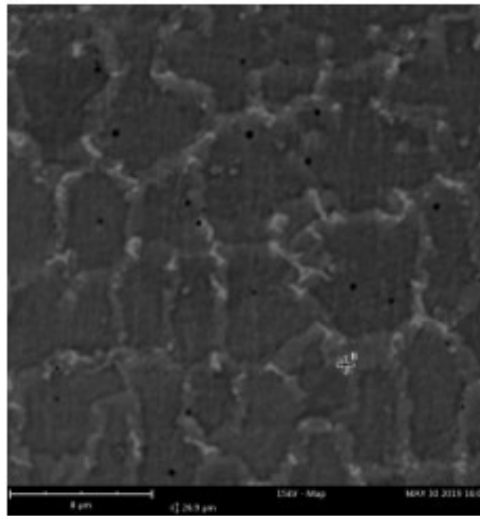
At this purpose, the EDS inspection has been run according to a straight scan line with the intent to highlight the difference in chemical composition between the matrix and the target phase, so creating a linear chemical profile Figure 5.56.

As a result of the chemical profiles trends, an Nb peak at 12,49% in weight, therefore, included in the δ -phase Nb composition range, has been recorded.

5.5.3 Carbides – EDS analysis

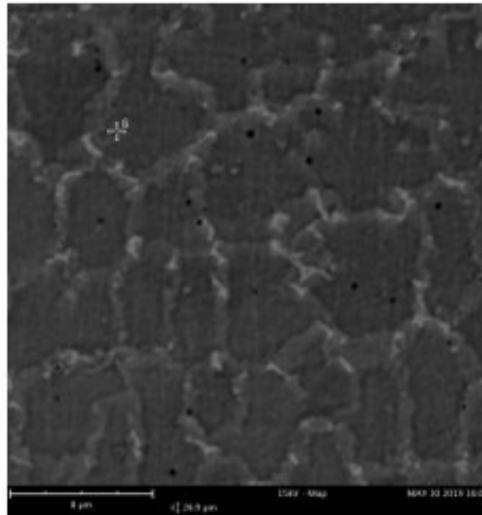
Besides the Laves and the δ -phases generation, the Nb segregation can also promote carbides formation. In Figure 5.57, is reported an Nb based carbide analysed in its chemical composition by EDS which revealed to be Nb and Ti-rich.

As aforementioned in the section 5.2.6, it is not possible to precisely state what exact species of carbides the feature analysed belong with. However, referring to paragraph 2.8.4 and Table 4, it can be said that the feature analysed could be representative of three main species NbC, Nb₆C or TiC.



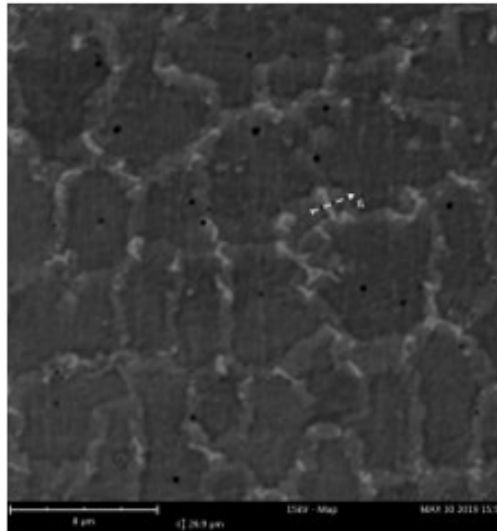
Element Number	Element Symbol	Element Name	Atomic Conc.	Weight Conc.
28	Ni	Nickel	47.40	44.80
24	Cr	Chromium	16.93	14.17
26	Fe	Iron	15.00	13.49
41	Nb	Niobium	13.28	19.86
42	Mo	Molybdenum	3.51	5.42
22	Ti	Titanium	1.64	1.27
14	Si	Silicon	1.19	0.54
13	Al	Aluminium	1.05	0.45

Figure 5.54: Laves phases detection in Cube 5 by the EDS analysis and their chemical composition.



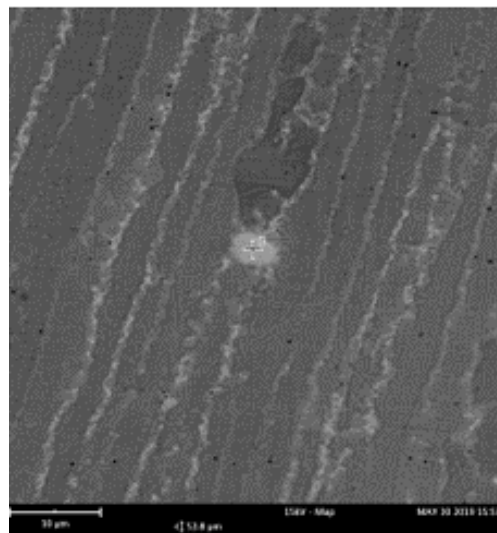
Element Number	Element Symbol	Element Name	Atomic Conc.	Weight Conc.
28	Ni	Nickel	31.28	43.31
8	O	Oxygen	27.24	10.28
13	Al	Aluminium	13.36	8.50
24	Cr	Chromium	12.44	15.26
26	Fe	Iron	11.90	15.68
41	Nb	Niobium	1.36	2.98
42	Mo	Molybdenum	1.30	2.95
22	Ti	Titanium	0.62	0.70
14	Si	Silicon	0.50	0.33

Figure 5.55: EDS matrix “Nb” depletion in the dendritic core areas.



Element Number	Element Symbol	Element Name	Atomic Conc.	Weight Conc.
28	Ni	Nickel	51.93	50.25
24	Cr	Chromium	17.85	15.30
26	Fe	Iron	15.75	14.50
41	Nb	Niobium	8.16	12.49
42	Mo	Molybdenum	2.93	4.63
22	Ti	Titanium	1.63	1.28
14	Si	Silicon	1.06	0.49
40	Zr	Zirconium	0.69	1.04

Figure 5.56: EDS scan line and δ -phases chemical composition.



Element Number	Element Symbol	Element Name	Atomic Conc.	Weight Conc.
41	Nb	Niobium	80.98	88.69
22	Ti	Titanium	12.58	7.10
14	Si	Silicon	1.58	0.52
42	Mo	Molybdenum	1.55	1.75
24	Cr	Chromium	1.50	0.92
26	Fe	Iron	1.29	0.85
13	Al	Aluminium	0.51	0.16
28	Ni	Nickel	0.00	0.00

Figure 5.57: SEM/EDS analysis of a Nb based carbide.

5.5.4 Oxide layer – EDS analysis

As reported in the representative Figure 5.58, the Cubes analysed to present an oxide layer not homogeneous in its thickness along with the feature's profile. At this purpose, the average thickness and the standard deviation of the layered oxide, have been calculated respectively to the Cube's top and the side walls. More in detail, the oxide layer's average thickness measured at the top of the built amounted to 72 μm with a standard deviation "SD" of 11,97%. Besides, the oxide layer's inhomogeneity is also constituted by its irregular morphology because of the embedding of non-melted particles within it. Furthermore, analysing the oxide layer's thickness at the side walls of the Cube 5, a relevant oxide layer thickness difference respect to that detected at the top, has been detected. The average thickness measured at the side walls is of 19 μm with a standard deviation of 2,5%, hence differing of around 50 μm from that was revealed in the Cube's top.

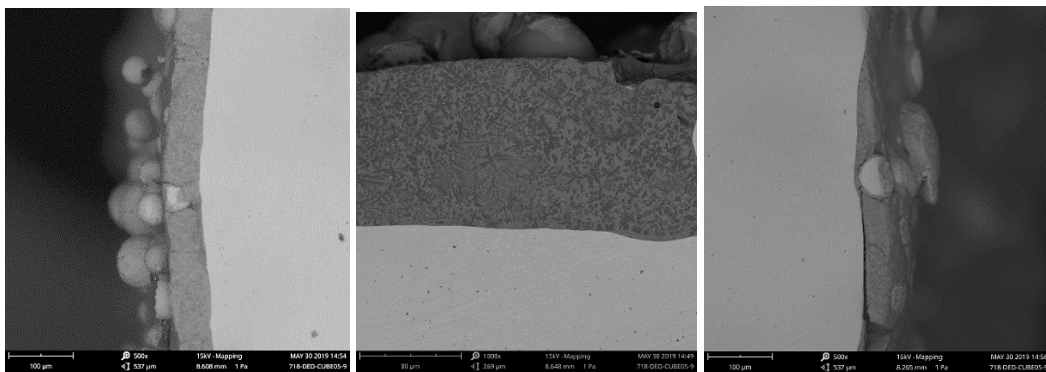


Figure 5.58: Oxide layer SEM images - Cube 5

Nevertheless, the oxide layer inhomogeneity is also findable in its chemical composition. In fact, as a consequence of the EDS analysis, two different types of oxides have been detected. More precisely, in the following SEM images have been highlighted the spots in which the layer has been analysed, and the chemical composition of the Al and Ti/Cr rich oxides detected.

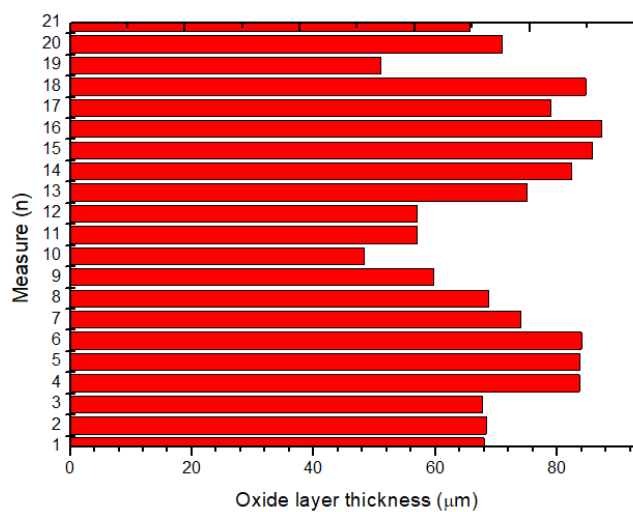


Figure 5.59: Oxide layer average thickness at the Top of Cube 5

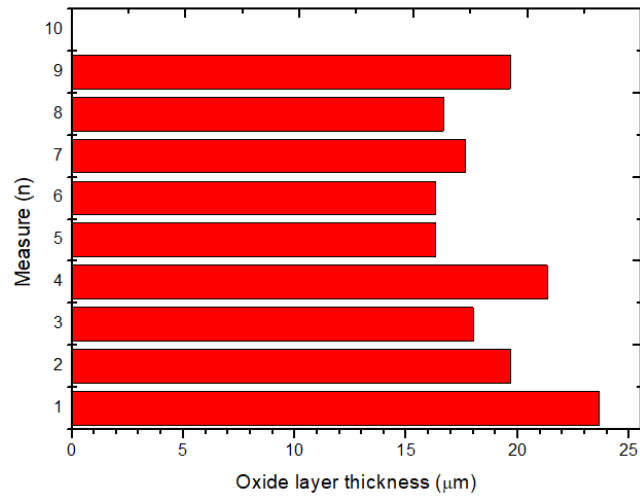
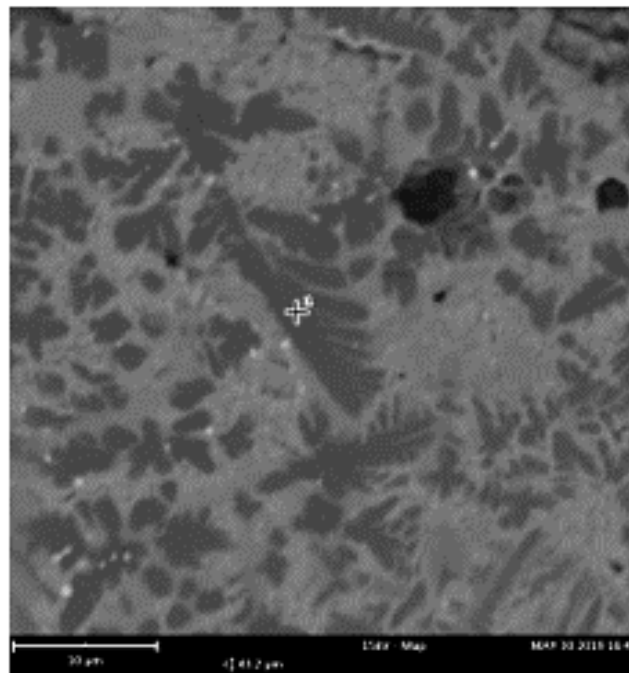


Figure 5.60: Oxide layer average thickness at the side walls of Cube 5



Element Number	Element Symbol	Element Name	Atomic Conc.	Weight Conc.
8	O	Oxygen	62.65	48.64
13	Al	Aluminium	34.93	45.73
22	Ti	Titanium	2.42	5.63

Figure 5.61: SEM/EDS analysis of the oxide layer- Aluminum oxide

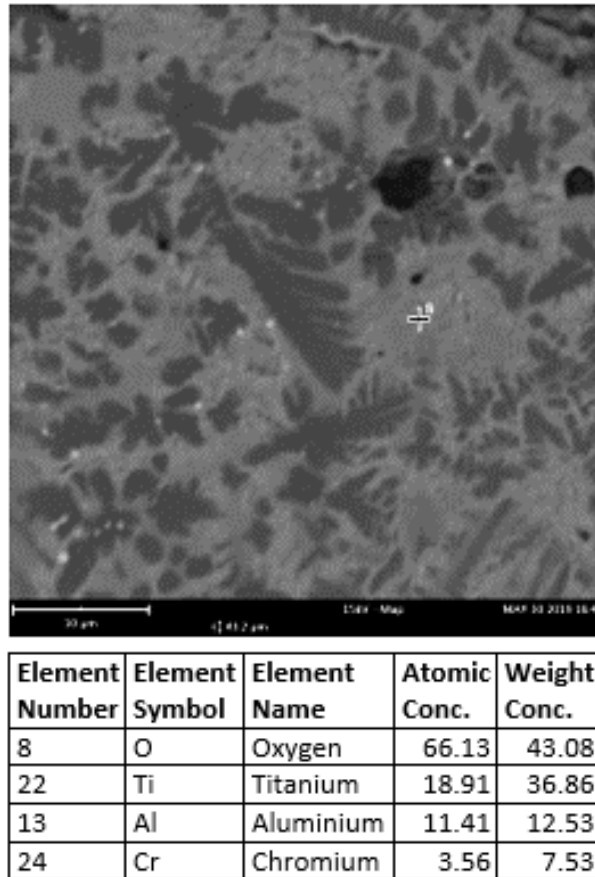


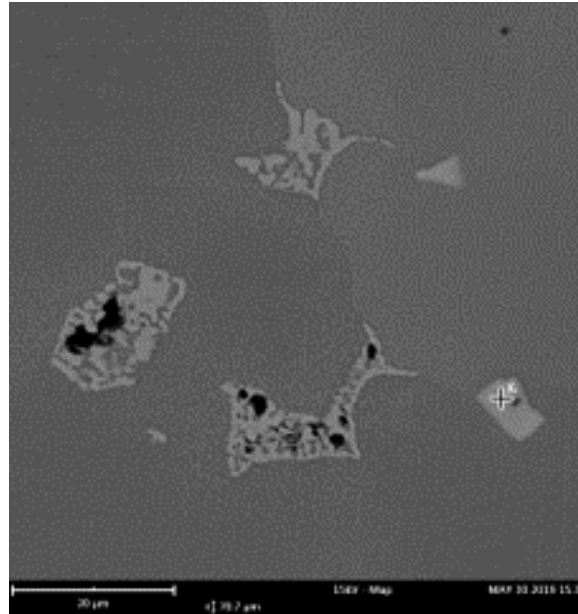
Figure 5.62: SEM/EDS analysis of the oxide layer- Titanium oxide.

5.6 SEM/EDS Substrate

In order to appreciate the microstructural differences between an additively built part a casted one instead, the Substrate has been analysed by SEM and EDS as well. The first findable difference between the substrate's matrix with the part's one is the absence of dendritic structures in the core. The low cooling rate (compared to that of AM) present in the casted part solidification, leads to a more homogeneous and isotropic microstructure's morphology of γ matrix. Nevertheless, the phases detected and previously detailed in the SEM/EDS part's analysis (such as Laves-phases, carbides and δ -phases), have been found in the substrates as well. However, because of the different manufacturing process characteristics, some of them result to be different respect to that achieved in the DED built apart from a morphologic perspective.

5.6.1 Carbides

As reported in Figure 5.63, the carbides' composition result to be approximately the same than that detected in the DED manufactured part with a prominent presence of Nb and Ti. Also, in this instance, it is not possible to locally define the carbides stichometry even though it is possible to venture the hypothesis of the species present according to the findable in literature. For further specification, the reader is reminded of paragraph 5.5.4.

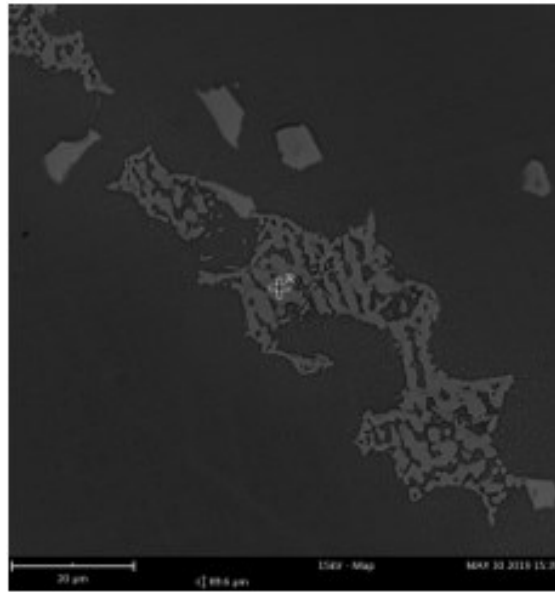


Element Number	Element Symbol	Element Name	Atomic Conc.	Weight Conc.
41	Nb	Niobium	80.53	88.36
22	Ti	Titanium	13.31	7.52
42	Mo	Molybdenum	1.59	1.80
14	Si	Silicon	1.51	0.50
24	Cr	Chromium	1.36	0.83
26	Fe	Iron	1.30	0.86
13	Al	Aluminium	0.40	0.13
28	Ni	Nickel	0.00	0.00

Figure 5.63: SEM/EDS analysis of a Nb based carbide.

5.6.2 Laves-phases

Otherwise from the Laves-phases detected within the part, the same generated in the substrate appear remarkably different in their morphology. The substrate's Laves does not exhibit a preferential directionality unlikely from the Cube's ones, which are directly influenced in their morphology by the deposition direction and by the G/R ratio. Furthermore, the Laves presence within the substrate is remarkably lower than that detected within the part in terms of percentage area, so marking a relevant discontinuity in microstructural features hence mechanical properties between the substrate and the deposited part.



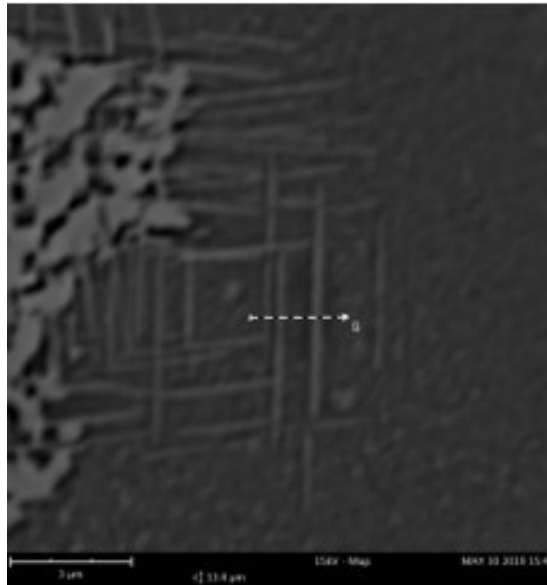
Element Number	Element Symbol	Element Name	Atomic Conc.	Weight Conc.
28	Ni	Nickel	38.96	34.60
41	Nb	Niobium	22.34	31.40
24	Cr	Chromium	15.71	12.36
26	Fe	Iron	13.72	11.59
42	Mo	Molybdenum	5.59	8.12
14	Si	Silicon	1.80	0.76
22	Ti	Titanium	1.27	0.92
13	Al	Aluminium	0.62	0.25

Figure 5.64: EDS analysis of Laves phases.

5.6.3 δ -phases

Another remarkable difference between the part and the Substrate's microstructure is the δ -phases morphology. In fact, because of the lower cooling rate that characterises the casted parts respect to that peculiar of the A.M., during the Substrate's solidification the δ -phases result to be coarser. Furthermore, the same is often detectable in the Laves neighbouring areas, in the form of needle-shaped phases intersected. With the intent to more reliably qualify the species of the needles shaped phases reported in Figure 5.59, an EDS scan line analysis has been run wanting to analyse the variation of the chemical elements along a straight line.

As a consequence of the line scan analysis, the elements percentage profiles have been acquired and analysed (Figure 5.65) in conjunction with their chemical composition. Therefore, from Figure 5.65 it can be concluded that the two Nb peaks with an average value major than 5-8% (12,1%) in weight concentration, are representative of the δ -phases crossing during the beamline scanning.



Element Number	Element Symbol	Element Name	Atomic Conc.	Weight Conc.
28	Ni	Nickel	53.87	52.98
24	Cr	Chromium	16.35	14.24
26	Fe	Iron	14.51	13.58
41	Nb	Niobium	7.77	12.10
42	Mo	Molybdenum	2.67	4.29
14	Si	Silicon	1.89	0.89
22	Ti	Titanium	1.70	1.37
13	Al	Aluminium	1.23	0.56

Figure 5.65: EDS scan line analysis of δ -phases detected within the Substrate.

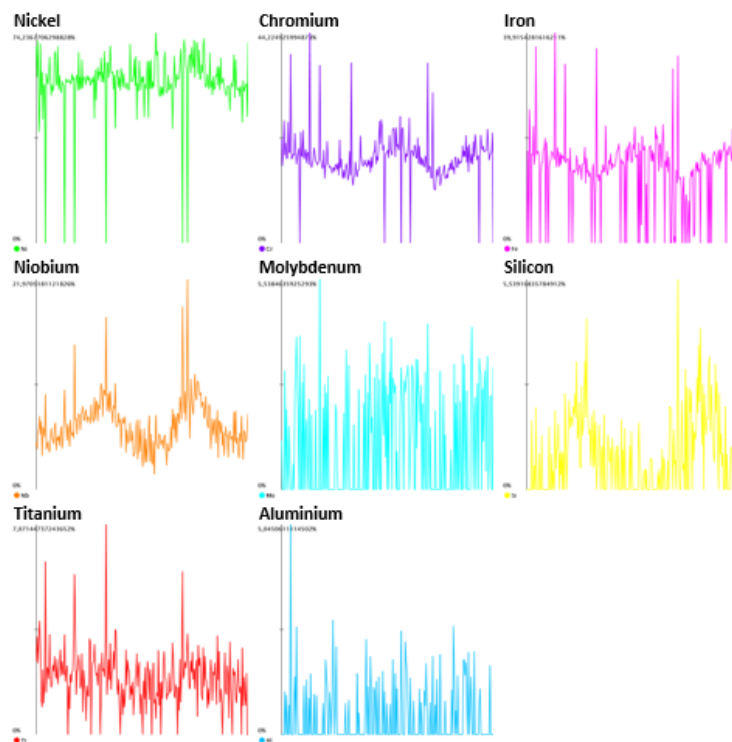


Figure 5.66: EDS line-scan analysis – chemical elements percentage profile along a straight line crossing two δ -phases embedded in the substrate.

6. Conclusions

In this thesis assignment, it has been presented a characterisation campaign of three different features (SSTs, Layers, and Cubes), realised in the Ni-based superalloy IN718 by Directed Energy Deposition (powder fed) with the intent to identify the optimal process parameters with which execute manufacturing and repairing operations of damaged aeronautic components. More in detail, 40 Single Scan Tracks deposited at different Laser Power and Feed rate values have been analysed in their morphologic appearance and microstructural features, so identifying a first deposition compliancy window. Successively, the characterisation has been extended to the two more massive features Layers and Cubes, analysing them in their morphological and microstructural traits as well as in their presence of defectology. According to the findings of this work, the following conclusions can be drawn;

- *6.1 SSTs*
- The “On top” analysis of SSTs depicted:
 - that all the SSTs are regular in their profile and shape except no. 1, 2, 3, 17, 33, 34, and 35.
 - that at the SSTs 21 and 25 were present two process instability
 - the 700W laser power level causes a severe interaction with the substrate leading to a pronounced HAZ width.
- The etched cross-section of the SSTs showed:
 - the absence of “Key hole” phenomena
 - the remarkable melt pools’ asymmetry of the SSTs:
 - no. 26,27,28,29,30,31 and 32 (obtained at 400W)
 - no. 10,11,12,13 (obtained at 300W)
 - no. 22
- The analysis of the melt pools’ main features dimensions concerning the process parameters employed showed:
 - the diminishing of the Fusion depth, melt pool’s width and bead height for scan speed increasing at the parity of P.
 - the melt pool’s width and fusion depth increase whether the laser power P increases at the parity of F
 - the bead height, hence the layer thickness diminishes at a parity of P whether the scan speed increases.
 - a not compliant feed rate value utilized to supply the deposition head which entailed to “Fusion Depth/Width” and “Bead Height Width” ratios, far from the ideal value of “1” so entailing to melt pools generally not balanced in their geometry
- All the non-compliancy of the SSTs has been summarised in Table 6.1
- In response to the SSTs’ results analysis, the medium F values of 750,900 mm/min and the medium P levels of 400,600W have been considered as optimal.
- the best solution in terms of defects minimization is represented by the choice of medium-high scan speed to compensate the high specific energy supplied.
- the best solution in terms of melt pools’ features maximization is pursuable adopting low scan speed and increasing the feed rate (amount of powder fluxed in the unit of time).

- *6.2 SLs*

The optical analysis of the SLs' cross-sections, "as-polished", revealed:

- The presence of the two defectology types: "oxide" and "pore", not directly distinguishable in their relative quantity, therefore, considered
- The maximum defects percentage area of 0,06% at layers built with F 750 mm/min of Substrate 2
- The maximum defects average size of 41,7 μm at layers built with F 900 mm/min of Substrate 2
- Considering the modest number of defects, the same analysis was not run on Substrate 1

The optical analysis of the SLs' cross-sections, "etched", revealed:

- superior melt pools' characteristics for the layers deposited at 600W
- superior melt pools' side overlapping for the layers deposited at 600W
- remarkable inhomogeneity of the depositions built at 400W
- The laser power level of 600W represents the optimal P-value to be employed
- The hatching distance Hd of 0,3 mm and the scan speed F of 750 mm/min represent the best choice wanting to minimise the defectology and maximise the deposition homogeneity.

- *6.3 Cubes*

The optical analysis of the "etched" Cubes revealed:

Bottom

- a dendritic and columnar growth juts out from the bottom of the built to the core
- the interface between the part, and the substrate is homogeneous, coherent and with a modest HAZ

Core

- no typical metal AM defectology such as Lack of fusions, or Key Holes was found
- the dendritic and columnar growth is consistent through different layers and the overlapped SSTs, suggesting an epitaxial growth.
- The deposition strategy and the directionality of the typical DED deposition led to a remarkable microstructural anisotropy.

Top

- A transition zone was observed nearby the Cubes' surfaces, marking a line between the dendritic columnar growth deriving from the parts' core and a cellular equiaxed microstructure detected at the edges.

The SEM/EDS analysis reported:

- a remarkably high inter-dendritic Laves presence (not directly quantified because of the optical nature of the analysis method adopted), and
- Laves presence noticed in the top neighbouring areas despite the generally low local thermal gradient that characterises this zone
- presence of carbides Nb and Ti-rich dispersed in the γ matrix
- presence of Ti and Al oxides
- Laves phases
- Delta phases
- Ti and Al oxides dispersed in the oxide layer covering the Cubes' surfaces

To conclude, the optimal solution in terms of process parameters employed in the characterisation campaign considered has been identified in the adoption of P 600W, F 750 mm/min and HD 0,3 mm.

7. References

- Akram, J. *et al.* (2018) ‘Understanding grain evolution in additive manufacturing through modeling’, *Additive Manufacturing*. Elsevier, 21(September 2017), pp. 255–268. doi: 10.1016/j.addma.2018.03.021.
- Alderliesten, R. C. (2018) ‘Introduction to Aerospace Structures and Materials’, *TU Delft-EDX online course*.
- Arcam EBM (2019) *History - Arcam AB*. Available at: <http://www.arcam.com/company/about-arcam/history/> (Accessed: 7 February 2019).
- ASTM International (2019a) *ASTM International - Standards Worldwide*. Available at: <https://www.astm.org/> (Accessed: 7 February 2019).
- ASTM International (2019b) *ISO/ASTM 52900:2015(en), Additive manufacturing — General principles — Terminology*. Available at: <https://www.iso.org/obp/ui/#iso:std:iso-astm:52900:ed-1:v1:en> (Accessed: 2 January 2019).
- Attaran, M. (2017) ‘The rise of 3-D printing : The advantages of additive manufacturing over traditional manufacturing’, *Business Horizons*. ‘Kelley School of Business, Indiana University’, 60(5), pp. 677–688. doi: 10.1016/j.bushor.2017.05.011.
- Beaman, J. J. (2001) ‘Solid Freeform Fabrication : An Historical Perspective’, *SFF - Solid Freeform Fabrication Symposium (2009)*, pp. 584–595. doi: 10.1007/978-1-4615-6327-3.
- Bourell, D. L. D. *et al.* (2009) ‘A brief history of additive manufacturing and the 2009 roadmap for additive manufacturing: looking back and looking ahead’, *US-Turkey Workshop on Rapid Technologies (RapidTech2009)*, (2), pp. 5–11. doi: 10.1089/3dp.2013.0002.
- BRUKER (2019) *Combined EBSD and EDS Analysis on SEM - Webinars | Bruker*. Available at: <https://www.bruker.com/events/webinars/combined-ebds-and-eds-analysis-on-sem.html> (Accessed: 24 May 2019).
- Carlo Baese (1902) ‘Photographic process for the reproduction of plastic objects.’, *US774549A patent*. Available at: <https://patents.google.com/patent/US774549A/en> (Accessed: 5 February 2019).
- Cunningham, C. R. *et al.* (2018) ‘Invited review article: Strategies and processes for high quality wire arc additive manufacturing’, *Additive Manufacturing*. Elsevier, 22(June), pp. 672–686. doi: 10.1016/j.addma.2018.06.020.
- Debroy, T. *et al.* (2018) ‘Progress in Materials Science Additive manufacturing of metallic components – Process , structure and properties’, 92, pp. 112–224. doi: 10.1016/j.pmatsci.2017.10.001.
- Digital Engineering (2019) *Wohlers Report 2019: Record Growth in Additive Manufacturing Materials - Digital Engineering 24/7*. Available at: <https://www.digitalengineering247.com/article/wohlers-report-2019-record-growth-in-additive-manufacturing-materials/design> (Accessed: 30 April 2019).
- European Project ‘4D Hybrid’ (2019) *Objectives – 4D Hybrid*. Available at: <http://4dhybrid.eu/objectives/> (Accessed: 3 February 2019).
- Fayazfar, H. *et al.* (2018) ‘A critical review of powder-based additive manufacturing of ferrous alloys: Process parameters, microstructure and mechanical properties’, *Materials and Design*. Elsevier Ltd, 144, pp. 98–128. doi: 10.1016/j.matdes.2018.02.018.

- Galati, M. and Iuliano, L. (2018) ‘A literature review of powder-based electron beam melting focusing on numerical simulations’, *Additive Manufacturing*. Elsevier B.V., 19, pp. 1–20. doi: 10.1016/j.addma.2017.11.001.
- Gasman, L. (2019) *Additive aerospace considered as a business*. SmarTech M, *Additive Manufacturing for the Aerospace Industry*. SmarTech M. Virginia, United States: Elsevier Inc. doi: 10.1016/B978-0-12-814062-8.00017-0.
- Gibson, I., Rosen, D. and Stucker, B. (2013) ‘Standard Terminology for Additive Manufacturing Technologies’, *Rapid Manufacturing Association*, pp. 10–12. doi: 10.1520/F2792-12A.2.
- Gibson, I., Rosen, D. and Stucker, B. (2014) ‘Directed Energy Deposition Processes’, in *Additive Manufacturing Technologies*, pp. 245–268. doi: 10.1007/978-1-4939-2113-3_10.
- Goodfellow, A. J. (2018) ‘Strengthening mechanisms in polycrystalline nickel-based superalloys’, *Materials Science and Technology (United Kingdom)*. Taylor & Francis, 34(15), pp. 1793–1808. doi: 10.1080/02670836.2018.1461594.
- Greer, C. *et al.* (2019) ‘Introduction to the design rules for Metal Big Area Additive Manufacturing’, *Additive Manufacturing*. Elsevier B.V., 27, pp. 159–166. doi: 10.1016/j.addma.2019.02.016.
- I. Gibson, D.W. Rosen, B. S. (2010) ‘Rapid Prototyping to Direct Digital Manufacturing’, *Additive Manufacturing Technologies*.
- innovametric (2019) *PolyWorks Modeler | InnovMetric Software*. Available at: https://www.innovmetric.com/en/products/polyworks-modeler?gclid=Cj0KCQjw5J_mBRDVARIsAGqGLZBZcHD-8KVmUa2USe2kiRBpkQ5xUcIuFUk0pSptyffr6CtYnKNDWCwaAgzeEALw_wcB (Accessed: 30 April 2019).
- Kumara, C. *et al.* (2019) ‘Microstructure modelling of laser metal powder directed energy deposition of alloy 718’. Elsevier, 25(November 2018), pp. 357–364. doi: 10.1016/j.addma.2018.11.024.
- L. Xue, M. U. I. (2006) ‘Laser consolidation-a novel one-step manufacturing process for making net-shape functional components Processing’, *Cost Effective Manufacture via Net-Shape*, (Neuilly-sur-Seine, France.).
- Laserdyne 430 | Primapower* (no date). Available at: <https://www.primapower.com/us/laserdyne-430/#1448982719858-0eaae0f8-b51dfc72-a00fae4f-fbacb154-86055a6d-1b9e> (Accessed: 8 July 2019).
- Li, Y., Chen, K. and Tamura, N. (2018) ‘Mechanism of heat affected zone cracking in Ni-based superalloy DZ125L fabricated by laser 3D printing technique’, *Materials and Design*. Elsevier Ltd, 150, pp. 171–181. doi: 10.1016/j.matdes.2018.04.032.
- Liu, R. *et al.* (2016) *Aerospace applications of laser additive manufacturing, Laser Additive Manufacturing: Materials, Design, Technologies, and Applications*. Elsevier Ltd. doi: 10.1016/B978-0-08-100433-3.00013-0.
- Mahamood, R. M. and Akinlabi, E. T. (2018) ‘Effect of Powder Flow Rate on Surface Finish in Laser Additive Manufacturing Process’, *IOP Conference Series: Materials Science and Engineering*, 391(1). doi: 10.1088/1757-899X/391/1/012005.
- Mazumder, J. (2017) ‘Laser-aided direct metal deposition of metals and alloys’, in *Laser Additive Manufacturing*. Elsevier, pp. 21–53. doi: 10.1016/B978-0-08-100433-3.00001-4.

- McKinsey&Company (2018) *Ops 4.0: The Human Factor--Recognizing the capability challenge* | McKinsey & Company. Available at: <https://www.mckinsey.com/business-functions/operations/our-insights/operations-blog/ops-40-the-human-factor-recognizing-the-capability-challenge> (Accessed: 3 January 2019).
- Michael Ashby, Hugh Shercliff, D. C. (2009) *Materiali-Dalla scienza alla progettazione ingegneristica*.
- Minet, K. *et al.* (2019) 8. *Superalloys, powders, process monitoring in additive manufacturing, Additive Manufacturing for the Aerospace Industry*. Elsevier Inc. doi: 10.1016/B978-0-12-814062-8.00009-1.
- Molitch-Hou, M. (2018) ‘Overview of additive manufacturing process’, *Additive Manufacturing*. Butterworth-Heinemann, pp. 1–38. doi: 10.1016/B978-0-12-812155-9.00001-3.
- Najmon, J. C., Raeisi, S. and Tovar, A. (2019) *Review of additive manufacturing technologies and applications in the aerospace industry, Additive Manufacturing for the Aerospace Industry*. Elsevier Inc. doi: 10.1016/B978-0-12-814062-8.00002-9.
- Ngo, T. D. *et al.* (2018) ‘Additive manufacturing (3D printing): A review of materials, methods, applications and challenges’, *Composites Part B: Engineering*. Elsevier, 143(December 2017), pp. 172–196. doi: 10.1016/j.compositesb.2018.02.012.
- Parimi, L. L. *et al.* (2013) ‘Microstructural and texture development in direct laser fabricated IN718 ☆’, *Materials Characterization*. The Authors, 89, pp. 102–111. doi: 10.1016/j.matchar.2013.12.012.
- Pierre Alfred Leon Ciraud (1972) ‘A method and apparatus for manufacturing objects made of any arbitrary material meltable’, *DE2263777A1 Patent*. Available at: <https://patents.google.com/patent/DE2263777A1/en> (Accessed: 6 February 2019).
- Sames, W. J. *et al.* (2016) ‘The metallurgy and processing science of metal additive manufacturing’, *International Materials Reviews*. Taylor & Francis, 61(5), pp. 315–360. doi: 10.1080/09506608.2015.1116649.
- Shamsaei, N. *et al.* (2015) ‘An overview of Direct Laser Deposition for additive manufacturing; Part II: Mechanical behavior, process parameter optimization and control’, *Additive Manufacturing*. Elsevier B.V., 8, pp. 12–35. doi: 10.1016/j.addma.2015.07.002.
- Shim, D. S. *et al.* (2016) ‘Effect of layer thickness setting on deposition characteristics in direct energy deposition (DED) process’, *Optics and Laser Technology*. Elsevier, 86, pp. 69–78. doi: 10.1016/j.optlastec.2016.07.001.
- Sims, C. T. (1984) ‘A History of Superalloy Metallurgy for Superalloy Metallurgists’, *Superalloys 1984 (Fifth International Symposium)*, pp. 399–419. doi: 10.7449/1984/Superalloys_1984_399_419.
- Singh, R. and Singh, S. (2017) ‘Additive Manufacturing: An Overview’, *Reference Module in Materials Science and Materials Engineering*, pp. 1–12. doi: 10.1016/B978-0-12-803581-8.04165-5.
- Swainson, W. K. (1971) ‘Method, medium and apparatus for producing three-dimensional figure product’, *US4041476A*. Available at: <https://patents.google.com/patent/US4041476A/en> (Accessed: 5 February 2019).
- Tang, L. *et al.* (2008) ‘Variable Powder Flow Rate Control in Laser Metal Deposition Processes’, *Journal of Manufacturing Science and Engineering*, 130(4), p. 041016. doi:

10.1115/1.2953074.

Tapia, A. S. (2006) 'COMPUTATIONAL DESIGN OF NICKEL BASED SUPERALLOYS FOR INDUSTRIAL GAS TURBINE COMPONENTS', *A THESIS PRESENTED TO THE GRADUATE SCHOOL OF THE UNIVERSITY OF FLORIDA IN PARTIAL FULFILLMENT OF THE REQUIREMENTS FOR THE DEGREE OF MASTER OF SCIENCE UNIVERSITY OF FLORIDA*.

Thompson, S. M. *et al.* (2015) 'An overview of Direct Laser Deposition for additive manufacturing; Part I: Transport phenomena, modeling and diagnostics', *Additive Manufacturing*. Elsevier B.V., 8, pp. 36–62. doi: 10.1016/j.addma.2015.07.001.

Villeneuve, F. *et al.* (2018) 'Typology of geometrical defects in Electron Beam Melting', *Procedia CIRP*, 75, pp. 92–97. doi: 10.1016/j.procir.2018.04.033.

Wei, H. L. *et al.* (2019) 'Three-dimensional grain growth during multi-layer printing of a nickel-based alloy Inconel 718'. Elsevier, 25(October 2018), pp. 448–459. doi: 10.1016/j.addma.2018.11.028.

Wong, K. V and Hernandez, A. (2012) 'A Review of Additive Manufacturing', 2012. doi: 10.5402/2012/208760.

Wu, B. *et al.* (2018) 'A review of the wire arc additive manufacturing of metals: properties, defects and quality improvement', *Journal of Manufacturing Processes*. Elsevier, 35(August), pp. 127–139. doi: 10.1016/j.jmapro.2018.08.001.

Zenou, M. and Grainger, L. (2018) *3 - Additive manufacturing of metallic materials, Additive Manufacturing: Materials, Processes, Quantifications and Applications*. Elsevier Inc. doi: 10.1016/B978-0-12-812155-9/00003-7.

Zhang, Q. li, Yao, J. hua and Mazumder, J. (2011) 'Laser Direct Metal Deposition Technology and Microstructure and Composition Segregation of Inconel 718 Superalloy', *Journal of Iron and Steel Research International*. Central Iron and Steel Research Institute, 18(4), pp. 73–78. doi: 10.1016/S1006-706X(11)60054-X.

Zhang, W. *et al.* (2017) 'Additive manufacturing of metallic components – Process, structure and properties', *Progress in Materials Science*, 92, pp. 112–224. doi: 10.1016/j.pmatsci.2017.10.001.

Zhang, Y. *et al.* (2018) *2 - Additive manufacturing processes and equipment, Additive Manufacturing: Materials, Processes, Quantifications and Applications*. Elsevier Inc. doi: 10.1016/B978-0-12-812155-9/00002-5.

Zhong, C. *et al.* (2019) 'Study of nickel-based super-alloys Inconel 718 and Inconel 625 in high- deposition-rate laser metal deposition', *Optics and Laser Technology*. Elsevier Ltd, 109(January 2018), pp. 352–360. doi: 10.1016/j.optlastec.2018.08.003.

8.Thanks

Ringrazio la mia famiglia e miei vecchi amici che soprattutto nell'ultimo periodo di maggiore difficoltà non si sono risparmiati a tendermi una mano di aiuto e conforto sincero. Ringrazio la Prof.ssa Biamino e il suo team di dottorandi e ricercatori da cui nel corso dei mesi ho potuto imparare molto a livello professionale ed umano. Ringrazio in particolar modo il Dr. Saboori, uomo di intelligenza, comprensione, comunicazione ed empatia; mi arrecherei il diritto di definirlo uomo di insegnamento. Non so, io l'ho sempre chiamato "Mr. Professor"! Ringrazio infine tutto il corpo docenti del corso di Ingegneria dei Materiali del Politecnico di Torino in cui nel corso degli anni ho sempre riconosciuto professionalità e attenzione alla formazione, in aula e nei corridoi.